Dissertation
submitted to the
Combined Faculties for the Natural Sciences and for Mathematics
of the Ruperto-Carola University of Heidelberg, Germany
for the degree of
Doctor of Natural Sciences

Put forward by
Diplom-Physiker: Kamil Lipert
Born in: Lublin, Poland
Oral examination: 22.07.2011

Development of a micro-Hall magnetometer and studies of individual Fe - filled carbon nanotubes

Referees: **Prof. Dr. Rüdiger Klingeler**
Prof. Dr. Werner Keune

Aufbau eines Mikro-Hall-Magnetometers und Untersuchungen individueller Fe-gefüllter Kohlenstoffnanoröhren:

In dieser Arbeit werden experimentelle Untersuchungen individueller Fe-gefüllter Kohlenstoffnanoröhren (CNT) mittels Hall-Magnetometrie präsentiert. Hierfür wurden auf Basis von GaAs/AlGaAs-Heterostrukturen mikrostrukturierte Hall-Sonden hergestellt, welche die Untersuchung der Streufelder einzelner nanoskaliger Magnete ermöglichen. Die Hall-Sensoren wurden mit Elektronenstrahllithographie und chemischen Nassätzverfahren strukturiert und mittels Rasterelektronenmikroskopie, Rasterkraftmikroskopie und Transportmessungen charakterisiert. Mit einem Mikromanipulator wurden einzelne Fe-CNT auf die aktive Fläche (800×800 nm^2) der Sensoren platziert. Messungen an den Fe-CNT zeigen die Anwendbarkeit der Sensoren für die Untersuchung nanoskaliger Magnete. Die Untersuchung eines einzelnen Fe-Nanodrahtes mit Durchmesser d = 26 nm zeigt, dass die Ummagnetisierung in einen lokalisierten Prozess stattfindet, wobei die Winkelabhängigkeit der Nukleationsfelder sich sehr gut im Rahmen des Curling Modells beschreiben lässt. Abhängig vom gewählten Winkel treten Nukleationsfelder bis etwa 900 mT auf. Neben einzelnen Nanodrähten wurden auch die magnetischen Eigenschaften von Ensembles unterschiedlich funktionalisierter CNT mit alternierender Gradienten- und SQUID-Magnetometrie untersucht. Dabei wurde der Einfluss ferromagnetischer Katalysatorpartikel im Detail untersucht und es konnte gezeigt werden, dass durch eine nachträgliche Wärmebehandlung der CNT das Katalysatormaterial vollständig entfernt werden kann.

Development of a micro-Hall magnetometer and studies of individual Fe – filled carbon nanotubes:

This work presents Hall magnetometry studies on individual Fe-filled carbon nanotubes (CNT). For this approach high sensitivity micro Hall sensors based on a GaAs/AlGaAs heterostructure with two dimensional electron gas (2DEG) were developed. Electron beam lithography and wet chemical etching were utilized for patterning Hall sensors onto the heterostructure surface. The devices were characterized by means of scanning electron microscopy, atomic force microscopy and transport measurements. Individual Fe-filled CNTs were placed on active part of devices (800×800 nm^2) with aid of micromanipulator system. Measurements on an individual iron nanowires confirmed devices applicability for measurements of nanoscale magnets. High nucleation fields were found of about 900 mT for a Fe nanowire with diameter of d = 26 nm. The magnetization reversal mechanism was found to be a localized process whereas the angular dependence of nucleation fields is in a good agreement with a curling mode. Through magnetization studies performed on differently functionalized ensembles of CNT by means of Alternating Gradient – and Superconducting Quantum Interference Device (SQUID) magnetometry a strong influence of a remaining ferromagnetic catalyst material on the magnetic properties of CNT was observed. Magnetization studies proved that a post annealing method removes catalyst material completely.

Contents

Abbreviations used in this thesis

AA	active area
2DEG	two dimensional electron gas
AGM	alternating gradient magnetometer
AC	alternating current
AFM	atomic force microscope
BCC	body center cubic
CNT	carbon nanotubes
CVD	chemical vapor deposition
DC	direct current
DWCNT	double-wall carbon nanotube
EA	easy axis
EBL	electron beam lithography
EDX	energy-dispersive X-ray
FCC	face centered cubic
FIB	focused ion beam
FM	Ferromagnet
HEMT	high electron mobility transistor
HCP	hexagonal closed packed
IPA	isopropanol,
MBE	molecular beam epitaxy
MFM	magnetic force microscope
MIBK	methyl-isobutyl-keton
MWCNT	multi-wall carbon nanotube
NMP	N-methylpyrrolidon
NMR	nuclear magnetic resonance
PMMA	poly(methyl methacrylate)
RT	room temperature
SQUID	superconducting quantum interference device
SSCVD	single source chemical vapor deposition
SWCNT	single-wall carbon nanotube
TCE	Trichloroethylene
UHV	ultra high vacuum

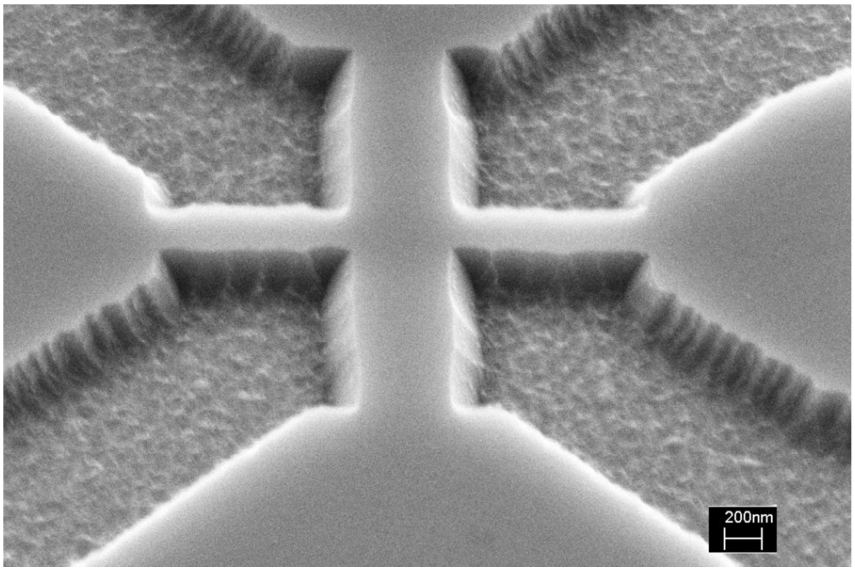

(GaAs/AlGaAs micro-Hall device) Kamil Lipert and Josef Biberger,
University of Regensburg, 14.03.2008

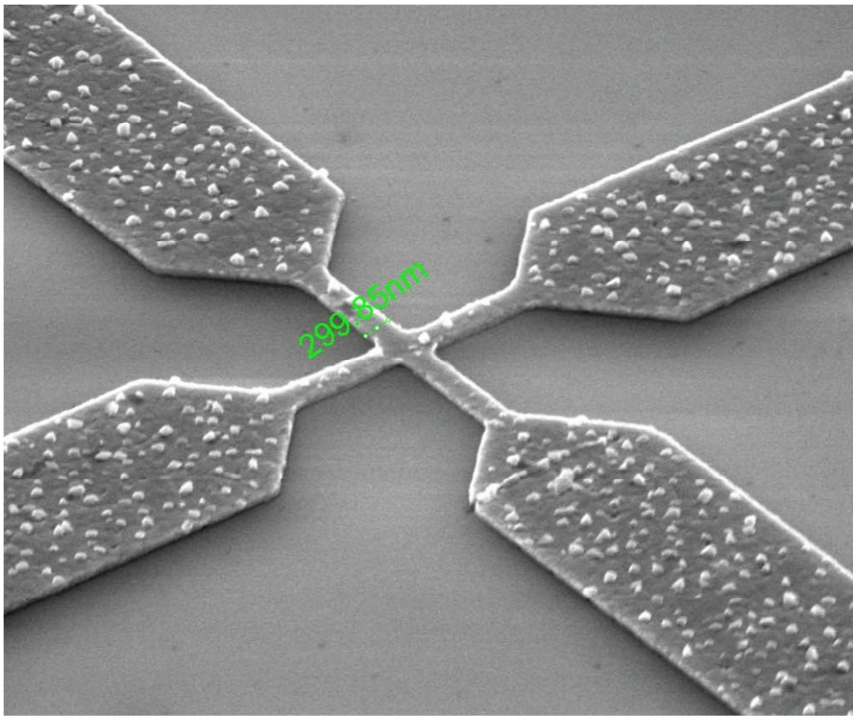

(Bismuth micro-Hall device) Kamil Lipert and Ingolf Mönch,
IFW Dresden, 27.09.2008

1. Introduction

Materials science promotes novel applications by producing novel materials with superior functionalities. In the last decades, enormous progress has been made in this respect by combined efforts of chemists, physicists, materials scientists and engineers. From a variety of approaches, downscaling well known materials into nanoscale objects is one of the most promising ways to achieve such novel functionalities. Such downscaling yields functionalities far beyond mere size reduction but there are fundamentally different physical properties arising in nanosize materials which invoke the high interest in new technological applications and attract scientists' attention because of their fundamental scientific importance.

The history of modern nanotechnology started in the 1950's when the well-known physicist Richard Feynman gave a talk on December 29th 1959 at the annual meeting of the American Physical Society entitled: "There is plenty of room at the bottom" [1]. This presentation caused a stir among scientists, because he concluded there might be the possibility to make changes in the structure of matter by manipulating single atoms. Since then, and particularly within the last decades there was a large progress in synthesis, characterization, and manipulation of matter at the nanoscale.

Nanosized materials, however, have already been used in ancient times. There are famous effects of color changes appearing upon size reduction which are related to changes of the electronic properties of materials upon downscaling. For example gold which easily forms nanoparticles, exhibits different colors depending on particle size. Another promising field of nanotechnology is application of nanoscale magnets where magnetic properties are altered due to reduced size. While for example bulk ferromagnets cooled in the absence of an external magnetic field form multi-domain patterns and hence exhibit only very small or vanishing net magnetization, size reductions straightforwardly yields single domain particles with net magnetic moments as large as their saturation magnetization. Novel effects in these single domain nanoparticles also arise if thermal fluctuations become comparable to magnetic anisotropy so that the nanomaterials behave as so-called superparamagnets. These effects are not only interesting from a fundamental research point of view but also drive a race for completely new applications in fields as different as, e.g., spintronics, data storage, and medicine.

A mandatory precondition for application is however the detailed knowledge on the magnetic response of these new nanoscale materials. Within the last two decades developments in experimental techniques provided novel methods for investigating the magnetic properties of individual nanosize magnetic grains and get insight into their properties. One of these methods is the micro-Hall magnetometry which is applied in this work in order to investigate the properties of a novel class of nanoscale magnets, i.e. ferromagnetic nanowires encapsulated inside carbon nanotubes. *Kent et al.* was the first who demonstrated the applicability of such a micro Hall device based on a GaAs/AlGaAs heterostructure containing two dimensional electron gas (2DEG) for investigating the properties of nanosize iron magnets [2]. In these studies the Hall measurements were performed on an ensemble of iron nanoparticles containing 100 - 600 nanoparticles grown by scanning tunneling microscopy (STM) assisted chemical vapor deposition (CVD) on the active area of the Hall device. A few years later in 2000 *Theil Kuhn et al*. for the first time measured an individual iron nanoparticle with magnetic moment of about $10^4 \mu_B$ [3].

The materials which have been addressed in this thesis are magnetically functionalized CNTs. They have been a subject of fundamental research since their discovery in 1991 [4]. Since then a variety of methods to synthesize these carbon structures such as arc discharge [5], laser ablation [6] and CVD [7] have been developed and improved. The interest in carbon nanotubes arises due to their extraordinary properties providing a promising potential for applications on the nanometer-scale. This holds e.g. for the electrical properties since semiconducting or metallic behavior depends on details of the morphology of the material, or for their extraordinary mechanical properties with a very large Young's modulus in the TPa regime [8]. CNTs form chemically stable shells which can be opened [9], filled with desired materials [10,11] and closed again [12,13]. Thus nanotubes can serve as containers encapsulating nanoscale materials. Carbon nanotubes can be biofunctionalized [14,15] and since it has been shown that nanotubes can be uptaken by many types of cells [16,17] this renders CNTs excellent nanocontainers for biomedical applications and drives research on their usage as drug delivery systems [18,19]. Magnetic functionalization opens further potential, because after inserting a dispersed ensemble of ferromagnetically filled CNTs into the body they can be addressed by external magnetic fields. In principle, gradient magnetic field can be used to move these objects, DC magnetic field to hold them at a desired position, and AC magnetic fields generate heating. The latter in-situ heating is particularly promising if applied for local cancer treatment by means of so-called magnetic hyperthermia [20]. This method is based on the fact that cancer cells exposed to elevated temperatures of

about 42 ^{o}C (or more) are eliminated. The particular advantage of ferromagnetic nanomaterials encapsulated in carbon shells refers to the shielding effect of the metallic encapsulates in the biological environment. Various studies have shown that, independently of the synthesis technique, the carbon encapsulated iron is efficiently protected by the surrounding shells and its magnetic properties are retained [21,22,23]. Another potential lies in the fact that various functional materials can be inserted into CNT. E.g., by filling CNT with strongly temperature dependent nuclear magnetic resonance (NMR) material i.e. CuI [24] the temperature of the hyperthermia process might be controlled [25].

The aim of this thesis is to investigate in detail the magnetic properties of magnetically functionalized CNTs, as well on the level of ensembles as - in particular - of individual entities. Hence a micro Hall magnetometer had to be set-up in a first step which is based on a GaAs/AlGaAs heterostructure with 2DEG. Patterning of Hall sensors on top of the heterostructure was done by EBL and wet chemical etching. Micromanipulation was applied in order to place the end of the nanowire, where its stray field is strongest, inside the active area of the device of size of 800 × 800 nm^2. Eventually, different individual nanowires have been studied and details of magnetization reversal have been elucidated.

The thesis starts in chapter 2 with a concise discussion of basics of magnetism with particular emphasis on the magnetic properties of nanoscale objects.

Chapter 3 is about the magnetization measurement techniques applied to study ensembles of CNT and the detailed description of principles of micro Hall magnetometry applied for studies of individual Fe–filled CNT.

Chapter 4 discusses all necessary techniques which were used for building up the micro Hall magnetometry setup. Here, we discuss the principles of the operation of the scanning electron microscope used in the work and basics of the electron beam lithography in detail. Later we emphasize on the fabrication of micro Hall devices. Then we describe the micromanipulation method used for placing nanowires in the active area of the Hall sensor. We provide a short description of the synthesis method and structural characterization of batch of CNT prepared for micro Hall measurements and at the end we focus on the electric circuit which has we used in Hall voltage measurements.

Chapter 5 presents the magnetism of CNT ensembles. We present the overall introduction to CVD preparation methods in which ferromagnetic catalysts are used. We present a method of annealing Fe catalyst-based CNTs which provides an evaporation of catalyst material and increase the carbon crystal structure quality of CNTs. The second approach consists of application of non-magnetic rhenium as catalyst material. Diamagnetism of CNT ensembles in both approaches is confirmed by the low temperature magnetization measurements. Further we discuss the influence of the remaining catalyst materials used in synthesis on the magnetic properties of carbon nanotubes.

Chapter 6 presents the discussion of the micro Hall data obtained for two individual Fe-filled CNT. On the one hand, the iron nanowires are used as model materials which demonstrate the devices performance. Subsequently, the experimental results on the magnetic properties of these nanowires are presented and discussed in detail.

Chapter 7 contains the summary of the work.

2. Basic aspects of magnetism in macro- and nano-materials

2.1. Exchange interactions

In 1906, to describe the ferromagnetic phenomenon, Weiss assumed the existence of an internal molecular field in the ferromagnetic body. However, twenty years later, Dirac and Heisenberg [26,27,28] independently explained ferromagnetism by the quantum mechanical exchange interaction between spins S_i. Heisenberg's Hamiltonian for the localized spins S_i and S_j with the exchange integral J_{ij} is given by:

$$\hat{H} = -2\sum_{i<j} J_{ij}\vec{S}_i \cdot \vec{S}_j \tag{2.1}$$

The exchange energy, which is assumed to be the same for each nearest-neighbor pair in a crystal, is:

$$E_{ex} = -2J\sum_{i<j}^{nn} \vec{S}_i \cdot \vec{S}_j \tag{2.2}$$

Clearly, for a positive exchange integral $J > 0$, the exchange energy has a minimum and ferromagnetic order with parallel alignment of spins is favored, while for a negative exchange integral i.e. $J < 0$, the resulting arrangement is antiferromagnetic.

Ferromagnetism in the 3d transition metals such as Fe, Co and Ni does not originate from the localized magnetic moments of individual atoms but it comes from freely moving 3d electrons in the crystal. The direct d-d exchange interaction model for localized magnetic moments cannot be used. The origin of the spontaneous magnetization can be explained by means of the band structure arrangement of the 3d and 4s electrons. The exchange coupling between the unfilled d shells and 4s conducting electrons leads to a relative shift of the two d spin bands which are partially covered with s band (this shift leads to a different number of spins at the Fermi level as shown in figure 2.1). Electrons are transferred between both sub-bands by reversing their spins. In fact, the kinetic energy

increases due to the occupation of higher energy levels, however the total energy decreases and ferromagnetic alignment of d spins is present.

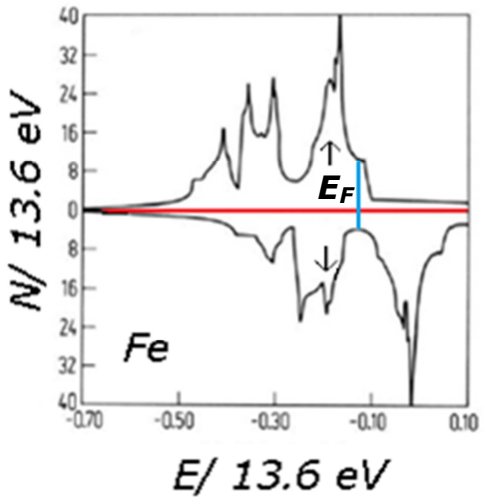

Figure 2.1: *Electronic density of states for s and d electrons in iron. Because of the exchange interactions both subbands are shifted 2.4 eV* [29].

The discussion below will be limited to the ferromagnetic case. It is known that bulk ferromagnets very often shows weak or even no average magnetic moment in the remanent state. Large ferromagnetic samples split into domains separated by domain walls. Spins inside each domain are parallel to each other however the magnetization directions between neighboring domains differs. Domains and corresponding domain walls are formed in order to reduce the magnetostatic energy associated with the demagnetization field inside a ferromagnetic body, while exchange and magnetocrystalline energies are stored in domain walls. This will be discussed in more detail in subchapters 2.2 - 2.6. For small particles it may happen that the energy necessary to create domain walls is higher than the saved magnetostatic energy, corresponding to the demagnetization field, in this case sample forms a single domain. The circumstances of formation of single domain configuration in small particles and magnetization reversal mechanisms will be discussed in subchapters 2.7 - 2.10.

2.2. Magnetocrystalline anisotropy

The manifestation of the magnetocrystalline anisotropy in single crystals of base ferromagnets Fe, Co and Ni is shown in figure 2.2. For bcc iron the easy axes lie along the

<100> directions while the hard axes lie along the <111> directions. The magnetic field which needs to be applied to saturate iron is much smaller in the <100> directions than in others. In the case of fcc nickel the easiest directions are <111> while the hard lies along the <100>. Cobalt has a hexagonal crystal structure and the easy axis magnetization direction is the c axis. To saturate Co crystal in the basal plane the magnetic field has to be one order of magnetitude higher than in the case of Fe in the hard direction. In the absence of an external magnetic field the magnetization tends to lie along the easy direction.

The magnetic field which needs to be applied to saturate the sample in the hard direction is the so called anisotropy field H_A. Magnetocrystalline energy shows numerous symmetries, however the cubic and uniaxial ones described above match the majority of cases. For cubic symmetry the energy density of magnetocrystalline anisotropy can be written [30]:

$$\frac{E_{mc}}{V} = K_0 + K_1\left(\cos^2\alpha_1\cos^2\alpha_2 + \cos^2\alpha_2\cos^2\alpha_3 + \cos^2\alpha_3\cos^2\alpha_1\right) + K_2\left(\cos^2\alpha_1\cos^2\alpha_2\cos^2\alpha_3\right) + \ldots \quad (2.3)$$

where K_0 is independent term of orientation of M (magnetic moment), α_1, α_2, α_3, are the angles between the magnetic moment and the three coordinate axes. The experimental room temperature anisotropy constants equal K_1 = 0.048 MJ/m^3 and K_2 = - 10 kJ/m^3, and K_1 = - 4.5 J/m^3 and K_2 = - 2.3 kJ/m^3 for iron and nickel, respectively. [30]

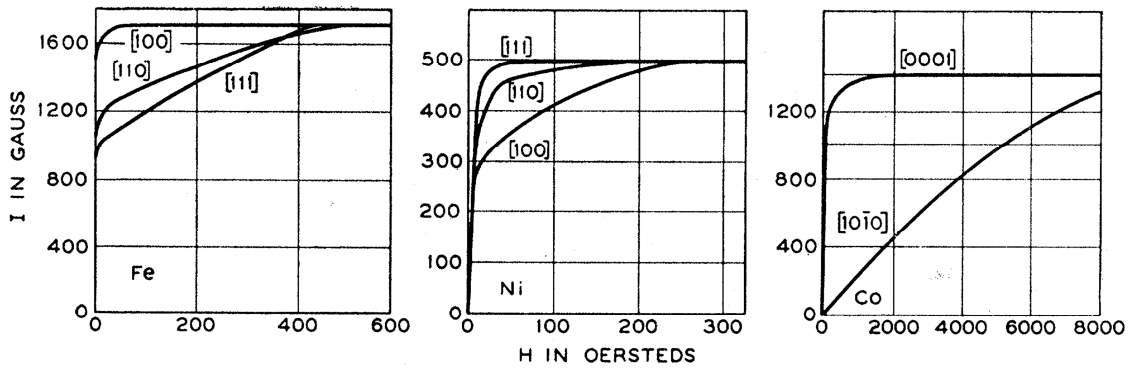

Figure 2.2: *Magnetization curves measured along easy, mid-hard and hard magnetic directions for single crystal. (a) Iron, (b) nickel and (c) cobalt.[31]*

For uniaxial symmetry the magnetocrystalline energy density is given by [30]

$$\frac{E_{mc}}{V} = K_0 + K_1 \sin^2\theta + K_2 \sin^4\theta + ... \tag{2.4}$$

where θ is the angle between the easy axis and magnetic moment, K_1 and K_2 are the anisotropy constants. For most purposes it is sufficient to keep only the first three terms in the above equation. The experimentally measured at room temperature anisotropy constants for cobalt equal $K_1 = 0.53$ MJ/m^3 and $K_2 = 0.14$ MJ/m^3.
The origin of the magnetocrystalline anisotropy is a quantum effect in contrast to the shape anisotropy which originates from the dipole interactions arising from magnetic poles at surface.

2.3. Shape anisotropy

The internal magnetization of a ferromagnetic sample leads to a so-called stray field. Inside the sample the stray field has often an opposite direction to the magnetization and is called the demagnetization field H_d. For ellipsoids the relation between the demagnetization field and magnetization can be expressed as follows [32]:

$$\vec{H}_d = -N_d \vec{M} \tag{2.5}$$

Where N_d is so called demagnetization factor. The magnetostatic energy of the ferromagnetic body equals [32]:

$$E_s = \frac{1}{2V} \cdot \left(N_x m_x^2 + N_y m_y^2 + N_z m_z^2\right) \mu_0 \tag{2.6}$$

where V is the volume of sample, N_x, N_y, N_z are the demagnetizing factors for axes x, y, z, respectively and m_x, m_y, m_z are the components of the magnetic moment.
Basically, magnetic shape anisotropy arises due to the body shape, and the easy axis of magnetization is in the direction for which the magnetostatic energy is the lowest. Thus, for example, in thin film layers with small magnetocrystalline anisotropy the spontaneous magnetization completely lies in the layer plane, whereas, for elongated samples the magnetization lies preferably along the longitudinal axis.

For the single domain nanoparticle the magnetostatic energy can be expressed exactly only for particles with ellipsoidal shape. For the ellipsoid of revolution with the major axis along the z direction demagnetizing factors can be written [32]:

$$N_z = \frac{1}{n^2 - 1} \cdot \frac{n}{\sqrt{n^2 - 1}} \ln\left(n - 1 + \sqrt{n^2 - 1}\right)$$

$$N_x = N_y = \frac{1 - N_z}{2} \tag{2.7}$$

Where n = p/a is the ratio of the semi axes of the ellipsoid.
E_s has uniaxial symmetry and for a prolate ellipsoid the anisotropy constant is positive, which means that the easy axis is the principal axis. For uniaxial magnetocrystalline energy and if the two easy axes coincide (which is often the case), the two constants add. For a sphere there is no shape anisotropy. The shape is isotropic.

2.4. Other magnetic anisotropies

Besides the shape and magnetocrystalline anisotropy other types of magnetic anisotropy exist and are called: magnetoelastic, surface and exchange anisotropy.
The magnetoelastic anisotropy is related to the magnetostriction effect, and to external and internal strains. Magnetostriction is the extension or constriction of the crystal upon the rotation of magnetic moment. For a spherical shaped nanoparticle and in the presence of external strain σ the magnetoelastic energy can be expressed [32]:

$$E_\sigma = -\frac{3}{2} \lambda_s \cdot \sigma \cdot \cos^2 \alpha \tag{2.8}$$

where α is the angle between the magnetization and strain axis, λ_s is the magnetostriction saturation. If $\lambda_s\sigma > 0$ (positive magnetostriction and tensile strains or negative magnetostriction and compressive strains) then the easy axis is determined along the strain axis. In the other case when $\lambda_s\sigma < 0$ then there is an easy plane.

The other type of magnetic anisotropy is related to the surface effects. A free surface results in a discontinuity of the magnetic interactions. This originates in the magnetostatic

energy but in parallel in surface energy. In the cubic symmetry, the surface energy can be expressed [32]:

$$E = K_s \cos^2 \psi \tag{2.9}$$

where ψ is the angle between the magnetization and the perpendicular to the surface.
The exchange anisotropy was discovered in 1966 by Meiklejohn and Bean [33] for tiny cobalt nanoparticles coated with a thin CoO layer. It is manifested by the shifting of the hysteresis loop (asymmetric coercive fields) after field cooling. The source of the anisotropy is a preferential magnetization direction of the ferromagnet due to the exchange coupling to the antiferromagnet.

2.5. Magnetic domains and domain walls

Even though most neighboring spins are aligned parallel to each other in a ferromagnetic sample, it often shows a very small or even no global magnetization. The reason for this is that the sample is divided into domains (i.e. areas in which the spins are parallel) whose magnetic moments cancel out. The change of the direction of the magnetization between neighboring domains is not sharp but takes place gradually and this transition area is called the domain wall. Domains form to minimize the magnetostatic energy which arises from the magnetic poles at the sample surface, however it costs additional energy, exchange and magnetocristalline which is stored in the domain walls. Figure 2.3 shows the ferromagnetic sample with different domain configurations. As seen in figure 2.3a, where the sample consists of a single domain, the magnetostatic energy is large. If the sample is divided into two domains with opposite magnetizations the magnetostatic energy becomes smaller. Further dividing of the sample into four domains still further decreases the energy (Fig. 2.3c). Finally the magneostatic energy is minimal when the domain magnetization directions form a closed loop (Fig. 2.3d). The exact domain configuration in the ferromagnetic sample arises from the balance between the saved magnetostatic energy and energies consumed for formation of domain walls. As already mentioned, the transition of the magnetization direction between the domains is not sharp but it takes place by continuous rotation of the magnetization direction, usually over a few hundred atomic monolayers. The exchange interactions tend to keep the next neighbor

spins in the parallel configuration, thus broadening the width of domain wall decreases the contribution of exchange energy, while the magnetocrystalline anisotropy energy is minimal when number of spins deviating from the magnetocrystalline easy axis is minimal.

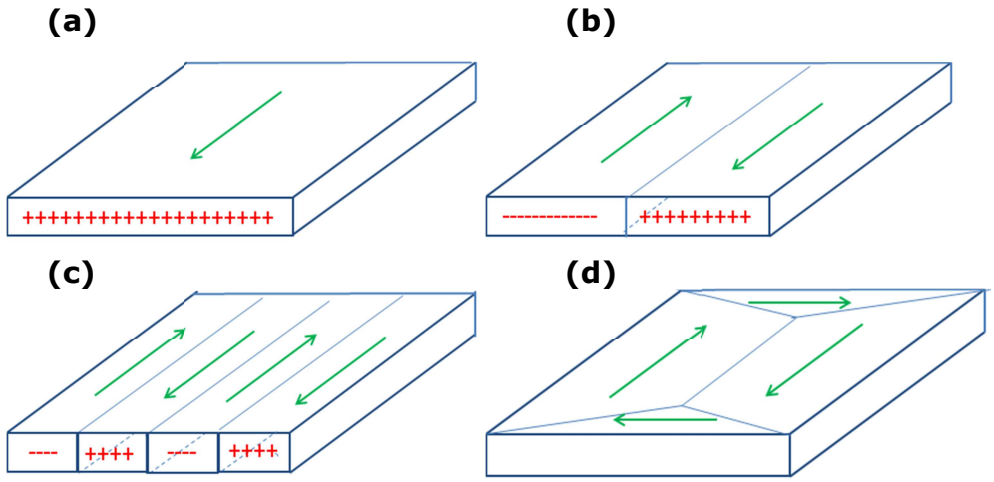

Figure 2.3: *Formation of domains in ferromagnetic material. The exact domain configuration arises from the balance of the energies, magnetostatic saved by formation of domains and those stored in domain walls. (a) Saturated sample, single domain, large magnetostatic energy, (b) introducing 180^{o} domain wall reduces the magnetostatic energy but it costs additional energy needed for its formation, (c) the magnetostatic energy is further decreased when four domains are formed, (d) in the case when closed domain loop is formed the magnetostatic energy is minimal but at a cost of a large increase in magnetocrystalline anisotropy energy in uniaxial materials [30].*

The width of the domain wall tends to minimize the overall contributions from exchange and magnetocrystalline anisotropy energy.

In general the domain wall thickness can be expressed [30]:

$$\delta_{dw} = \pi\sqrt{\frac{\mathbf{A}}{\mathbf{K}}} \qquad \text{for Bloch wall} \qquad (2.10)$$

$$\delta_{dw} = \pi\sqrt{\frac{\mathbf{2A}}{\mathbf{K}}} \qquad \text{for Néel wall} \qquad (2.11)$$

where A is the exchange constant and K is attributed to anisotropy.

The sketch of Bloch and Néel walls is shown in figure 2.4. Bloch domain walls are typical for bulk samples whereas Néel domain walls are seen in thin films. In the Bloch type wall the magnetization vector rotates parallel to the wall plane which results in the appearance of magnetic poles at the sample surface (Fig. 2.4a). When decreasing the thickness of the film the magnetostatic energy associated with the magnetic poles increases and to minimize this energy the spins rotate in such a manner as is shown in figure 2.4b.

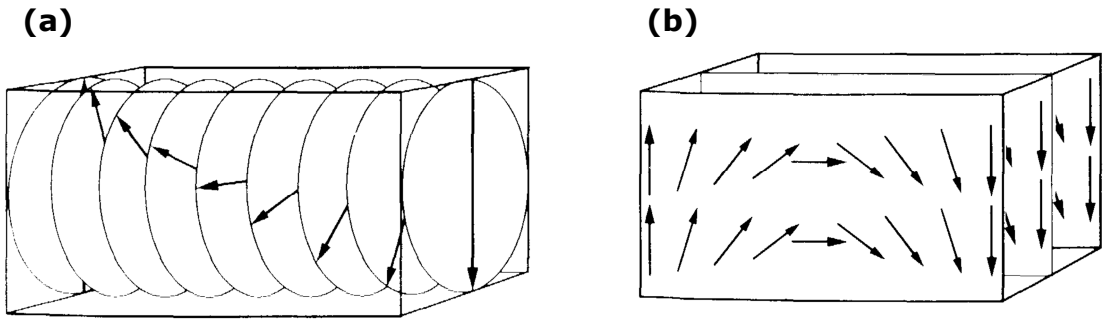

Figure 2.4: *Domain walls separating neighbor domains with opposite magnetization direction. (a) Bloch type, typical for bulk material, (b) Néel type, characteristic for thin films [34].*

2.6. Magnetic hysteresis loop in multidomain material

The magnetic domain configuration of the demagnetized ferromagnetic sample is such that M = 0 in the absence of an external magnetic field (Fig. 2.5a). Upon application of an external magnetic field the domain walls start moving in such a manner that the parts of the sample having the highest M component in the field direction expand. After both processes (domain wall motion and rotation of magnetization vector) are completed the sample reaches the saturation state M_s (Fig. 2.5a). When the external magnetic field decreases, the magnetization vector rotates back to the easy direction, in The energy of each domain is $U = - \mu_0 \mathbf{M} \cdot \mathbf{H} V$, where V is the volume of the domain and M is its magnetization. After the domain walls complete their motion the sample often forms single domain and its magnetization rotates towards the magnetic field direction. The energy needed to rotate the magnetization vector from an easy direction is higher than that needed for domain wall motion. general this process is without hysteresis. When the external magnetic field is further decreased the domain walls start to move back across the sample. In an ideal ferromagnet the displacement of a domain wall requires very little

energy. However, real ferromagnetic materials consist of inclusions and constrictions, so called pinning centers. These local defects influence the movement of the domain walls, because they locally induce magnetic anisotropy deviations leading to pinning of the domain walls at the defects. Only if the external field is large enough the wall becomes depinned and it jumps abruptly and irreversibly to the next pinning center. This opens up the loop and causes hysteresis. When the field reaches zero, some average spontaneous magnetization is still present called remanent magnetization M_r. In order to restore the state in which an average magnetization is zero, a negative field needs to be applied called the coercive field. As the magnetic field closes the cycle the H - M hysteresis loop is formed (Fig. 2.5b). The area inside the loop is the work done by the external magnetic field in one cycle, which is dissipated as a heat [30].

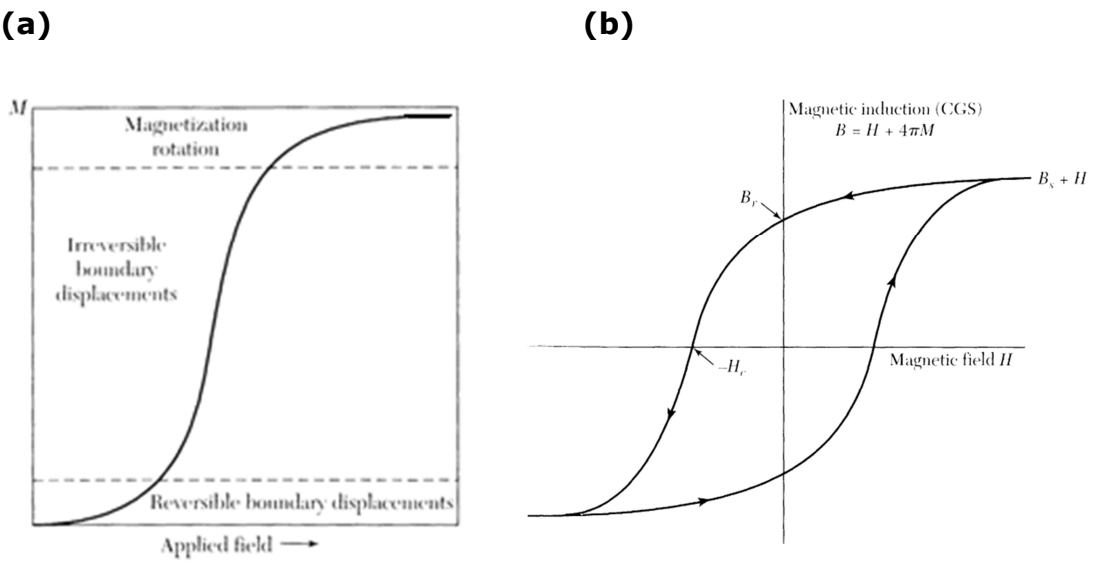

Figure 2.5*: (a) Virgin magnetization curve of a ferromagnet with multi-domain structure. The dominant processes are given for different field ranges, (b) hysteresis loop of ferromagnetic material showing the variation of magnetization M as a function of external magnetic field H.[35]*

2.7. Magnetic domains in nanoparticles

Under certain circumstances a ferromagnetic particle becomes single domain in the remanent state. At first it might be assumed that the critical diameter of the particle i.e. the diameter below which it becomes single domain, should be comparable to or lower than the domain wall width ($d \leq \pi \cdot (A/K)^{1/2}$) such that the domain wall cannot be formed. For

the single domain configuration to be stable in a spherical particle of radius r, the energy which is stored in the domain wall equals:

$$\sigma_{dw}\pi r^2 = 4\pi r^2 (AK)^{\frac{1}{2}} \tag{2.12}$$

where σ_{dw} is the domain wall energy per unit area, A is the exchange constant and K is the effective anisotropy constant. σ_{dw} has to be higher than the magnetostatic energy which is saved by the formation of two domains (roughly equal to half the single domain energy) [36]:

$$\Delta E_{ms} = \frac{1}{12}\mu_0 M_s^2 V = \frac{1}{9}\mu_0 M_s^2 \pi r^3 \tag{2.13}$$

The critical radius r_c of the sphere below which it becomes single domain can be then calculated by equating both energies, giving:

$$r_c = 36\frac{(AK)^{1/2}}{\mu_0 M_s^2} \tag{2.14}$$

Taking into account values A = 10^{-11} J/m, K = 48 kJ/m the critical radius for spherical iron nanoparticle is $r_c \approx 6$ nm.

2.8. Stoner - Wohlfarth model

Uniform magnetization reversal of a single domain nanoparticle is referred to as the Stoner - Wohlfarth model [37,38]. The critical size (radius of spherical nanoparticle below which it becomes a single domain in the absence of external magnetic field) calculations do not rule out the possibility that the nanoparticle loses its single domain configuration during magnetization reversal. The coherent process of magnetization reversal is favorable for very small magnetic particles of a few nanometers. For larger, but still single domain magnetic particles nonuniform modes dominate. There is an assumption that the magnetization value remains constant for all values of applied external magnetic field. Consider an elongated spheroid shown in figure 2.6a with

negligible magnetocrystalline anisotropy and mechanical strain. The free energy density of such a prolate spheroid under the application of external magnetic field can be then written as:

$$f = K_u \sin^2(\theta - \theta_0) - \mu_0 H M_s \cos\theta \tag{2.15}$$

There are two stable orientations of magnetic moment parallel and antiparallel to the easy axis separated by the energy barrier of the high K_uV at H = 0 as shown in figure 2.6b (black curve) which in the absence of external magnetic field are energetically equal. Under the application of the magnetic field the double energy well becomes asymmetric and the effective barrier decreases (see Fig. 2.6b (green, red and blue curves)). When the external magnetic field reaches the switching field H_{sw}, the barrier vanishes and the magnetization switches irreversibly (blue curve). The value of the switching field and its angular dependence provides the information about the mechanism of magnetization reversal.

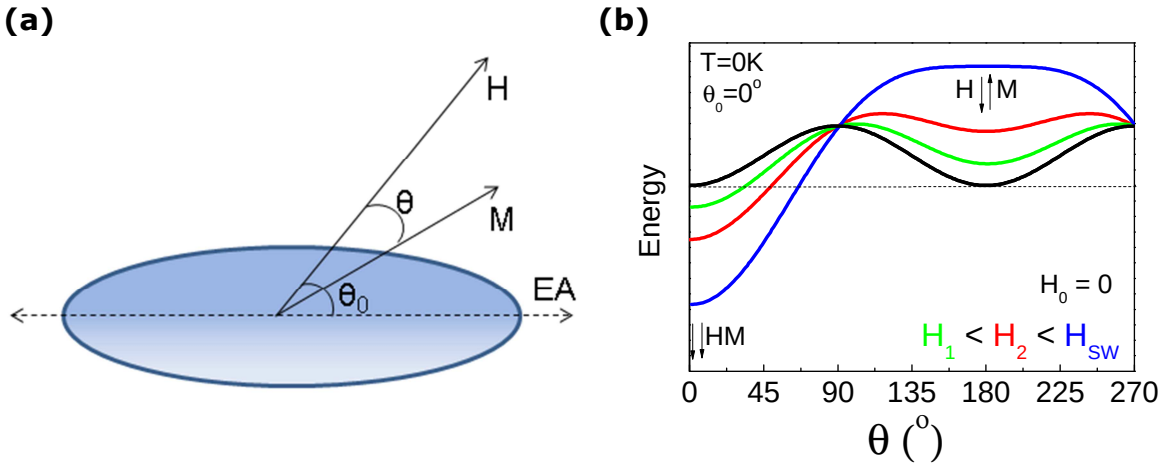

Figure 2.6: *(a) Single domain nanoparticle with negligible magnetocrystalline anisotropy. The easy magnetization axis (EA) lays along the long axis of the particle. Magnetic field is applied with angle θ_0 with respect to the easy axis. θ is the angle between the magnetization vector and easy axis, (b) the energy configuration in the absence of external magnetic field (black curve) and under the application of external magnetic fields with different strengths (green and red curves) in the parallel direction to the easy magnetization axis (θ_0 = 0). Switching of magnetization takes place when energy barrier vanishes at magnetic field H_{sw} (blue curve). Arrows represent vectors of magnetization and magnetic field respectively. Thermal fluctuations are neglected (T = 0 K)* [30].

The minimum of free energy density is the first derivative of θ compared to zero:

$$2K_u \sin[2(\theta - \theta_0)] + \mu_0 H M_s \sin\theta = 0 \qquad (2.16)$$

By replacing the $K_u=\mu_0 H_A M_S/2$ and $h=H/H_A$, where H_A is the anisotropy field one obtains:

$$\sin[2(\theta - \theta_0)] + 2h \cdot \sin\theta = 0 \qquad (2.17)$$

and again by replacing $m=M/M_S=\cos\theta$, one gains the solution:

$$2m(1-m^2)^{1/2}\cos 2\theta_0 + \sin 2\theta_0 (1-2m^2) \pm 2h(1-m^2)^{1/2} = 0 \qquad (2.18)$$

The solution of the above equation is shown in figure 2.7. For $\theta_0 = 90^o$ the equations reduce to $2K_u\cos\theta = M_S H$ which provides the linear M - H characteristics.
For $\theta_0 = 0^o$, m = 1 and the remanent magnetization equals the saturation magnetization. In this limit the hysteresis loop results in a square shape.

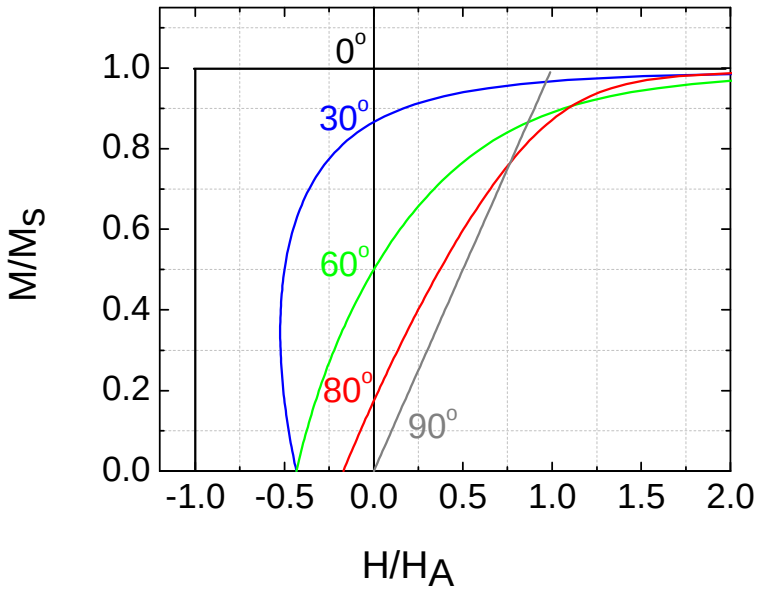

Figure 2.7: *Solutions for the Stoner - Wohlfarth model. Reduced magnetization M/M_s vs. reduced magnetic field H/H_A. M_s represents saturation magnetization whereas H_A is anisotropy field. θ_0 = 0^o, 30^o, 60^o, 80^o, 90^o, represents the angles between applied magnetic field and easy axis of magnetization.*

The switching takes place when the free energy density minima $df/d\theta=0$ becomes flat so that $d^2f/d\theta^2=0$ (cf. figure 2.6b):

$$h_s \cos\theta - \cos 2(\theta - \theta_0) = 0 \tag{2.19}$$

It is possible to eliminate $\cos2(\theta-\theta_0)$ and express $\sin2\theta_0$ as a function of h_S:

$$\sin 2\theta_0 = \left(\frac{2}{h_s^2}\right)\left[\frac{1-h_s^2}{3}\right]^{3/2} \tag{2.20}$$

Solving the equation 2.20 gives the values of the switching field, as a function of the angle θ_0:

$$h_s = \left(\cos^{2/3}\theta_0 + \sin^{2/3}\theta_0\right)^{-3/2} \tag{2.21}$$

The equation 2.21 describes the angular variation of the switching field in the case when the magnetization reversal of the nanowire takes place via coherent rotation. This dependence is shown in figure 2.8. The characteristic feature of the dependence is the maximum at $\theta_0 = 0$ which distinguishes coherent rotation from a nonuniform process and provides a means to discriminate the coherent process from an incoherent mode [30].

2.9. Nonuniform magnetization reversal

The simplest nonuniform mode is the so called curling mode as developed in a model by Brown [39]. The critical parameter in this model is the exchange length $\lambda = (A/\mu_0 M_S^2)^{1/2}$ (A is the exchange constant) determining the region in which the transition from coherent rotation to nonuniform mode takes place. In case of a cylinder with radii $r < \lambda$ the coherent rotation is favorable, whereas in the opposite case $r > \lambda$, non coherent modes dominate. The spin configuration during magnetization reversal by means of coherent rotation and curling mode is shown if figure 2.9a. During the magnetization reversal in the coherent manner the exchange energy is saved while it cost much of the dipolar energy. In curling mode magnetization reversal the dipolar energy is

saved because fewer spins are pointing away from the easy axis but it cost a lot of exchange energy since spins are not parallel. The variation of the switching field with angle θ_0 between the long axis of the ellipsoid and the magnetic field has been given by Aharoni [40]:

$$H_{SW} = \frac{\mu_0 M_s}{2} \cdot \frac{a_x \cdot a_z}{\sqrt{a_z^2 \sin^2 \theta_0 + a_x^2 \cos^2 \theta_0}} \tag{2.22}$$

where $a_{x,z} = 2N_{x,y} - k/S^2$, $N_{x,y}$ are demagnetizing factors, $S = d/ d_0$, $d_0 = 2 \cdot (A/\mu_0 M_s^2)^{1/2}$ and d is major axis of the ellipsoid. The parameter k is a function of the aspect ratio of ellipsoid. For an infinite cylinder k = 1.079 while for a sphere k = 1.379. For an infinite cylinder equation 2.22 with an angle θ_0 defined as the angle between the easy axis of the nanowire and external magnetic field becomes [41]:

$$H_{SW} = \frac{\mu_0 M_s}{2} \cdot \frac{a(1+a)}{\sqrt{a^2 + (1+2a)\cos^2 \theta_0}} \tag{2.23}$$

where, $a = -1.079 \cdot (d_0/d)^2$.

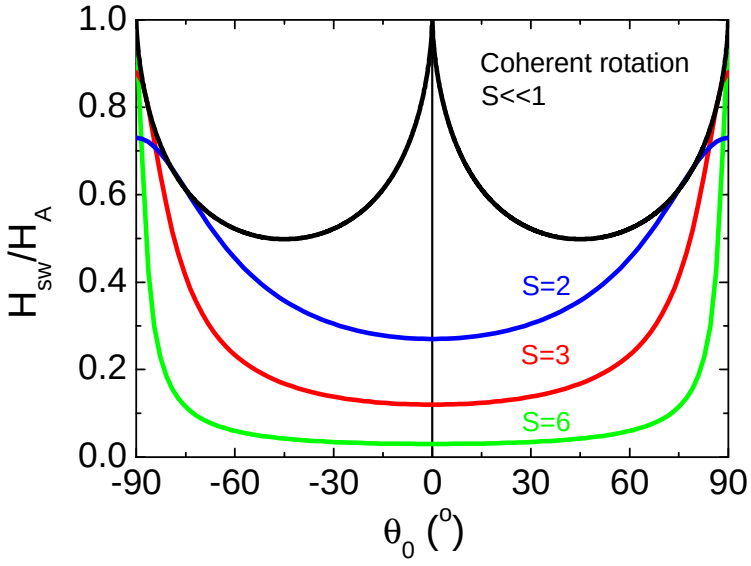

Figure 2.8: *Angular variation of the switching field for an infinitely long ferromagnetic nanowire. Black line (S << 1) represents the rotation in unison (Stoner - Wohlfarth model), while for the rest (nanowires with different diameters d) of the lines the curling mode takes place.*

The other mode of incoherent magnetization reversal process is the so called buckling mode, first studied by Frei [42]. For an infinite cylinder, this mode of reversal is represented by periodic fluctuations of magnetization around the long axis of the cylinder. During magnetization reversal spins remain almost parallel in the plane perpendicular to the axis. The spin orientation depends only on the z coordinate (Fig. 2.9a).

In general the type of magnetization reversal in the magnetic nanowire strongly depends on the nanowire diameter d. Curling mode is observed when S (= d/ d_0) > 1.1 while the buckling mode is observed for S < 1.1 and it approaches the Stoner - Wohlfarth model for S << 1. The transition from buckling to coherent rotation is not sharp and near S = 1 a mixed mechanism takes place.

The schematic illustration of the spin configuration for the three modes of magnetization reversal is shown in figure 2.9a. The reduced nucleation field as a function of reduced radius is shown in figure 2.9b.

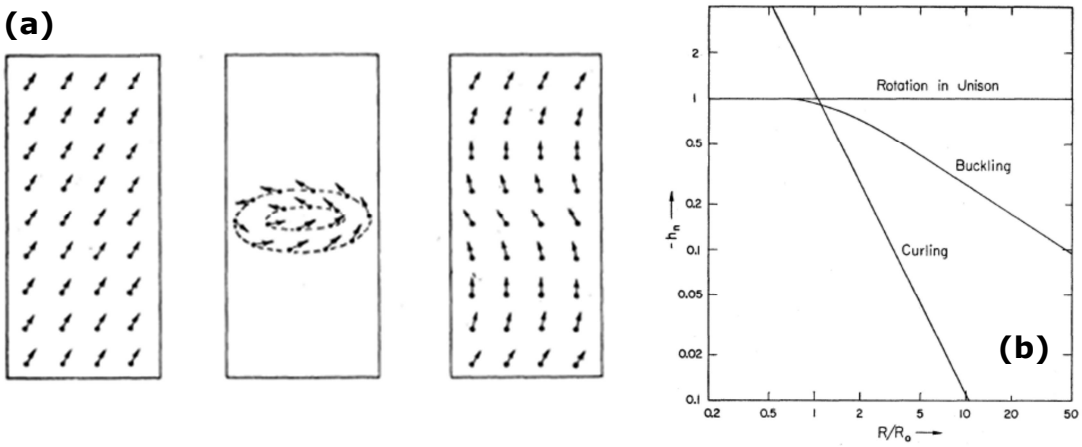

Figure 2.9: *(a) Spin orientation for three modes of magnetization reversal in infinitely long ferromagnetic nanowires. From left: coherent rotation, curling and buckling mode, (b) theoretical plot of the dependence of the nucleation field vs the reduced radius of ferromagnetic nanowires for different magnetization reversal modes. [43]*

2.10. Thermal relaxation of magnetic moment

The dynamic properties of nanosize magnets are characterized by the relaxation time τ of the magnetic moment of the particle via the Arrhenius formula.

$$\tau = \tau_0 \cdot e^{\frac{E_B}{k_B T}} \tag{2.24}$$

where τ_0 is a length of time, characteristic of the material, called the attempt time and typically in the range 10^{-10} - 10^{-8} s, k_B is the Boltzmann constant and T is temperature.
$E_B = KV$ is the energy barrier associated with magnetic anisotropy, V is the volume of the particle and K is the effective magnetic anisotropy constant including contributions from various types of anisotropies

For very small particles the energy barrier is small which leads to very short τ and under conditions $\tau_m > \tau$, where τ_m is the time of measurement, superparamagnetism is observed and coercivity equals zero. To be specific, for spherical Fe nanopartcicle with magnetocrystaline anisotropy $K = 10^5$ J/m^3, the superparamegnetic radii for stability over 1 s equals about 6nm, while for stability over one year it is about 7.3 nm. In case of magnetic nanowires the energy barrier is high (Fe nanowire with diameter d = 26 nm and length L = 15µm $E/k_BT \approx 10^4$) thus τ is extremely large and the magnetic moment is stable.

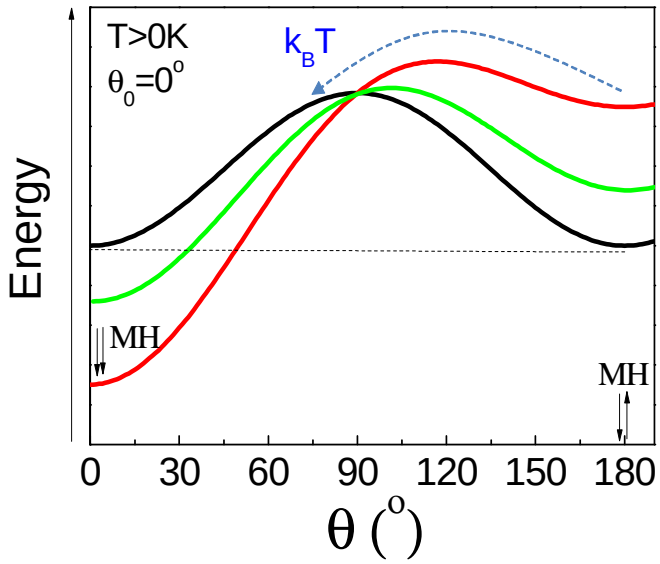

Figure 2.10:
Thermally activated switching process. At a certain energy barrier height ($E_B \leq K_BT$), thermal fluctuations can initialize the switching process.

The basic switching behavior with a single energy barrier shown in figure 2.6 is only valid at T = 0 K. In real scenario thermal fluctuations meant above play a role in the process of magnetization reversal and cannot be neglected. As shown in figure 2.10 at a certain energy barrier height comparable to thermal energy k_BT, these fluctuations can already kick the magnetization over the energy barrier and initialize magnetic switching.

This is so called a thermally activated magnetization reversal process in which the average switching field follows the formula [44]:

$$< H_{sw} >= H^0 \left(1 - \left(\frac{k_B T}{E_0} \ln(cT/v) \right)^{\frac{2}{3}} \right) \tag{2.25}$$

where H^0 is the switching field at temperature T = 0 K, k_B is the Boltzmann constant, E_0 is the energy barrier in absence of an external magnetic field, v is the sweeping field rate, $c = k_B H^0/(\tau_0 E_0)$, τ_0 is the prefactor of the thermal activation rate $\tau = \tau_0 \exp(E/k_B T)$ and $E = E_0 \cdot (1-H/H_0)^{3/2}$ is the energy barrier dependence on the external magnetic field.

3. Magnetic measurement techniques

3.1. Magnetometry techniques for characterization ensembles of carbon nanotubes

Low temperature characterization of CNT ensembles has been performed on the superconducting quantum interference device (SQUID) (Quantum Design MPMS®-XL). The SQUID consists of a superconducting loop containing two Josephson junctions. A superconducting loop will contain flux only in multiples of the quantum flux, i.e. $n\Phi_0$, where n is any integer and $\Phi_0 = h/2e$. A change in magnetic flux which is applied to the loop will result in a current which flows oppositely to this change. As a result of this a phase difference occurs across the junction which finally results in a voltage across the loop. This voltage is detected. [45]. The magnetization sensitivity of the device equals 10^{-8} emu [46]. The device used in experiments has been calibrated by the manufacturer.

Room temperature measurements were performed by means of an alternating gradient magnetometer (AGM) (2900, Princeton Measurement Corporation).

Setup utilizes an alternating field gradient to create a periodic force which acts on the magnetized sample. This gradient field is applied along x axis while the sample is attached to the tip of a vertical rod (along z axis) and can be rotated around the z axis. The top end of the rod is attached to the bottom part of a piezoelectric element. A direct current (DC) applied to the electromagnetic coils causes the appearance of a DC magnetic field along x axis ($\mu_0 H_{max} = 1.1$ T) which magnetizes a mounted sample. A gradient field results in the force which acts on the magnetized sample and causes the bending moment on the piezoelectric element which generates the voltage. The voltage strength is proportional to the force on the sample. This voltage is synchronously detected at the frequency of the gradient field. The measured voltage amplitude is proportional to magnetic moment of the sample [47]. The magnetometer is calibrated with a thin Nickel (Ni) film which produces the saturation moment $M_s = 5 \cdot 10^{-4}$ emu. As well as for the SQUID, the magnetic moment sensitivity of the device is 10^{-8} emu [48].

3.2. Micro Hall magnetometry

3.2.1. Introduction to experimental techniques detecting magnetization switching via probing magnetic stray fields

As mentioned previously, commercial magnetometers offer the magnetic moment sensitivity of about 10^{-8} emu, which corresponds to the value $\approx 10^{15}$ μ_B ($\mu_B = 9.274 \cdot 10^{-24}$ emu [49]). The magnetic moment of a typical Fe-filled carbon nanotube (diameter of Fe nanowire d = 20 nm and its length l = 10 μm) is $\approx 10^9$ μ_B. Thus only the methods with elevated magnetic moment sensitivity can be applied for investigation of individual micro- and nano-scale magnets.

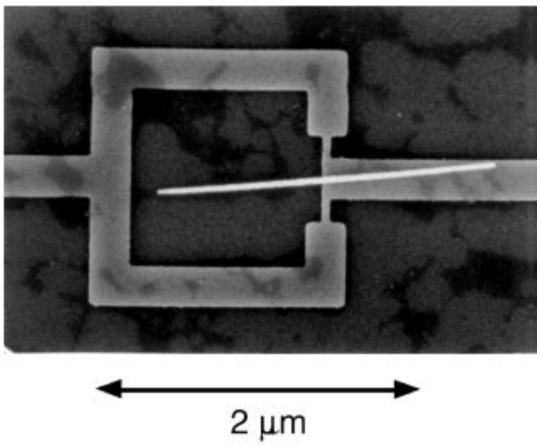

Figure 3.1: *SEM image of a dc SQUID and a Ni wire with 65nmin diameter inside the loop [50].*

Within the last two decades a variety of experimental techniques have been developed for this purpose. The micro Hall magnetometry, along with the micro SQUID and the magnetic force microscopy (MFM), belongs to the class of experimental methods for detecting stray fields of magnetic nanoparticles and probing their magnetization reversal via detecting changes of the stray fields. Micro SQUID (Fig. 3.1) has been successfully implemented for measurements of individual magnetic particles by *Wernsdorfer et al*. in 1995 [51]. The typical device used in that work consists of a very small pickup area of around 1 - 4 μm^2 prepared with few tens of nanometers of Niobium (Nb) or Aluminum (Al) thin films. It has been shown that the magnetization reversal of Cobalt (Co) nanoparticles with 2 - 3 nm in diameter, what corresponds to magnetic moment 10^3 μ_B

could be detected by micro SQUID [52].

The disadvantage of using the micro SQUID device often arises from the critical temperature of the material it is made of. For example, the Nb micro SQUID can operate only in the temperature range up to 7 K. Micro SQUID made of Al for instance can operate only up to 0.6 K. In recent years, however, the measurement techniques using the micro SQUID device were improved which let to extend the temperature limit up to 30 K [53] and by using high temperature superconducting thin films of $YBa_2Cu_3O_{7-\delta}$ (YBCO) (with potential magnetic moment sensitivity 10^6 μ_B) operating up to temperatures 70 K [54].

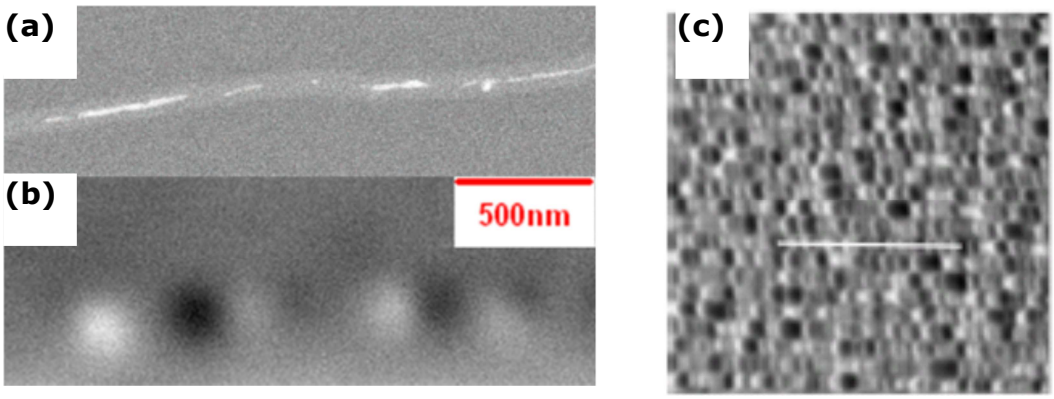

Figure 3.2: *(a) BSE SEM picture showing Fe nanowires filled carbon nanotube, (b) corresponding MFM image, showing single domain behavior of each nanowire [55], (c) MFM image of the hard drive surface with 3·3 μm^2. Each domain size is around 30·60 nm^2 [56].*

The MFM is a scanning force technique which probes the magnetostatic interactions of the magnetic tip brought close to a sample surface with the stray fields emanating from a magnetic sample. For this, a cantilever containing an atomically sharp magnetic tip attached at its end scans the surface of the sample. Using the MFM lift mode® (Digital Instruments) these local magnetostatic interactions are measured. The method consists of a two-pass scan over the sample. The magnetic signal is measured during the second pass at a constant height from the sample. This dynamic method of imaging offers high sensitivity, excluding greatly the topographic features in the magnetic image. Even though, a certain cross-talk between topography and magnetic signal cannot be avoided due to the non-perfect feedback and tip radius effects.

The principle of the magnetic image creation can be shortly explained as changes in the cantilever spring constant ($C^* = C - \partial F/\partial z$) caused by the interaction of the stray fields of

the tip and the sample. In this case C is the natural spring constant of the cantilever and the factor $\partial F/\partial z$ is the derivative of the force acting on the tip in the perpendicular direction. The change of the spring constant either by attraction $\partial F/\partial z > 0$ or repulsion $\partial F/\partial z < 0$ modifies the resonant frequency of the cantilever, which leads to a vibration phase shift. These changes, either vibration phase shift for a fixed frequency or resonant frequency for a fixed phase are detected by a deflection sensor and the MFM image is created as the spatial variation of either tip vibration resonant frequency or phase shift (Fig. 3.2). The technique can be successfully employed for investigation of switching of magnetic nanostructures. However it is important to point out that an external magnetic field applied in the experiments can influence the magnetization of the tip. Moreover, the stray field of the tip can initiate a magnetization reversal process in the sample [57].

Micro Hall magnetometry offers almost no limit for the external magnetic fields which can be applied in experiments. The device is built on the n-doped GaAs/AlGaAs heterostructure with 2DEG and can operate at relatively high temperature ranges. It has been shown by *Schuh et al*. that the device can still detect the individual Ni pillar with diameter of around 170 nm and height greater than 300 nm at temperatures as high as 225 K [58]. In contrast to MFM, micro Hall magnetometry is a noninvasive method. The current of $\approx 2\mu A$ is injected to the device and creates only negligible magnetic field (< 10 μT) acting on the sample (the distance between 2DEG plane and nanoparticle usually varies between 100 - 150 nm). In comparison to the micro SQUID performance, the moment sensitivity of micro Hall device is worse. It has been shown that the GaAs/AlGaAs-based micro Hall devices can reach a magnetic moment sensitivity as low as $10^4\ \mu_B$ [59] which is at least one order of magnitude higher than the moment sensitivity of micro SQUIDs. The detailed principles of the micro Hall magnetometry will be given in subchapter 3.2.2.

3.2.2. Ballistic Hall magnetometry

The Hall effect was discovered experimentally in 1879 by Edwin Herbert Hall in 1879 [60]. This effect has been widely used in experimental solid state physics for the determination of carrier concentration and type (viz. electrons or holes). Many commercial field sensors which are based on the Hall effect are built using a variety of semiconducting materials [61]. A Hall sensor can be described as a four terminal device in which current is injected in longitudinal direction x and the Hall voltage is measured in the transversal direction y.

In the absence of an external magnetic field the measured Hall voltage is zero. As soon as the device is exposed to a non-zero magnetic field, the Lorentz force on electric charges proportional to the z component of the external magnetic field emerges. This deflects the trajectories of the electric charges, resulting in the emergence of a transversal Hall voltage. The application of the sensor for investigating magnetic properties of nanosize magnets lays in the measurement of the Hall voltage induced by an inhomogeneous stray field of the nanomagnet inside the active area of the device (Fig. 3.3). In particular the micro Hall device probes the z-component of the stray field penetrating the crossing section of the device. Moreover by application of the external magnetic field it is possible to measure changes of the stray field related to changes of the magnetization of the nanomagnet as a function of external magnetic field.

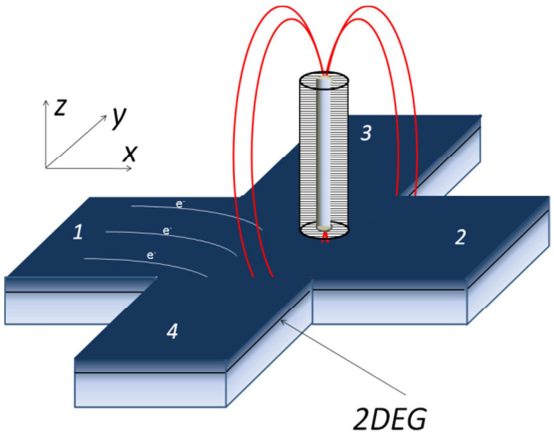

Figure 3.3: *Sketch of iron nanowire inside carbon nanotube placed near the center of the 2DEG micro Hall device. Red lines represent the lines of the stray field of the iron nanowire penetrating the active area of the sensor. Current I is injected between terminals 1 - 2 while Hall voltage is measured between terminals 3 - 4. White lines represent the hypothetical trajectories of electrons in the channel carrying the current I and they are deflected by z component of the stray magnetic field.*

There are several ways to include the external magnetic field in the system. The most common methods are: a) application of the external magnetic field in the plane of the device then the background signal coming from an external magnetic field has linear character and can be subtracted from the raw data (see subchapter 6.1.1.) or b) by using the gradientometry technique where the field is applied perpendicularly to the device surface, the device can be tilted and the background signal is subtracted using the reference Hall cross [62].

The way in which the 2DEG inside the active area of the device interacts with inhomogeneous stray fields (Fig. 3.4) to generate the Hall voltage was concerned by several different groups [63,64]. It has been shown that in the ballistic transport regime (subchapter 3.2.3) usually T < 100 K for GaAs/AlGaAs heterostructures with channel

width 800 nm and for tiny inhomogeneous magnetic fields, the Hall voltage is completely determined by the average z – component of the stray field in the cross region. In addition, the Hall voltage is independent of the detailed distribution of the magnetic field. Thus the Hall voltage measured by the device exposed to the small and nonuniform magnetic field can be written as:

$$U_H = \alpha \frac{I < B_z >}{ne} \tag{3.1}$$

where I is the current, n is the 2D electron concentration and e is the electron charge ($e \approx 1.6 \cdot 10^{-19}$ C). $<B_z>$ represents the already mentioned, average z component of the stray field in the active area of the device, α is the geometry dependent coefficient, however, for small radius of the corners of the Hall cross section $\alpha \approx 1$ [65]. The influence of the geometry of the active area on the Hall signal in the ballistic transport regime will be discussed further in subchapter 3.2.4.

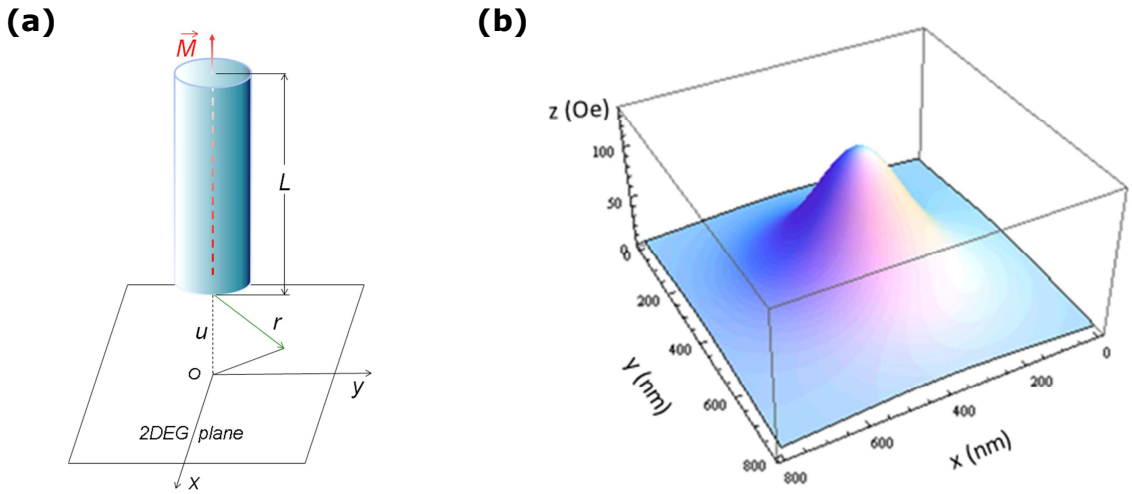

Figure 3.4: *(a) Coordinate system of the ferromagnetic nanowire placed on the active area of the micro Hall device [66], (b) theoretical distribution of the z component of the stray field inside the active area (800·800 nm^2) calculated for iron nanowire with diameter d = 18 nm and length l = 10 μm, with the distance to the 2DEG plane u = 200 nm.*

The z component of the stray field of the nanowire placed inside the active area (Fig. 3.4) can be expressed by the formula [66]:

$$B_z = \frac{m}{L}\left(\frac{u}{\left(\rho^2 + u^2\right)^{3/2}} - \frac{L+u}{\left(\rho^2 + (L+u)^2\right)^{3/2}} \right) \tag{3.2}$$

where m = M·V, M is magnetization of the nanowire, V is its volume, L is the length of the nanowire, u is the distance between the end of the nanowire and 2DEG plane and $\rho = ((x-x_0)^2+(y-y_0)^2)^{1/2}$ (Fig. 3.4), where x_0 and y_0 are particle coordinates. The average z component of the stray field inside the active area can be obtained by integration the above equation over the cross section of the device. The theoretical distribution of the z component of the stray field calculated by integrating equation 3.2 with step 10 nm for an iron nanowire with dimensions l = 10 µm and d = 18 nm, u = 200 nm, placed in the center of the Hall cross is shown in figure 3.4b.

Now we will discuss the influence of the size of the active area of the micro Hall device on its magnetic moment resolution. The field resolution of the device is defined as the minimum magnetic field which can be detected by the Hall sensor.
Thus we can write:

$$B_{\min} = \frac{V_N}{R_H \cdot I_{\max}} \tag{3.3}$$

Where V_N represents the noise level in the Hall voltage measurement for the maximum applied current I_{max}. For the 2DEG Hall devices with active area in submicron scale and operating with frequencies of the order of kHz the maximum injected current is limited by Joule heating in the device $(j_{max})^2 \cdot \rho$ = const where $\rho = (\mu ne)^{-1}$ is the resistivity of the device. Then $j_{max} = I_{max}/d$ where d is the channel width of the device. Thus we can write $I_{max} \sim d \cdot (\mu ne)^{1/2}$ and by substituting it into equation 3.3 we receive:

$$B_{\min} = \frac{V_N}{R_H \cdot I_{\max}} \sim \frac{1}{d \cdot \sqrt{\mu}} \tag{3.4}$$

This provides that the field sensitivity $(B_{min})^{-1}$ is proportional to the width of the device and can be increased by widening the channels. Moreover equation 3.4 clearly demonstrates the correlation between the mobility of carriers and the field sensitivity. This makes the 2DEG heterostructures as for example GaAs/AlGaAs with high electron mobility desirable materials for low magnetic field detection.

The equation 3.4 demonstrates that B_{min} is lower for larger size Hall cross. Using the Hall crosses with larger active areas for detecting nanoparticles with small magnetic moments is not a solution. This is because the inhomogeneous magnetic field created by the magnetic particle will be spread in relatively small area in comparison to the size of the sensing area of the device and thus generated Hall voltage will be small.

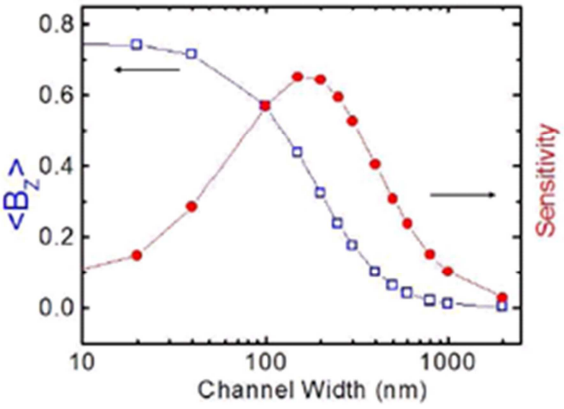

Figure 3.5: *Sensitivity dependence (red squares) of the micro Hall device as a function of channel width for a ferromagnetic cylindrical nanoparticle with diameter and high 100 nm. Distance between the 2DEG sensing plane and the end of nanoparticle 100nm. The best performance is achieved for channel w = 150 – 200 nm* [66].

Instead of using magnetic field resolution parameter to characterize device more suitable is to use magnetic moment resolution while describing the performance of the device for detecting nanosize particles. Thus the coupling coefficient β must be introduced which essentially describes the capability of the device to convert magnetic moment m into the average magnetic stray field $<B_z>$ inside the active area:

$$\beta \equiv \frac{<B_z>}{m} \tag{3.5}$$

In general, β depends on many factors i.e. shape of the device, position of the nanomagnet inside the active area, distance between the nanomagnet and 2DEG plain, magnetization of the nanomagnet etc.

The magnetic movement sensitivity of a Hall device in the ballistic regime can expressed:

$$m_{\min}^{-1} = \beta \cdot B_{\min}^{-1} = \frac{<B_z>}{m} \cdot B_{\min}^{-1} \quad . \tag{3.6}$$

where B_{min}^{-1} is the field sensitivity of the Hall sensor (see eq. 3.4) [66].

As found by Li [66], the dependence of the magnetic moment sensitivity m_{min}^{-1} as a function of the channel width w is shown in figure 3.5. The best sensitivity is obtained for the channel width 150 – 200 nm. However as it will be discussed in next subchapters in this range of the channel width mesoscopic effects (quenching of the Hall resistance and negative Hall effect) which have an influence on the Hall signal play a role. Thus to get rid of those effects it is needed to enlarge the channel width at least to the size of w = 800 nm which costs the sensitivity of the device.

3.2.3. GaAs/AlGaAs 2DEG heterostructure

For preparation of the micro Hall devices we used an n-doped GaAs/AlGaAs heterostructure[1] containing a 2DEG. In the following we will focus on the elementary properties of the heterostructure and the heterointerface at which the 2DEG forms. Because of the basic properties i.e. very low degree of lattice mismatch between the two materials and sufficient band-gap discontinuity, the GaAs/AlGaAs system heterostructure is an optimal material for creation of a 2DEG. In order to obtain a very sharp, on the atomic scale, interface between the AlGaAs and GaAs layers, molecular beam epitaxy (MBE) technique is employed. The small difference in the GaAs and AlAs lattice constants, which at room temperature equal 0.565325 nm and 0.56605 nm [67], respectively allows several microns of high aluminum containing AlGaAs to be grown on top of GaAs without introducing significant strains. The large bandgap discontinuity between the two materials provides electric carrier confinement. The band gap varies as $(1.424 + 1.594x + x\,(1 - x)\,(0.127 - 1.310x))$ eV [68] over the range $0 < x < 0.45$ where x is the Aluminum molar fraction. At higher x values, the AlGaAs bandgap becomes indirect. The most commonly used aluminum molar fraction for 2DEG heterostructures is $x = 0.33$ with a direct bandgap of 1.826 eV, resulting in good confinement for electrons at the interface.

Typically as n-type dopant for GaAs/AlGaAs, silicon is used, which tends to occupy the group III site during the growth process for (100) GaAs substrates under arsenic-rich growth conditions. The donor states are formed near the conducting band and provide electrons to the band. When doping $Al_xGa_{1-x}As$, with $x > 0.2$, some meta-stable deep level defects associated with silicon incorporation occur.

[1] The heterostructure was MBE grown by Dr. Paola Atkinson, Institute for Integrative Nanosciences, IFW Dresden.

These so called D-X centers have significant influence on the photoresponse of the 2DEG at low temperatures and electrical noise at temperatures T > 100 K [69]. A schematic picture of a typical n - doped GaAs/AlGaAs heterostructure is shown in figure 3.6. It starts with bulk GaAs substrate, on which superlattice is grown. The role of the former is to prevent the diffusion of impurities from the substrate. Then a buffer layer ≈ 1 μm of pure GaAs is grown.

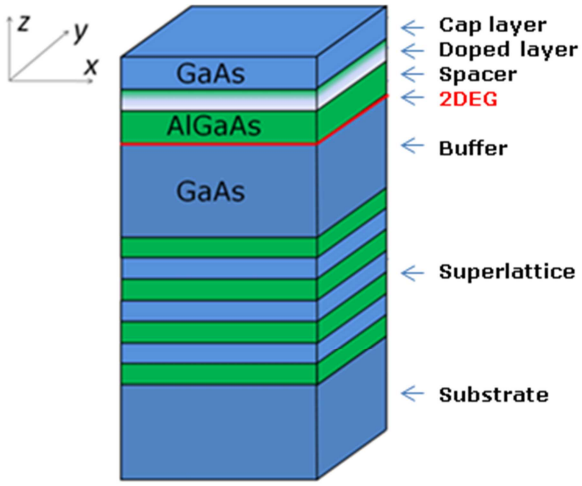

Figure 3.6: *Schematic picture of the GaAs/AlGaAs multilayer heterostructure in which a 2DEG is formed.*

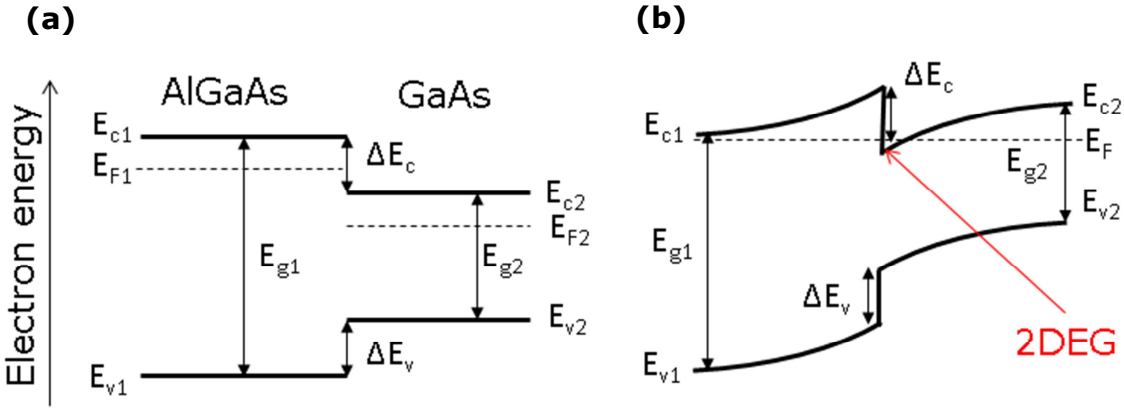

Figure 3.7: *Band diagram of the GaAs/AlGaAs interface. Left part corresponds to the n-doped AlGaAs layer, while the right part to the intrinsic GaAs. (a) The band diagram at t = 0 s before the charge transfer, E_c, E_F, E_V represent the bottom of conducting bands, Fermi energies and the top of the valence bands, respectively, (b) the band structure after the redistribution of charges Both bands in the n-doped and intrinsic part are bent. The triangular potential well below the Fermi level is formed in which electrons are confined and form thin layer [70].*

To achieve high mobility of electrons in the 2DEG (at low temperature coulomb scattering due to ionized impurities is the dominant scattering process) an undoped

AlGaAs spacer layer (thickness of few tens of nanometers) is grown on the buffer in order to separate the n -doped layer from the 2DEG. The n-doped AlGaAs layer of thickness of few tens of nanometers is grown on the spacer. At the end the structure is covered with a protective GaAs cap layer of thickness ≈ 10 nm.

The 2DEG forms at the interface between buffer and spacer layers and the schematic picture of band diagram and formation of 2DEG at the GaAs/AlGaAs interface is shown in figure 3.7. The band diagram of the interface at t = 0 s is shown in figure 3.7a. Energies E_c, E_v and E_F correspond to bottom of the conducting bands, top of the valence bands and Fermi levels in both semiconductors, respectively. The chemical potentials in both parts are in the different levels i.e. the level in the n - doped part is higher than that in the intrinsic part. This is not the equilibrium state thus in order to equalize both chemical potentials the redistribution of the charges takes place. The electrons from n - doped part drift into the intrinsic part to lower the system energy. The redistribution process results in band bending and the formation of a triangular potential well located below the Fermi level (see Fig. 3.7b). Electrons are confined in the triangular potential well and form 2DEG. Electrons in the 2DEG are characterized by very high mobility at low temperatures exceeding 10^6 cm^2/Vs [71], much higher than in bulk semiconductors. As mentioned above the increased mobility of the electrons is achieved by the separation of the doping layer from the channel by the spacer layer. This increase of the mobility is significant at low temperatures (redundant scattering in phonons) where coulomb scattering due to ionized impurities is the dominant scattering process.

Due to the high mobility of electrons in the 2DEG the heterostructure is often called a high electron mobility transistor (HEMT). The mobility and carrier concentration in a 2DEG can be modified and controlled by the application of an electric potential either at the front or at the back of the structure.

A sketch of a triangular potential well is shown in figure 3.8. The energy barrier at z = 0 is approximated by an infinite barrier while for z > 0 the potential is approximated by a linear potential V(z) = eFz, where F is the electric field and z represents the growth direction of the heterostructure. The consequence of the additional potential V(z) is that the electronic wave function satisfies the conditions of the narrow box potential (confinement potential) in the z direction, while wave functions perpendicular to the x - y plane should have a Bloch character. Electrons are free to move only in x-y plane. The energy spectrum of electrons in the potential well is given:

$$E_n(k) = \varepsilon_n + \frac{\hbar^2(k_x^2 + k_y^2)}{2m^*} \tag{3.7}$$

where, n=1,2,3,….

The lowest energy levels and the associated wave functions for the triangular potential well are show in figure 3.8.

Usually, for GaAs/AlGaAs heterostructures the 2DEG confinement is strong while the carrier density is low so that only the lowest subband is occupied (n = 1). Two dimensional electron gases can then be described by a parabolic dispersion relation with the ground state energy E_1.

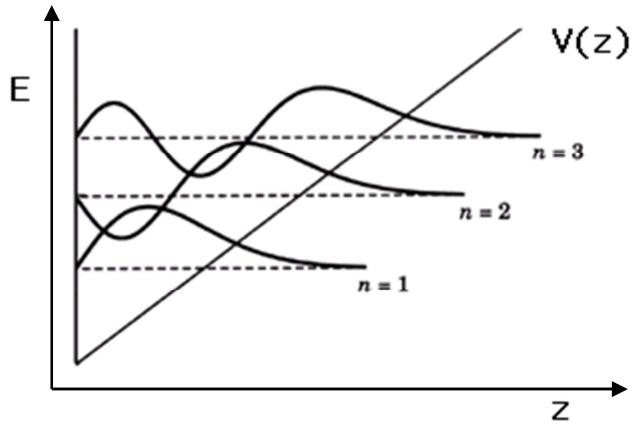

Figure 3.8: *Triangular potential well V(z), with first three energy levels and wave functions. It is good approximation of the well formed at the heterointerface [72].*

At low temperatures the conductance is determined mostly by the electrons having energies close to the Fermi energy. The electrons which take part in the transport in 2DEG can be described by the quantities:

- wavelength

$$\lambda_F = 2\pi / k_F = \sqrt{2\pi / n_s} \tag{3.8}$$

For the concentration of carriers $n_s \approx 10^{11}$ cm^{-2} typical for GaAs/AlGaAs heterostructures the Fermi wavelength is about 80 nm.

- wavenumber

$$k_F = \frac{2\pi}{\lambda_F} = \sqrt{2\pi \cdot n_s} \tag{3.9}$$

- velocity

$$v_F = \frac{\hbar k_F}{m^*} = \frac{\hbar}{m^*}\sqrt{2\pi \cdot n_s} \tag{3.10}$$

with effective mass $m^* = 0.067 \cdot m_e$ in case of GaAs/AlGaAs heterostructures.

3.2.4. Drude theory of transport

The Drude approach treats all electrons as independent particles moving through the crystal where they are randomly scattered with probability $1/\tau$. After the application of an external electric field E electrons are accelerated in the field direction and reach the so called drift velocity v_d:

$$v_d = \frac{eE\tau}{m^*} \tag{3.11}$$

where τ is the mean time between the collisions and m^* is the effective mass of electrons. The electron mobility is given:

$$\mu = \frac{|v_d|}{|E|} = \frac{e\tau}{m^*} \tag{3.12}$$

and the conductivity:

$$\sigma = \frac{ne^2\tau}{m^*} \tag{3.13}$$

where n is the electron concentration.
In the presence of an external magnetic field B the Lorentz force deflects the electric carriers:

$$\vec{F}_L = -e(\vec{E} + \vec{v} \times \vec{B}) \tag{3.14}$$

The force causes the appearance of the charge at the side of channel carrying the electric current thus additional transversal electric field appears. Consider the sample placed in the electric field E_x and exposed to the perpendicular magnetic field B = (0,0,B).
The current cannot flow out the sample in y direction, thus $\langle v_y \rangle = 0$. This is possible only if the transversal electric field appears:

$$E_y = -\frac{eB\tau}{m^*} E_x \tag{3.15}$$

Hall coefficient is defined:

$$R_H = \frac{E_y}{j_x B} \tag{3.16}$$

To calculate the Hall coefficient the change of the momentum of electrons upon acting of the magnetic and electric field must be considered:

$$\frac{d\vec{p}}{dt} = -e(\vec{E} + \frac{\vec{p}}{m^*} \times \vec{B}) - \frac{\vec{p}}{\tau} \tag{3.17}$$

In the steady state the current is independent on time, thus we can write:

$$\sigma_0 E_x = \omega_c \cdot \tau \cdot j_y + j_x \tag{3.18}$$

$$\sigma_0 E_y = -\omega_c \cdot \tau \cdot j_x + j_y \tag{3.19}$$

where σ_0 is the electric conductivity given by the formula 3.13, j = - nev is the current density and ω_c represents the cyclotron frequency.

$$\omega_c = \frac{eB}{m^*} \tag{3.20}$$

The cyclotron frequency ω_c is the frequency of the orbital movement of the electrons in the magnetic field with assumption that the whole orbit is closed before electrons are scattered. The cyclotron radius can be then expressed:

$$R_c = \frac{\hbar k_F}{eB} \tag{3.21}$$

As already mentioned in the equilibrium conditions the average current j_y is zero, thus we can now write the Hall coefficient:

$$R_H = \frac{1}{ne} \tag{3.22}$$

The longitudinal conductance is independent of the magnetic field:

$$j_x = \sigma_0 \cdot E_x \tag{3.23}$$

In this consideration we must assume that the mobility is dependent on the relaxation time averaged over the all electrons, thus:

$$\mu = \frac{e\langle\tau\rangle}{m^*} \tag{3.24}$$

This provides the additional factor to the Hall coefficient:

$$R_H = \frac{\langle\tau^2\rangle}{\langle\tau\rangle^2}\frac{1}{ne} \tag{3.25}$$

This additional term is known as the Hall factor. It is assumed to equal one. However in the rare cases in 2DEG structures it has been shown that the Hall factor can be higher than one. In the micro Hall measurements we assume that the Hall factor equals one.

3.2.5. Transport regimes

Depending on the characteristic quantities i.e. Fermi wavelength and phase coherence length, the transport through the sample can be divided into three different regimes (ballistic, quasi ballistic and diffusive). As long as both the Fermi wavelength and the phase coherence length are much smaller than the size of the sample, the classification of type of the transport regime is made by direct comparison between sample dimensions and the mean free path of electrons. In the case, when the mean free

path of electrons is much shorter than the width W and length L of the sample, the transport is diffusive. The diffusive transport of charge carriers can be then described on the basis of the Drude model discussed above and the conductance obeys the Ohms law:

$$G = \frac{\sigma W}{L} \tag{3.26}$$

where, σ is conductivity, W and L are the width and length of the channel for the 2DEG, respectively.

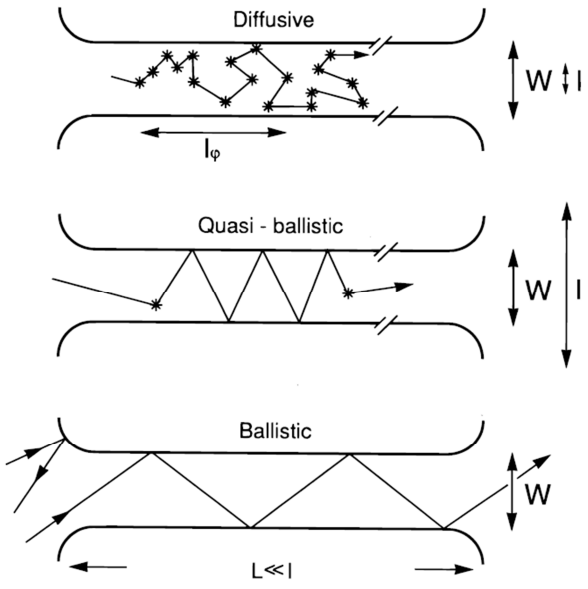

Figure 3.9: *Electron trajectories in the wire under diffusive (mean free path l_e is significantly shorter than the width W and the length L of the channel: l_e << W, L), quasi-ballistic (L < l_e <W) and ballistic (l_e >> W, L) transport regimes [73].*

In the ballistic transport regime, the channel dimensions are much smaller than the mean free path. The simple expression of the conductance (eq. 3.26) is not valid anymore, since in case of a conductor with short conducting channel L → 0, one would expect that the conductance increases to infinity G → ∞, which is not the case. In this regime the scattering at the impurities and defects is negligible and only the conductance plays a role instead of the conductivity. In the ballistic transport regime, the Landauer formula expresses the conductance in terms of transmission probabilities:

$$G = \left(\frac{e^2}{h}\right) T \tag{3.27}$$

where T is the transmission probability, h is the Planck constant and e is the electron charge. The resistance of the sample is mainly due to the backscattering of electrons at transition regions of the channel. One can further distinguish an intermediate quasi-ballistic regime, characterized by $W < l_e < L$. Characteristic for this is that the scattering of charge carriers on impurities or phonons, and at the edges of the sample are quite similar.

3.2.6. Mesoscopic effects

Ballistic electron transport causes multiple anomalies in the Hall signal, which are the result of the deviations from the right angled Hall cross. The finite radius of curvature of the corners, always present, due to the processing of the device, results in strong deviations of the linear Hall voltage curve. This can be explained by curved trajectories of electrons in a classical billiard [74] which allows the change in the electron trajectories through mirror reflection at the probe edges (Fig. 3.11).

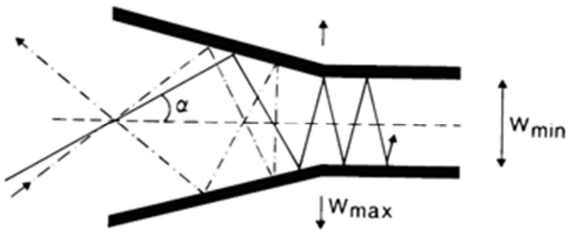

Figure 3.10: *Sketch presenting the collimation effect. The channel width changes from W_{min} to W_{max}. Electrons approaching at angle larger than α are reflected what is presented by dash-dotted lines [75].*

At very small magnetic fields collimation (Fig. 3.10-3.11a) and scrambling (Fig. 3.11b) are responsible for anomalies in the measured Hall signal. The former effect caused by the geometry appears in the gradual decrease of width of the channels leading to active area. Electrons can only reach the voltage sensors below a certain angle α due to the geometry of the Hall cross (Fig. 3.10-3.11a). If the angle is above this threshold electrons undergo multiple reflections in the active area resolving an equal probability to reach both voltage sensors (Fig 3.11b). Through this collimation of electrons the Hall effect can be suppressed at small magnetic fields as shown by the dashed line in figure 3.11d. This is so called quenching of the Hall resistance with a characteristic plateau, which was shown by *Roukes et al.* [76] in quantum wires where transport happens in the ballistic and diffusive regime depending on the channel width. Such a suppression of the Hall voltage is not observed for Hall cross with right-angled corners [77,78].

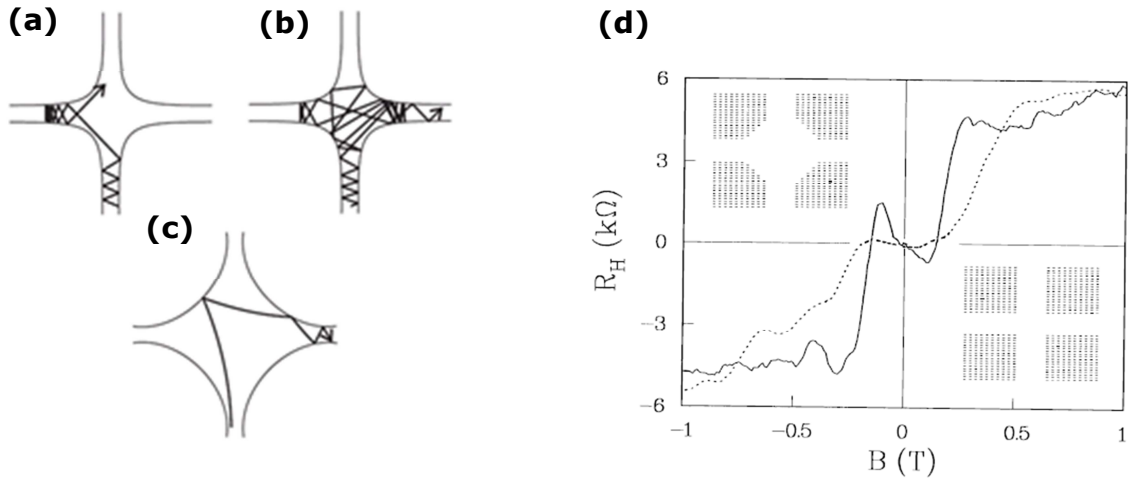

Figure 3.11: *Classical trajectories of the electrons in the ballistic regime demonstrate the influence of the active area geometries. (a) Collimation, (b) scrambling, (c) rebound, (c) shows the experimental effect of varying the radius of curvature of corners on the Hall resistance. The dashed line shows a quenching of the Hall effect at low magnetic field, and represents the inset in the lower right, with small corner radii. The solid line represents the negative Hall effect at small fields, and represents the inset in the upper left, with large corner radii [79, 80].*

A device with strongly rounded corners is presented in figure 3.11c. An electron which is reflected from the side of the channel might enter the opposite channel of the device with large probability. This mechanism is called the “rebound” mechanism and is responsible for a negative Hall effect. At low magnetic fields it changes the sign of the Hall resistance as shown in the figure 3.11d by the solid line.

Thus for the proper fabrication of the active area of the micro Hall sensor, appropriate selection of the channel width and minimization of the corners radii are mandatory conditions in order to minimize the influence of the above mentioned effects on the magnetic investigations of nansoscale magnets. The exact preparation technique of the device will be described in the following chapter. In the Hall voltage measurements performed on micro Hall devices prepared in this work with channels width 800 nm we did not observe any influence of these mesoscopic effects on the measured Hall signal.

4. Experimental details of the micro Hall setup

4.1. Scanning electron microscope

SEM is a tool for fast visualizing nanometer sized objects, and it provides the information on surface topography and chemical composition. In combination with special electronic it can be used for patterning nanometer scale structures with electron beam lithography. Electron microscopes can achieve a maximum magnification of 500 000. In this work we used SEM FEI Nova NanoSEM 200. A schematic picture of the electron microscope is shown in figure 4.1a and the picture of the inside of SEM chamber made with the CCD camera is presented in figure 4.1b.

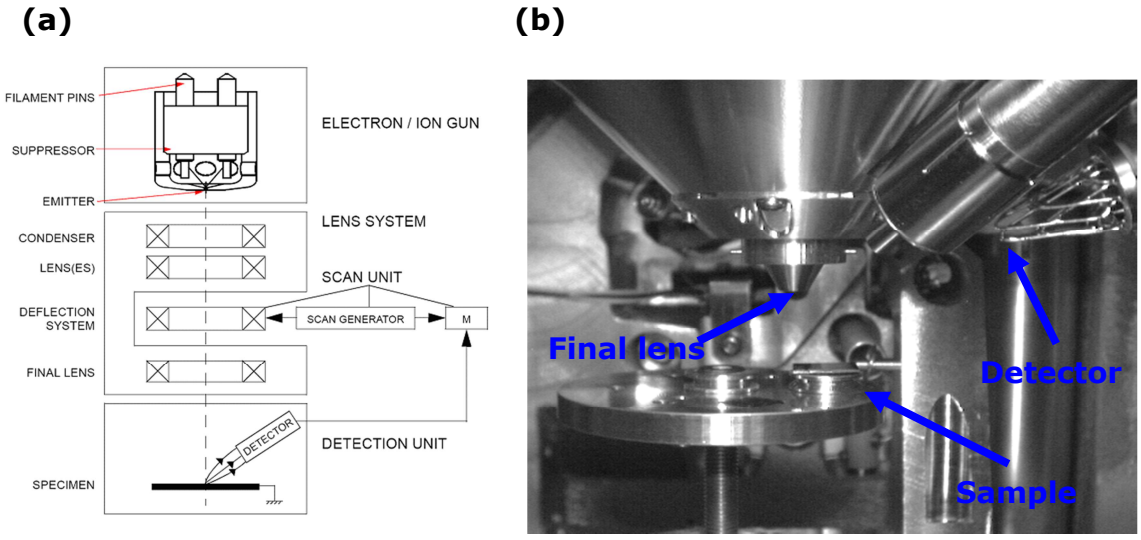

Figure 4.1: *(a) Schematic overview of the scanning electron microscope [81], (b) chamber of the microscope.*

The microscope consists of four main modules:

- The source of free electrons – electrons are thermionically emitted from field emission gun cathode with low angular spread and selectable energies. The emission current can be varied between pA to nA.

- Lens system – after the electron beam is created it passes the lens system which contains several electromagnetic and electrostatic lenses. In the condenser lenses the beam is focused to spot about 1 nm. Then the beam passes the x,y deflection system which provides the scanning of the rectangular area,

- Scan unit – connected to the deflection system moves the electron beam in a raster pattern at the sample area,

- Detection unit – The detection system, equipped with respective detectors, picks up back scattered electrons, secondary electrons and x-rays and converts it into an amplified electrical signal.

Basically imaging of an object is based on scanning its surface with a high energy electron beam (2 to 30 keV) in a raster pattern. This creates secondary and backscattered electrons, x-ray irradiation, which are collected by respective detectors, converted to a voltage and amplified. Secondary electrons are low energy electrons with energies below 50 eV. Incident electrons kick out electrons from the orbits (K shells) around the nucleus. Secondary electrons can only escape from the layer near the surface, hence the area contributing to the signal is nearly the size of the electron beam. Thus they provide the highest resolution images. Secondary electrons provide topographic information and to a certain extend a compositional contrast.

Backscattered electrons are high energy electrons. They enter the sample and approach the nucleus of an atom close enough to be scattered back (Coulomb scattering) and exit from the sample surface. Images crated with backscattered electrons are with lower resolution in comparison to images created with secondary electrons due to the deeper penetration of the sample, thus the area which contributes to the signal is larger than the size of the electron beam. Backscattered electrons provide a large compositional contrast i.e. the higher the atomic mass of chemical elements the brighter the contrast.

Characteristic x – rays provide information about the chemical composition. When an incident electron hits and kicks out electrons from an inner shell then electrons from outer shells fill the vacancy. Thus electrons are jumping from higher to lower energy states i.e. from shells M to L and L to K and due to this they irradiate characteristic x-rays to conserve the energy. The chemical elements are identified by measurements of the energy of those x-rays [82].

4.2. Electron beam lithography

For patterning micro Hall devices onto the sample surface, we used the combined system FEI Nova NanoSEM 200 and attached patterning system (Nanonic GmbH) with beam blanker booster for high blanking rates. A schematic picture of the system is shown in the figure 4.2. The 16 bit patterning system provides a high precision in guiding the electron beam down to nanometer scale.

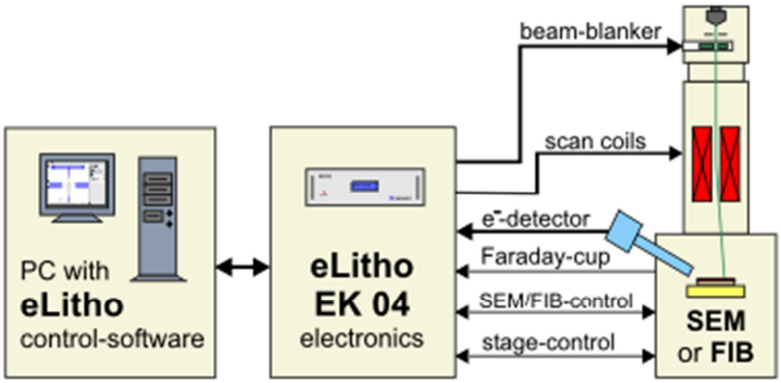

Figure 4.2: *The schematic interactions of the lithography system with scanning electron microscope or focused ion beam. With aid of the edraw software the layout of the desired structure is created and the exposure process controlled with Tax software (elitho). In the actual lithography process the external electronics (middle) takes the control on the stage position and the operation of the electron beam. The structural data is transferred to the analog voltage signals. The beam is swept in the raster mode via the scan coils which deflect it and beam blanker is turn on and off in the right time. The Faraday cup is used for the measurement of the beam current before the lithography process. This helps to define the time of the exposure of individual pixel [83].*

Electron beam lithography (EBL) is a practical tool for patterning very small structures on organic resist, the Poly(methyl methacrylate) (PMMA) covering the surface of the sample. The desired shape of the structure is achieved by selective irradiation of the resist with electron beam. High energetic electrons (~ keV) are cutting the chains between the monomers in PMMA. The exposed regions can be then dissolved in the developer solution and the pattern can be transferred to substrate material for example by wet chemical etching. Now we will shortly describe the interaction of the electron beam with the substrate and resist while later we will focus on the entire procedure of patterning the devices and preparation of 2DEG contacts. The electron beam enters the resist and

penetrates the substrate (Fig. 4.3). The penetration depth mostly depends on the acceleration voltage V_A and usually is around few µm. An initial spot size of the electron beam (≈ 1 nm) broadens to over 10 nm, upon entering the resist what reduces the resolution of the process. Electrons from the primary beam are scattered in several ways in the PMMA and substrate. The energy of secondary electrons is too low (50 eV) to have any significant effect on the resist while fast back scattered electrons (keV) cut the chains of polymer in the exposed parts of the resist. The rest of the beam energy is transferred into x - ray irradiation and Auger electrons.

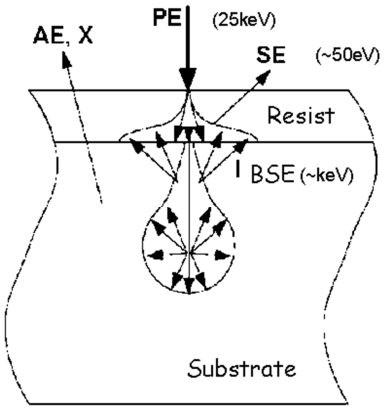

Figure. 4.3: *Primary electron beam travels through the resist and penetrates the substrate in a few microns. As the result of the scattering of primary electrons in the substrate slow secondary electrons appear with energies ~ 50 eV and very fast backscattered electrons with energies ~ 1 keV which are responsible for scissoring the chains in PMMA. Part of kinetic energy is transferred to x - rays and Auger electrons which do not contribute to the process of electron lithography [84].*

The backscattered electrons are reflected in different directions what influence doses of neighboring structures and cannot be neglected. These proximity effects are in the range of 5 µm and depend on several factors i.e. thickness of the resist, distance between structures, material of the substrate, acceleration voltage etc. Therefore while designing a new structures this is always necessarily to perform additional test to adjust the lithographic parameters (dose factor, and dose value for individual pixel).

We designed the eight terminal Hall device shown in figure 4.4a which can be used in both: the gradientometry setup and in Hall measurements with external magnetic field applied in plane of the device. The first important step in the preparation of micro Hall devices is to design of the proper layout with edraw software. The geometry of the Hall

cross can influence the device performance, thus it is necessary to provide the shape of the Hall device with right angle corners.

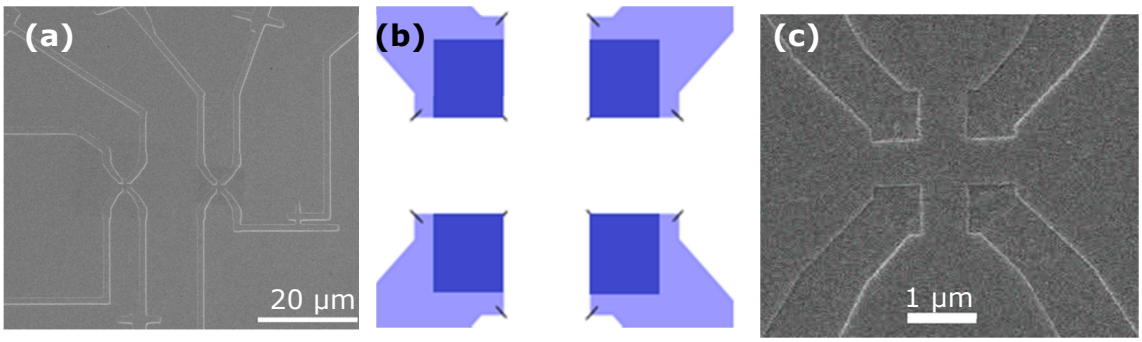

Figure 4.4: *(a) SEM picture of the eight channel Hall device used in this work,(b)The edraw layout for the individual Hall cross. The dark blue areas correspond to the dose factor 1, light blue areas to 1.2, while the lines to dose 2000 pC/cm, (c) SEM picture of the properly shaped Hall cross after the entire preparation procedure.*

Because the channel width of the micro Hall devices used in this work was selected to 800 nm the proximity effects during the exposure in the electron beam play a role. The exposing parts are very close therefore during the exposure procedure both influence each other. This might result in rounded corners with a radius of 300 nm after the entire process. To avoid this, additional lines (with dose 2000 pC/cm) in the corners are inserted in order to locally increase dose value (Fig. 4.4b). A proper shape of the Hall cross with minimized radius of the corners is shown in figure 4.4c.

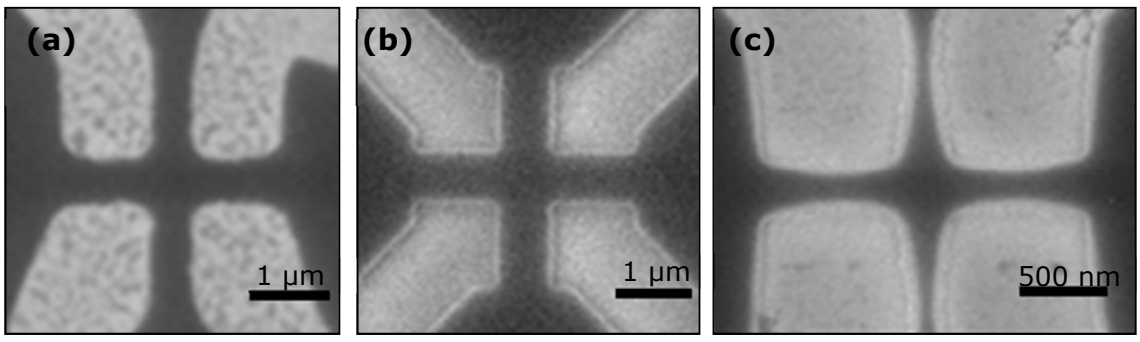

Figure 4.5: *SEM picture shows influence of doses on the shape of microstructure. The dark areas correspond to the resist while light to the uncovered GaAs surface. (a) Underexposed structure with doses value 130 µC/cm^2, (b) right dose number 190 µC/cm^2, (c) overexposed structure 250 µC/cm^2.*

Another important factor which has to be taken into account is to determine the proper doses (Fig. 4.5) (the number of electrons which hit the surface unit ($\mu C/cm^2$)) for a given structure. The correct dose is most important for the smallest structures. Determination of proper dose can be done by performing an additional test before exposing the entire layout. One can use the pure GaAs for testing and expose it with a series of the smallest structures with varying dose numbers. If the doses are too low then the final structure is underexposed (Fig. 4.5a). This causes the residual polymer at the exposed parts and underexposure of corners which becomes rounded. If the dose is selected too high than the structure becomes overexposed and additional doses increase the proximity effects (Fig. 4.5c). Only the selection of proper dose number results in the correctly exposed areas and Hall cross with sharp corners and straight paths (Fig. 4.5b). We discussed the influence of the layout design and doses values on the shape of the device right now we will shortly discuss the preparation of Ohmic contacts and patterning the devices onto the heterostructure surface.

4.3. Preparation of the substrate for EBL patterning

For the micro Hall devices the size of the chips was chosen to be 3.5×5 mm^2 due to the a design of the chip carrier. At first the entire wafer was covered by spin coating with thick layer (≈ 1 μm) of polymer in order to protect the surface from a dust. The sample was then cut in the desired dimensions by scratching lines along the crystal axes with the aid of diamond scriber. Then the chip was placed in the Trichloroethylene (TCE) solvent bath for three minutes in order to dilute the polymer from the surface.

We performed cleaning of the sample towards preparation the surface for further processing i.e. spin coating and electron beam lithography. The sample was washed three times with acetone. To tune up the cleaning procedure the first beaker with acetone was heat up to temperature 70 ^oC. While taking the chip from one beaker to another the surface of the sample was rinsed with fresh acetone. Then the similar procedure was performed with cleaning in the isopropanol (IPA). In the last beaker a very short about 20 s ultrasonification was applied. The sample was blown dry with high purity N_2 and at the end the chip was placed on a hot plate (150 ^oC) for 10 minutes to get rid of the residue water layer.

4.4. Preparation of Ohmic contacts

In this work we firstly prepared Ohmic contacts on the chips and in the next step the samples were realigned in the SEM and micro Hall devices were patterned according to the position of Ohmic contacts.

At first the 2DEG heterostructure was covered with electron susceptible resist via spin coating. For the first layer we used PMMA with an average molecular weight of 50 K, 9 %. We used a spin coater (Laurell) with maximum 6000 rpm spinning velocity. One spin coating run was divided into three steps. At first – start 500 rpm/5 s, second – pulling down drops of the polymer into the surface 2000 rpm/5 s and the last step – dispersing of the polymer on the surface 6000 rpm/30 s. After this procedure the polymer was homogeneously dispersed on the surface with layer thickness of ≈ 200 nm. To avoid any strains inside the polymer layer and to evaporate chlorobenzene one applies a baking on a hot (150 ^{o}C) plate for 10 min. A similar procedure was then performed to provide the second layer of PMMA on top (950 k, 1 %).

Using two layers of PMMA was necessary in order to get the so called undercut profile of the resist after the developing procedure. The 50 k resist on the bottom is approximately 15 % more susceptible to the electron beam than that (950 k) on top what provides the undercut profile, necessary for successful lift off process. Such prepared substrate is then ready for exposure in the electron beam. The adjustment of the electron optical system (mainly astigmatism) was performed by focusing at the edges of the sample. The alignment of the sample to the corners of the chip was performed carefully. That was necessary in order to avoid large relative shifts of the areas in the second exposure for preparation of Hall devices.

The working distance between the final condenser lens and sample surface was set at 13 mm. The acceleration voltage was set to 25 kV. Each of the sixteen contact pads on one chip was 300 × 500 μm^2 large thus in order to shorten the time of the exposure session the current beam, measured with aid of Faraday cup was set to maximum (spot size 5, I ≈ 2600 pA). After the irradiation in the electron beam the sample was developed in the solution of 1:3 MIBK: IPA for 2.5 minutes and put in the IPA for 1 min to stop the further development and dry – blown with N_2. The irradiated areas are now uncovered. The metallization was done with aid of (Univex 450, Leybold) and AuGe 200nm and Ni 40nm thick layers were deposited in on top of the sample surface. The lift off procedure was

performed by immersing the sample in warm acetone (70 ^{o}C) for 20 minutes, and then washing it in the IPA and dry blown with N_2.

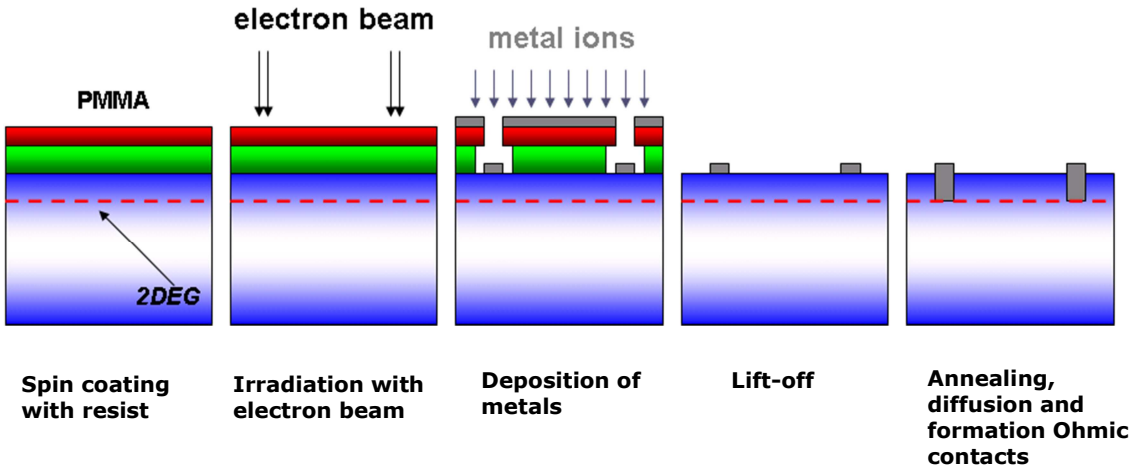

Figure 4.6: *Sketch of the contacts preparation. GaAs is spin coated with double layer of electron resist (50 K, 9 % bottom layer and 950 K , 1 % top layer), the desired parts of surface are irradiated with electron beam, development procedure removes the exposed resist layers, the entire surface is coated with the AuGe 200 nm and Ni 40 nm layer, lift-off process dissolves the PMMA and remove the metals layer from top of the polymer, annealing provides the alloying and diffusion of the alloy below the surface and formation 2DEG contacts.*

This lifts the metal layers from top of the PMMA and ends up with metal layers lying in the exposed areas. The annealing procedure was performed in an oven (AZ 450, MBE Komponenten GmbH) with set parameters 350 ^{o}C/120 s, 450 ^{o}C/50 s, 50 ^{o}C/s which initialized and provided alloying of metals and diffusion of the alloy below the surface. The temperatures and time of the alloying was chosen for the specific doping concentration and deepness of 2DEG below the surface[2].

4.5. Patterning the micro Hall devices onto heterostructure surface

For patterning the Hall devices on chip with Ohmic contacts, the substrate surface was again prepared as described in subchapter 4.3. The surface was spin coated with one layer of PMMA with average molecular weight (950 k, 4 %). The resist was drop onto the spinning substrate (2000 rpm) and spun for 30 s at spinning velocity 6000 rpm.

[2] Metal deposition, annealing and lift off were done by Mrs. Cornelia Linz from University of Regensburg.

This resulted in a thickness of the first layer of PMMA of around 150 nm. The substrate was baked for 10 min at 150 ^{o}C hot plate. Such prepared sample was loaded into SEM chamber for EBL patterning.

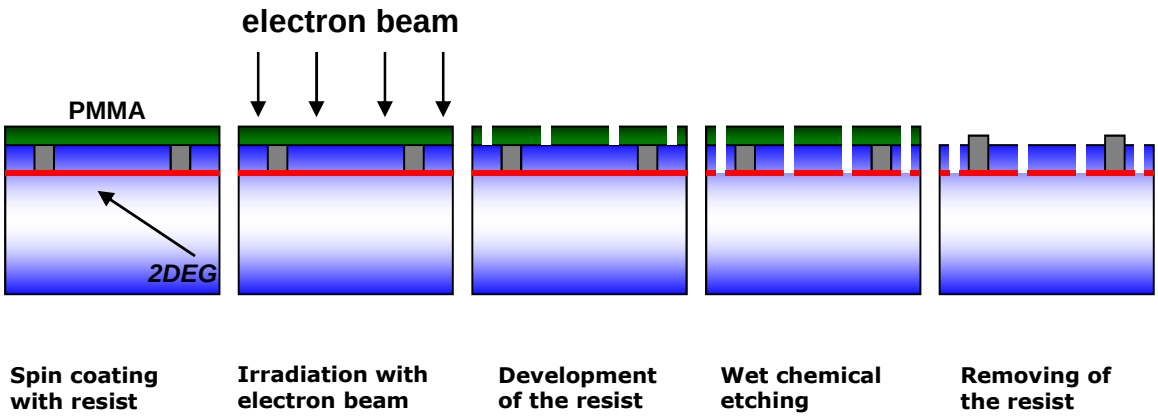

Figure 4.7: *Sketch of the patterning devices procedure. GaAs plane is spin coated with electron resist (PMMA), the desired parts of surface are irradiated with electron beam, development procedure rinses out the exposed resist, wet etching removes uncovered GaAs and post etching cleaning, strip off the residual resist.*

It was necessary to carefully readjust the sample to the corners in order to pattern the entire layout with correct position with respect to the contact pads. The EBL exposure session was split into two parts. At first the submicron Hall crosses and surrounding lines were exposed with the smallest beam current ≈ 20 pA. This helps to minimize the influence of proximity effects between closest neighboring structures. Then the current was changed to the higher values ≈ 2000 pA and the rest of the pattern was exposed. The time of developing was 2 min in 1:3 MIBK solution and 1 min in pure IPA.

To transfer the pattern into the GaAs surface we used a wet chemical etching method. As the etchant we used a solution of diluted sulfuric acid: H_2SO_4 : H_2O_2 : H_2O with a volume ratio 1:8:40 and further diluted with a deionized water with a volume ratio 1:16.

The fresh etchant must be tested. By performing the atomic force microscopy (AFM) scan on the test structure with known time of etching one determines the precise etching rate which is usually around 1 nm/s. This provides relatively high precision of etching (± 2 nm). To stop the formation of 2DEG below the surface it is necessary to remove at least n-doped layer. Therefore we chose 65 nm of etching. This relatively shallow etching depth was chosen in order to avoid overlapping of the etched depletion from two etched sides, what could make the smallest channels insulating. Wet chemical etching is

performed as bath of the sample in the beaker filled with the fresh etchant. After the desired time of etching the structure is put into the deionized water for 1 min to stop the further etching.

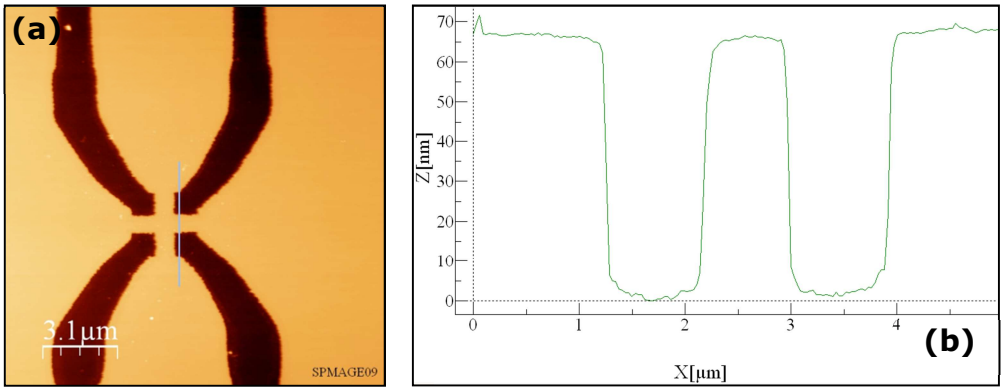

Figure 4.8: *(a) AFM topography image of the 0.8 × 0.8 µm² Hall cross prepared on GaAs/AlGaAs heterostructure, (b) the corresponding cross section of the device with etching depth of around 65 nm.*

The last procedure in shaping of the surface of the heterostructure is stripping off the polymer from the surface. This consisted of bath of the sample in acetone and isopropanol. Acetone dissolves PMMA while isopropanol cleans GaAs surface. After the bath the sample was dried with N_2. The AFM image and the cross section of the etched structure are shown in figure 4.8. The cross section of the device is nearly rectangular with etching depth ≈ 65 nm.

4.6. Synthesis and characterization of iron filled carbon nanotubes

The Fe nanowires encapsulated in the CNTs were prepared with the thermal chemical vapor deposition method[3]. For this purpose the two-zone furnace with separate sublimation and reactions zones is used. The schematic picture of the furnace is shown in figure 4.9. A silicon substrate covered with a thin (10 nm) aluminum layer and an additional iron catalyst layer (2 nm) on top, synthesized by sputter techniques or electron (e)-beam evaporation, was employed. The additional buffer layer of aluminum helps to

[3] The batch of Fe-filled CNTs used for micro-Hall magnetometry was prepared by Uhland Weissker, Institute for Solid State Research (IFF), IFW Dresden.

improve the nanotubes alignment and provides nanotubes with smaller distribution of diameters [85].

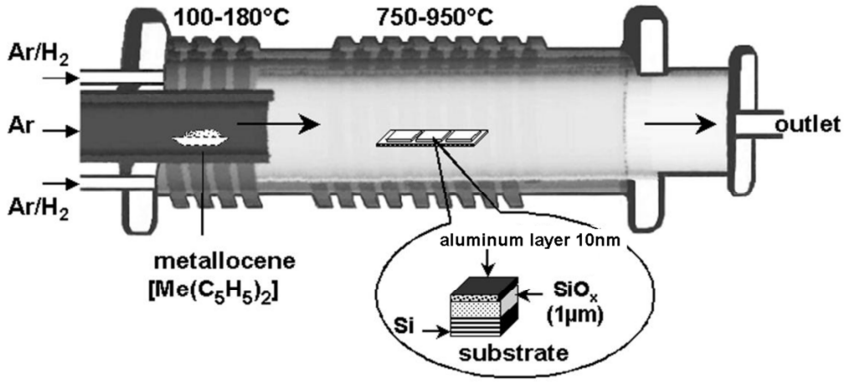

Figure 4.9: *Two-zone furnace for the pyrolysis of metallocenes, single source chemical vapor deposition (SSCVD) and the structure of substrates used (metal: Fe, Co, Ni) [86].*

For the Fe-filled CNT growth, the ferrocene which consist of both iron for the filling and carbon for the carbon shell formation is sublimated at T = 130 ^{o}C for 10 min. Ar gas flow of 150 sccm was employed to transport the sublimated ferrocene into the reaction zone (Fig. 4.9). In order to prevent condensation of the ferrocene in the reaction zone the substrate was heated up and kept at a constant temperature 300 ^{o}C. As soon as the sublimation is constant the temperature of the reaction zone is changed to 800 ^{o}C with a constant rate 0.6 K/s, and above 600 K the ferrocene starts decomposing. Carbon species take a reaction with the iron catalyst layer which induces the formation of carbon nanotubes on the substrate. Iron clusters resulting from the steam are incorporated into the nanotubes during their growth. The method described above provides nanotubes with a length of about 10 - 25 µm (Fig. 4.10a) and very high filling ratio. However, the CVD method used for synthesis is a dirty method. Very often many of the residual catalyst nanoparticles are attached to the nanotubes (Fig. 4.10b). These catalyst particles could affect the results of Hall magnetometry measurements. As it will be described in subchapter 4.7, micromanipulator allowsone to select nanotubes without external nanoparticles. Figure 4.10c shows the high magnification TEM image of an individual Fe-filled CNT. Carbon shells are clearly visible, while the dark contrast corresponds to the iron filling. With high resolution diffraction measurements, single crystalline α - iron is evidenced (Fig. 4.10d).

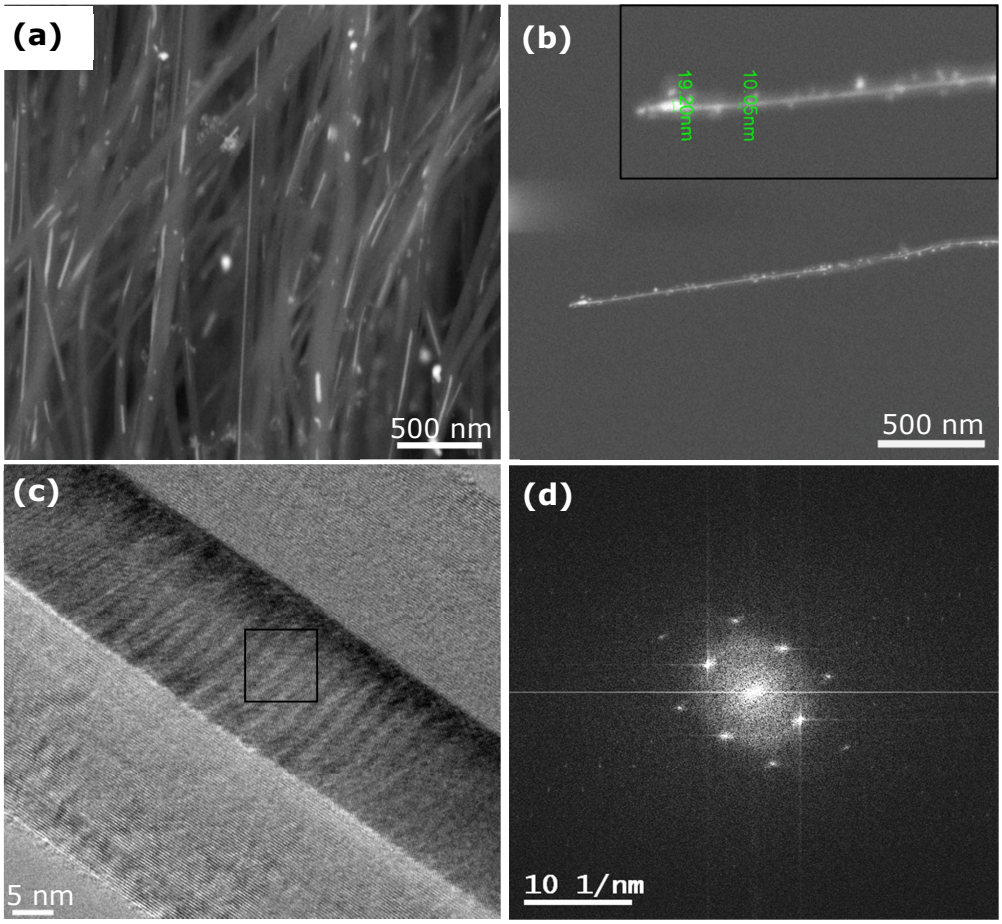

Figure 4.10: *(a) BSE image of Fe-filled CNTs grown on a silicon substrate, bright contrast represents iron filling, (b) individual Fe-filled CNT with surrounding residual catalyst particles, (c) TEM image of a Fe-filled CNT, carbon shells are clearly visible, the dark core is the iron filling, (d) high resolution diffraction measurement of the α phase iron filling. (TEM image and diffraction measurements were made by Dr. Thomas, IFW Dresden)*

4.7. Micromanipulation

In the following, we will discuss the influence of the position of the nanomagnet in the active area on the Hall signal and further micromanipulation technique used in the experiments. The strength of the Hall signal is strictly connected with the position of the nanomagnet on the active area of the device and distance between the nanowires end and 2DEG plane. In other words, the Hall signal depends on the coupling between the nanomagnet stray field and 2DEG. Figure 4.11 shows a picture of the ferromagnetic,

single domain nanowire with easy axis perpendicular to the device surface. Black lines represent the 2DEG.

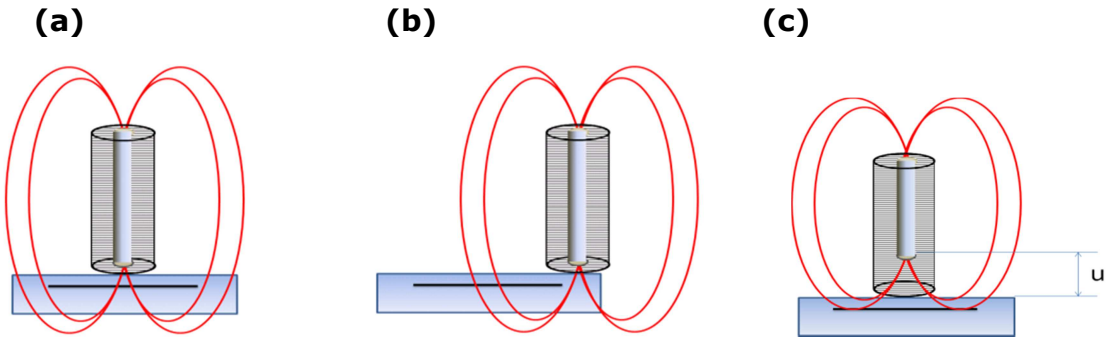

Figure 4.11: *Position of the nanowire embedded inside the carbon nanotube on the active are in respect to the edge of the active area. Black line corresponds to the 2DEG. (a) The nanowire is placed almost at the center of the active area of the device. The majority of the wire stray field lines penetrate the active are of the device. The coupling between the stray field and 2DEG plane is most optimal and Hall signal in this configuration is maximal, (b) the nanowire is located near the edge of the Hall cross, some of the lines of the stray field do not contribute to the Hall voltage, (c)the iron nanowire is located high above the active area. This has strong influence on the Hall signal, since less of the lines of the stray field contribute to the Hall voltage.*

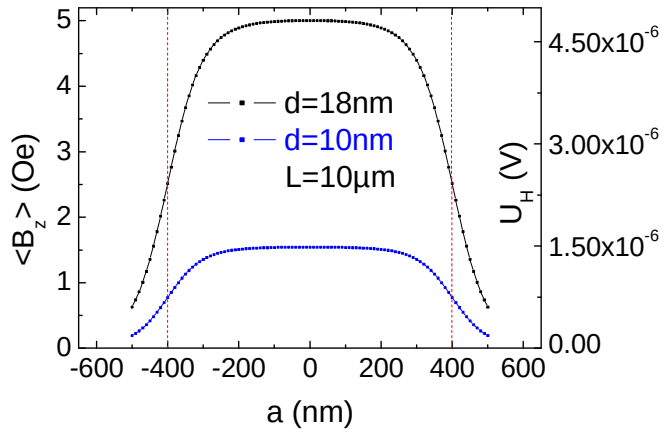

Figure 4.12: *The dependence of the average stray field <Bz> and measured Hall voltage of two iron nanowires d =18 nm and d =10 nm, L = 10 µm (u = 200 nm) on the distance* ***a*** *from the center of the active area along the channel. Each point was calculated by integration the eq.3.2 over the active area. Hall voltage was calculated for R_H=4,8 kΩ/T, I=2 µA.*

In case a) when the nanowire is placed close to the center of the active area most of lines of the stray field enter the sensing part of the device. In case b) the end of the nanowire is close to the edge of the active area and as we can see, only a few lines of the stray field penetrate the sensing part of the device. Thus the contribution of the stray field to the Hall signal based on this drawn is expected to be higher when the nanowire ends lies close to the center of the active area than at the border (Fig. 4.11a). Besides the position, the distance between the nanowire and 2DEG plane has strong influence as shown in figure

4.11c. Thus the precise manipulation method has to be applied in order to place the nanowire end near the center of active area of the device. Since Fe-filled CNTs are grown as a bulk material we used a high precision and high accuracy method of manipulation of an individual Fe-filled CNT.

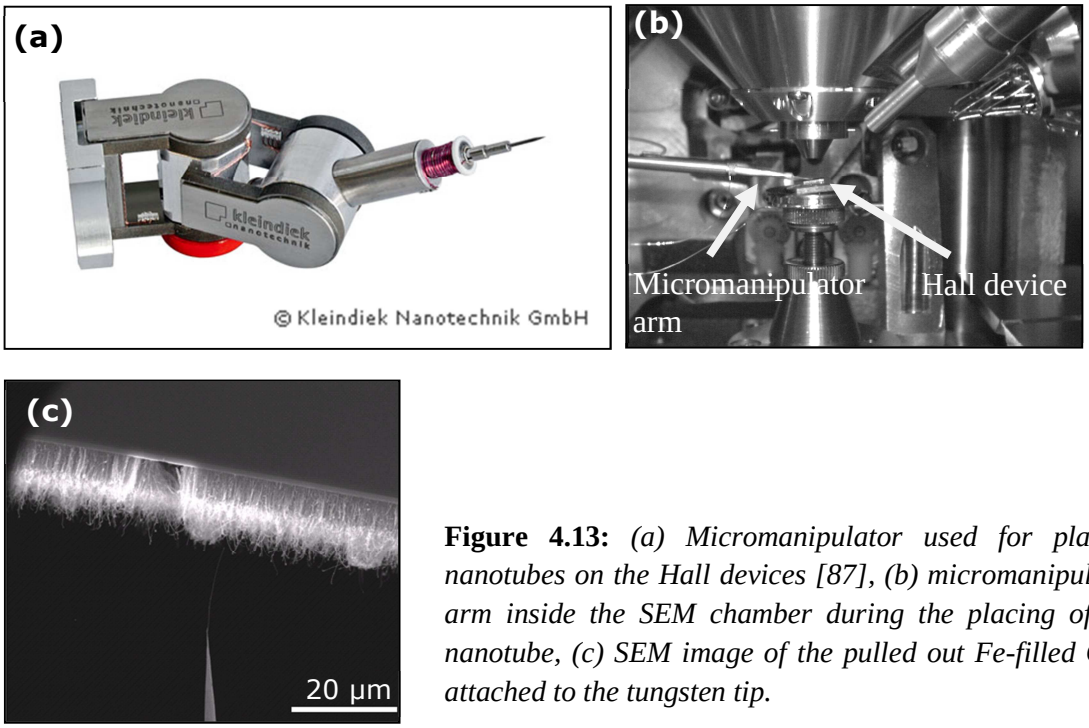

Figure 4.13: *(a) Micromanipulator used for placing nanotubes on the Hall devices [87], (b) micromanipulator arm inside the SEM chamber during the placing of the nanotube, (c) SEM image of the pulled out Fe-filled CNT attached to the tungsten tip.*

For this purpose we use a Kleindiek three-axis (x,y,z) piezoelectric micromanipulation system (Fig. 4.13 a-b) installed in the chamber of SEM. A tungsten tip with a very sharp end of around few tens of nanometer in diameter is attached to the manipulator arm. The fact that some of the nanotubes are longer and stick out of the ensemble makes them easily accessible thus one can approach the tiny end of the tip to the selected nanotube. The exposure to the electron beam under high magnification (ranging of 150 000) of the little contact area between the tip and nanotube causes the deposition of the residual carbon containing contaminations onto the area. The tip is then retracted and in most of the cases Fe-filled CNT is successfully pulled out (Fig. 4.13c). The nanotube can be then characterized in the microscope i.e. by measuring the outer and inner diameter, filling length. Moreover by application rotating of the tip it is possible to observe the exact shape of the nanotube.

Nanotubes often stick together and contain of many iron catalyst particles and different filling ratio. The micromanipulator lets to select the Fe-filled CNT with high purity,

without Fe catalyst particles surrounding the nanotube and homogenous filling suitable for micro Hall experiments.

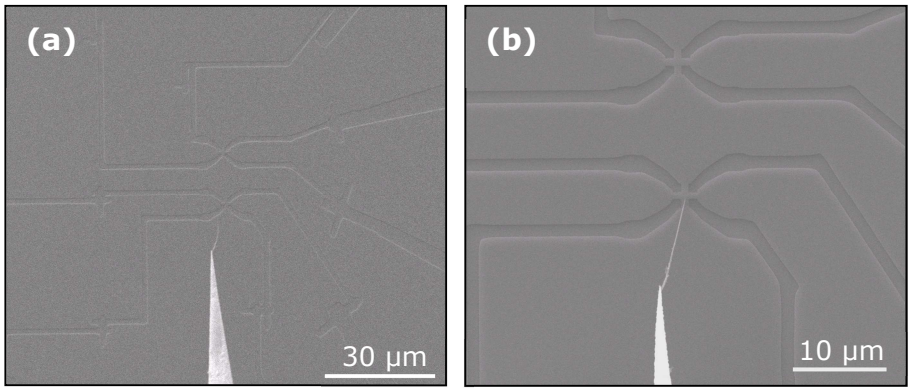

Figure 4.14: *SEM image of the Fe filled nanotube attached to the tip during the manipulation. (a) Tip approaches the surface. The distance between the nanotube and the device surface is estimated based on the difference in focus for surface and nanotube, (b) retraction of the tip. The connection between the nanotube and surface should be stronger than attachment of the tube to the tip.*

To attach the nanotube to the surface of the Hall device it is necessary to bring the end of the nanotube close to the surface and deposit carbon contaminations onto the touching area. To assure that the Fe-filled CNT remains on the sample after retracting the tip, its connection to the GaAs surface needs to be stronger than that to the tungsten tip. One can control the strength of the attachment by varying parameters such as time of exposure or beam current. Typical time of the exposure during attaching the nanotubes to the surface is around 20 min with an acceleration voltage 15 kV. The manipulation is shown in figure 4.14 a-b. Because the sample surface is very sensitive towards scratches the tip must approach the device plane with certain angle in order to prevent the device surface from mechanical contact with the manipulator. As a result the nanotube forms some large angle with the surface after the placement (see Fig. 4.15a). The magnetic field applied in micro Hall experiments may cause bending of the nanotube but also our experimental setup let us to measure magnetic properties with field applied parallel to the surface device. Thus we tend to place the nanotube entirely lying on the plane. This can be achieved by additional step. To let the nanotube fall down (Fig. 4.15b) on the surface we can etch the connection between the nanotube and the surface. Etching of the carbon containing contaminations which glued the nanotube to the surface is achieved by exposing the connection part in electron beam under the low vacuum mode in water vapor

environment. Usually the applied water pressure is around 0.2 mbar, an etching doses of about 10.000μC/cm^2 with the acceleration voltage V_A = 5kV.

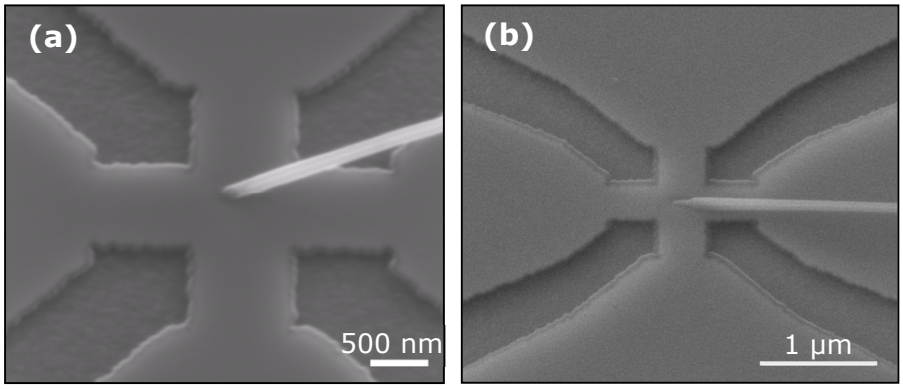

Figure 4.15: *SEM image of the Fe filled nanotube attached to the micro Hall device. Pictures are made with plane tilt 45^o. (a) The nanotube forms large angle with the surface >30^o, (b) after etching the connection in the water vapor environment between the tube and the device surface the nanotube fell down onto the surface.*

4.8. Hall voltage measurement technique

The substrate with patterned devices is glued with GE varnish to a homemade chip carrier with cooper electrodes (Fig. 4.16a). The electrical connections between sample and chip carrier are made with thin (25 μm), bonded with ultrasound aluminum wires. The probe head, screwed to the probe stick is made of copper and wrapped with the heating cable (Fig. 4.16b). The chip carrier with the sample is screwed to the probe head (Fig 4.16c). The connections between the chip holder and socket at top of the rod are realized by copper cables via top cap with electrodes. The schematic picture of the setup used in micro Hall experiments is shown in figure 4.17.

We used a commercial-type cryostat (Oxford Teslatron) with maximum in plane magnetic field of 18 T, generated by superconducting coils immersed in liquid helium. The field sweep rate used in experiments was between 0.1 - 0.5 T/min. A variable temperature insert (VTI) allows varying the temperature continuously from 5 to 240K, by evacuation liquid helium with different rates. For precise measurement of the temperature at the device an additional cernox temperature sensor is mounted in close proximity samples. This sensor was calibrated having the VTI sensor as a reference. The temperature is read by Lakeshore 340 temperature controller. Hall voltage measurements

were performed with lock-in technique with fixed frequency 937 Hz. In the work we use digital lock-in amplifier Stanford Research SR 830 DSP.

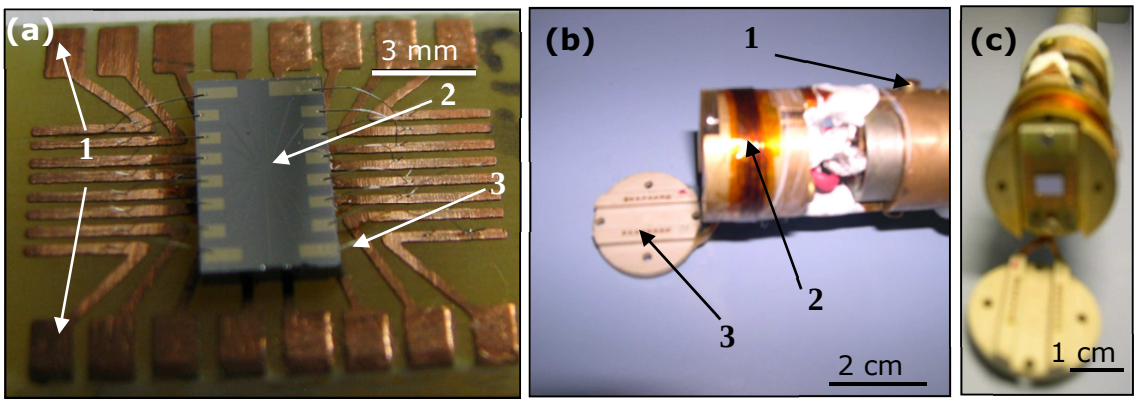

Figure 4.16: *(a) Homemade chip carrier made of plastic with 1-cooper electrodes, 2-the Hall sensor is glued via GE varnish to the chip carrier, 3-the device is connected to the chip carrier via thin (ϕ =25 μm) aluminum wires, (b) 1- The probe head made of cooper is screwed to the probe stick, 2-probe head is wounded with heating cable, 3-top cap with 16 electrodes is connected to the socket at the top of probe head via the cooper cable, (c) chip carrier is screwed to the probe head and finally top cap is screwed on the top.*

The output of lock-in oscillator is connected to the 100 kΩ resistor and the channel of the device (with resistance of few kΩ at low temperatures) grounded from the other side. This provides an AC current with constant amplitude, well-defined frequency f_0 and phase flowing throw the current path of the Hall cross. The injected current through the Hall probe is in a range of a few μA. The advantage of the AC technique in comparison to the DC method is that the measured Hall voltage with frequency corresponding to that of injected current over the wide range of selectable frequencies is detected, amplified and evaluated. This method lets to suppress noises effectively. Measured values were integrated every each 100 ms, and the set of data Hall voltage and magnetic field was read and stored by the program every each 100 ms. The angle between the external magnetic field and the nanomagnet placed on the active area of the micro Hall device could be changed by rotating the probe stick around its long axis.

The Hall coefficient measurements were performed in the Oxford Teslatron with perpendicular magnetic field 9 T.

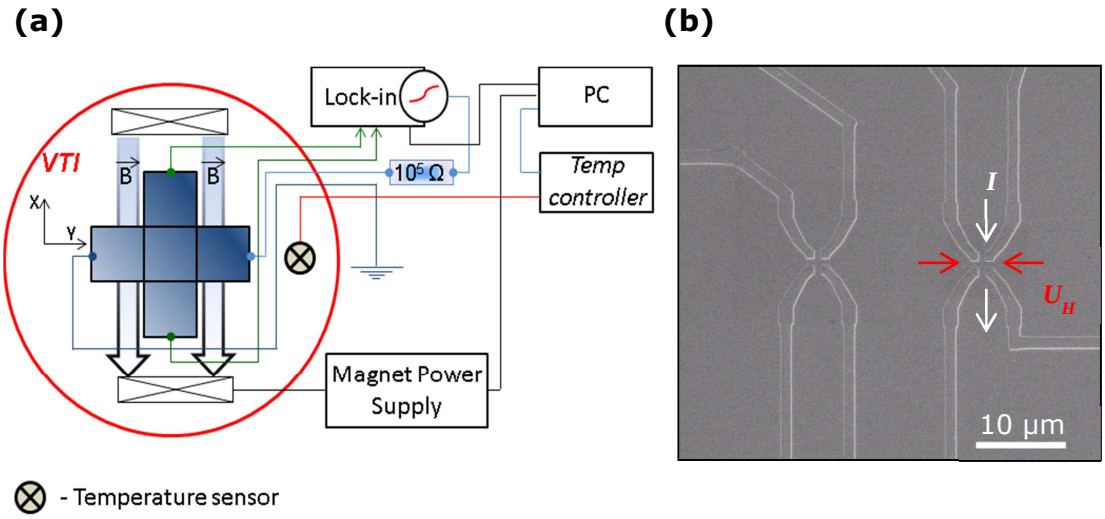

Figure 4.17: *(a) Schematic picture of four terminals experimental setup used in experiments. External magnetic field is applied parallel to the Hall sensor, (b) SEM picture of typical Hall device used in experiments, with marked current and voltage paths.*

5. Magnetism of CNT ensembles

5.1. Diamagnetism of pure carbon nanotubes

Usually, CNT are synthesized by virtue of magnetic catalyst particles in the chemical vapor deposition method[4]. However, the remaining catalysts affect the magnetic properties of the resulting material. Interestingly, from the variety of materials investigated as potential catalysts, the ferromagnetic ones such as iron, cobalt, nickel and their alloys exhibit the highest activity for catalyst based growth of carbon nanotubes [88,89,90,91,92,93,94]. On the other hand, pure carbon structures are supposed to exhibit only weak diamagnetic susceptibilities so that even extremely small residual catalyst material present in the CNT would dominate the magnetic response. In particular, a ferromagnetic-like response is often observed in the pristine Fe catalyzed CNT samples.

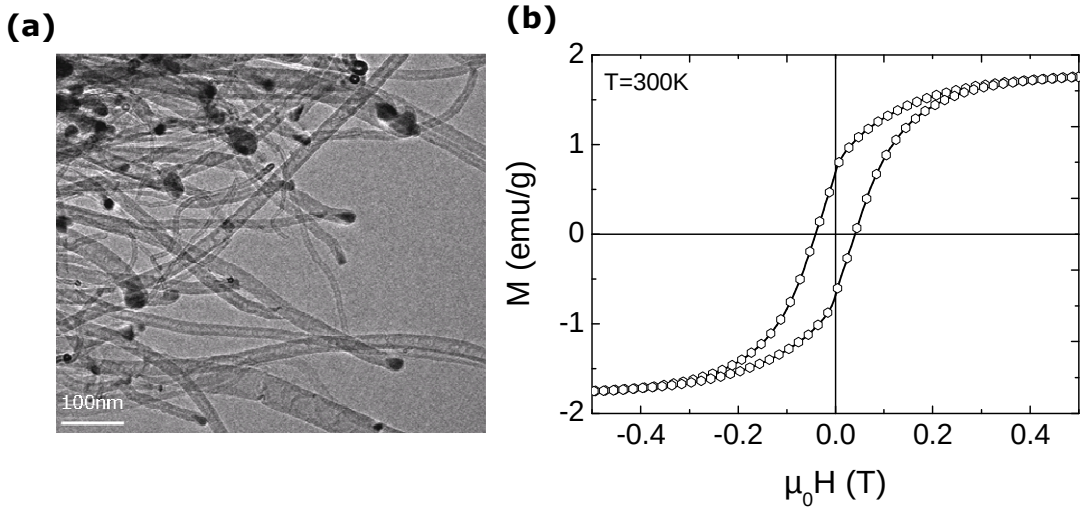

Figure 5.1: *(a) TEM image of Fe-catalyzed CNTs, synthesized by using acetonitrile as solvent, (by Dr. M. Ritschel, IFW Dresden), (b) the hysteresis loop for the powdered sample was measured at room temperature in magnetic fields up to 0.5 T. [95]*

Even a purification process, e.g. washing the tubes in nitric acid after the synthesis, does not eliminate the catalyst contamination completely. This is illustrated in figure 5.1a by TEM picture where iron catalyst particles are visible and by magnetization measurements (Fig. 5.1b) where a clear ferromagnetic hysteresis is seen superimposing the expected diamagnetic properties of the pure material. The data imply a broad hysteresis with a coercivity of 400 Oe and the magnetization at $\mu_0 H = 0.5$ T amounts to $M_S = 1.76$ emu/ g.

[4] Parts of the following text have been published in [95].

In this particular case, the material contains Fe catalyst nanoparticles which had been utilized during synthesis. Taking into account the saturation magnetization of bulk α - Fe (M_{bulk} = 212 emu/g), we conclude that $m_{Fe}/m_{CNT} \approx 0.01$ in this case.

We discuss two different ways to obtain diamagnetic CNTs, which are as follows: (1) by post synthesis evaporation of catalyst particles at extremely high temperatures and (2) by using nonmagnetic catalyst material Re. For approach (1), Fe-containing CNTs have been synthesized by aerosol-assisted CVD. This method is based on a liquid starting material consisting of a metal organic catalyst compound ferrocene solved in a hydrocarbon (cyclohexane or acetonitrile). This solution was nebulized in an ultrasonic generator and injected directly into the quartz tube reactor diameter of 4 cm and length of 120 cm. A transport gas consisting of 50 % argon and 50 % hydrogen was used. The total flow rate was kept at 1300 sccm and the reactor temperature at 800 °C.

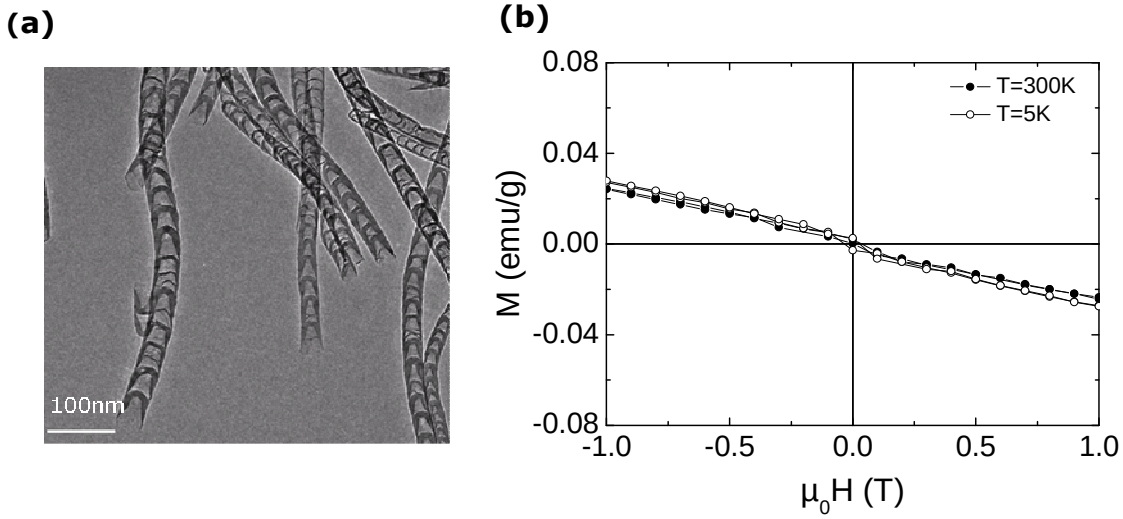

Figure 5.2: *(a) TEM image of Fe as a catalyst carbon nanotubes, synthesized by using acetonitrile as solvent and after re-annealing at 2500 °C under argon. The image confirms removal of Fe catalyst nanoparticles,(by Dr. Ritschel IFW Dresden) (b) diamagnetic behavior of Fe-based empty nanotubes after annealing the sample in argon atmosphere at 2500 °C. [95]*

The prepared Fe-based CNTs were annealed at the temperature 2500 °C and under argon atmosphere. After the process, TEM images show no signature of Fe-catalyst particles as displayed in figure 5.2a. These CNTs exhibit outer diameters between 10 and 40 nm. A magnetization studies are shown in figure 5.2b. The magnetization is linearly decreasing upon increasing the external magnetic field in the positive range and an opposite behavior is observed in the negative range of the applied magnetic field. This behavior unambiguously implies a diamagnetic response and shows the absence of any measurable

contribution of magnetic Fe. The data at T = 5 K strongly confirm the absence of any magnetic impurities since paramagnetic ions, e.g., individual Fe ions, would result in a Curie-like increase in the magnetization which is clearly not observed.

The Raman studies have been performed with Bruker Fourier Transform Raman spectrometer (λ = 1064 nm) on the sample before and after annealing[5].

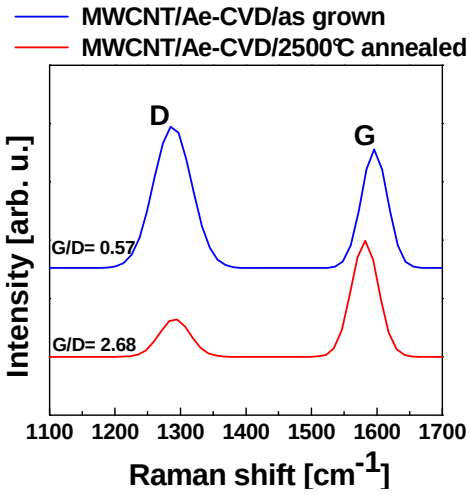

Figure 5.3: *Raman spectra of the region presenting D- (defect mode) and G- (graphitic mode) peaks (sp^2 carbon presence) for carbon nanotubes synthesized on the Fe catalyst particles, before (blue line) and after annealing (red line) at 2500 °C under argon atmosphere. The relative ratio of G/D areas increases upon the annealing from 0.57 to 2.68. This indicates the improvement of the graphitic crystal structure quality after the heating treatment, (measured by Dr. M. Ritschel, IFW Dresden)*

The technique probes the vibrational, rotational, and other low-frequency modes in the investigated sample. The sample is irradiated with monochromatic laser light, and non-elastic scattering of photons on molecular vibrations, phonons and other excitations causes a shift of the photons energy. The Raman effect is the process in which photons interact with the binding electron cloud. The absorbed photon excites the system to a virtual state. While the system relaxes to its original ground state it emits a photon with shifted frequency with respect to the original photon. The negative shift in the frequency of the photon is called Stokes shift, while the positive shift is Anti-Stokes shift. The vibrations are specific to the chemical bonding and symmetry of the system. Thus on the basis of the shift in the Raman spectra the molecules can be identified. The Raman shift can be expressed by the formula:

$$\Delta\omega = \left(\frac{1}{\lambda_0} - \frac{1}{\lambda_1} \right) \tag{5.1}$$

where, λ_0 is the excitation wavelength, and λ_1 is the Raman spectrum wavelength.

[5] Raman experiments were performed by Dr. M. Ritschel , Institute for Solid State Research, IFW Dresden.

Typically in case of carbon nanotubes two allotropic forms of carbon dominate; amorphous carbon with bonding sp^3 and graphitic sp^2 carbon.
Both gives different Raman shift, D (defect mode) ascribed as defect peak at wavenumber $\omega \approx 1280\ cm^{-1}$ and G (graphitic mode) associated with graphitic peak wavenumber $\omega \approx 1580\ cm^{-1}$.

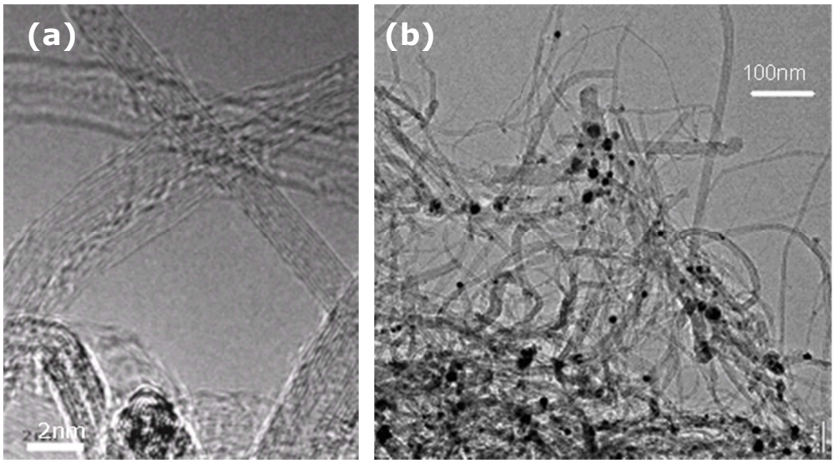

Figure 5.4: *(a) A typical TEM image of Re-catalyzed carbon nanotubes after washing process. (b) TEM-image of Re-catalyzed carbon nanotubes after annealing at 2300 °C under argon. Re-particles are still present (images made by Dr. Ritschel).[95]*

We observed the increase of the G/D areas ratio (Fig. 5.3) after the sample was annealed. The relative ratio of G/D areas increased upon the annealing from 0.57 to 2.68. This can be explained by high temperature annealing of the sample the amorphous carbon contaminations are eliminated while the crystallinity of the graphitic structure is improved.

The second set of samples was made using Re as catalyst by the fixed-bed method [96]. A TEM image of the Re-catalyzed carbon nanotubes is shown in figure 5.4a. Re-catalyzed CNTs are observed with an averaged diameter of 3 – 8 nm. Moreover, individual double-walled CNTs (DWCNTs) and bundles of single-walled CNTs (SWCNTs) are also observed. After the annealing process at 2300 °C in vacuum, the Energy-dispersive X-ray (EDX) analysis show that annealed CNTs consist of only Re and carbon, while any impurities such as iron are not observed. This observation is corroborated by classical chemical analysis which yields Fe and other foreign metal concentrations lower 0.01 wt %. The chemical analysis results a Re concentration of 3.80

wt % for the as-grown Re catalyzed CNTs and from 4.5 wt % for the annealed Re catalyzed CNTs. The TEM image (Fig. 5.4b) confirms dark nanoparticles of Re and the carbon nanostructures.

The magnetization of Re-catalyzed CNT at T = 300 K and at T = 5 K is shown in figure 5.5. Similarly as discussed above, the magnetic field dependence of the magnetization is linear and exhibits a negative slope, which again demonstrates the diamagnetic properties of the material and confirms absence of significant amounts of ferro- or paramagnetic impurities.

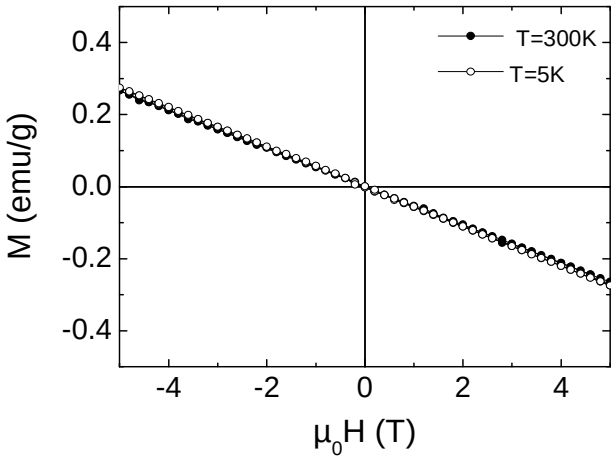

Figure 5.5:
Diamagnetic behaviour of Re supported carbon nanotubes. After the synthesis procedure the sample was annealed at 2300 °C. [95]

Accordingly, also the temperature dependence of the magnetic susceptibility $\chi = dM/dH$ is very weak. Quantitatively, the magnetic susceptibility at $\mu_0 H = 0.5$ T and T = 300 K amounts to $\chi = (-2.7 \pm 0.5) \cdot 10^{-6}$ emu/g for the annealed nanotubes from approach (1) and to $\chi = (-4.6 \pm 0.1) \cdot 10^{-6}$ emu/g for the Re-catalyzed ones. These values are in agreement with the range of values previously reported for carbon structures [97,98,99].

The usage of non-magnetic catalysts or a high temperature annealing procedure render the material diamagnetic as expected for a pure carbon structure.

5.2. Pristine carbon nanotubes: magnetism of catalyst nanoparticles

It has already been mentioned above that magnetization measurements are sensitive to magnetic impurities and hence can provide information about their presence. In addition, magnetic measurements can be used as a very sensitive measure of the amount of magnetic particles inside the sample while conventional methods such as Energy-

dispersive X-ray spectroscopy (EDX), X-ray photoelectron spectroscopy (XPS) or X-ray Diffraction (XRD) might fail to detect trace amounts of magnetic material[6]. Several different batches of empty carbon nanotubes were prepared using a variety of ferromagnetic catalyst materials and various synthesis methods.

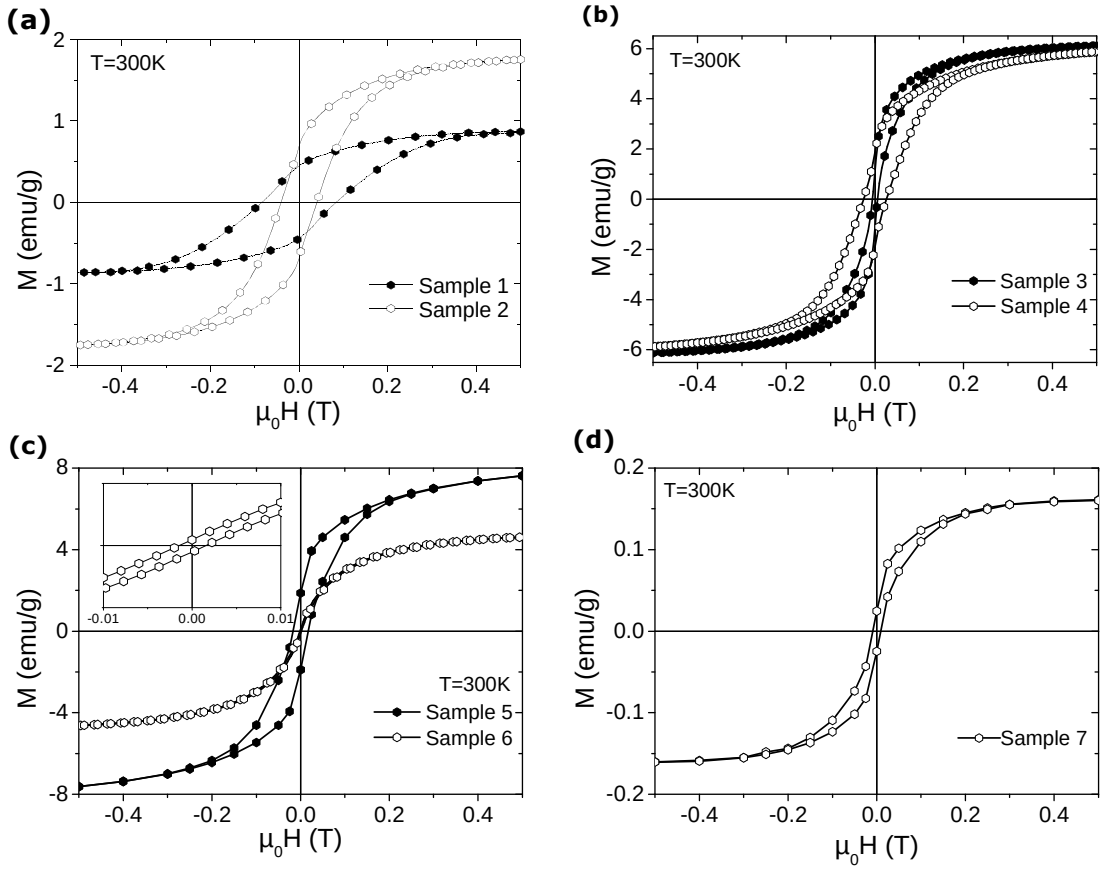

Figure 5.6: *Magnetization vs. magnetic field at T = 300 K for (a) sample 1, CNT made by the fixed bed method with FeCo catalyst and sample 2, made by the AA-CVD method. (b) Sample 3, a single- and double-walled CNT mixture and sample 4, CNT, both made by the fixed bed method with Fe catalyst. (c) Sample 5, MWCNT by the AA-CVD method with Fe catalyst and sample 6, SWCNT from NanoLab synthesized by CVD with Fe as catalyst. (d) Sample 7, CNT from Bayer Material Science prepared by CVD with Fe as catalyst. [100]*

A set of seven different powder samples of CNT prepared with 50% FeCo alloy catalysts (sample 1) and pure iron catalyst (samples 2-7) were examined. The fixed bed method [101] was used for the synthesis of samples (1), (3) and (4), while aerosol assisted CVD was used for samples (2) and (5). In addition, commercially available single-walled

[6] Parts of the following text have been published in [100].

carbon nanotubes (SWCNT) from Nanolab Inc. (sample 6) and CNT from Bayer Material Science (baytubes C150 HP) (sample 7) have been studied. Room temperature magnetic measurements were performed in magnetic fields up to 0.5 T employing AGM and SQUID magnetometers. The results of these measurements are shown in figure 5.6. The experimental data shown in figure 5.6 demonstrate a ferromagnetic-like behavior of all samples. In particular, diamagnetism of the carbon shells is masked by the magnetism of the catalyst particles formed during and remaining inside the carbon nanotubes after the synthesis procedure. The M(H) curves provide relevant characteristic parameters such as the coercive magnetic field (H_C), the saturation magnetization (M_S) and the remanent magnetic moment (M_R). Indirectly, based on the saturation moment it is also possible to derive the density of the magnetic material in the sample. The respective values are listed in Table 1. Note, that the table includes also the mean diameter of the catalyst particles as extracted from TEM imaging. In addition we present the relative amount of ferromagnetic catalyst material in the sample, m_{cat}/m_{CNT}, which was deduced by comparing the measured saturation magnetization with its corresponding bulk values.

Sample	Synthesis	Catalyst	*d* (nm)	$\mu_0 H_C$ (mT)	*M*s (emu/g)	m_{cat}/m_{CNT} (%)
1	Fixed bed	FeCo	10 – 15	84.2	0.87	---
2	AA-CVD	Fe	~10	36.9	1.76	0.8
3	Fixed bed	Fe	1 – 5	5.8	6.1	2.9
4	Fixed bed	Fe	8 – 15	26.1	5.93	2.8
5	AA-CVD	Fe	10 – 20	20.0	8.2	3.8
6	CVD	Fe	---	1.5	4.84	2.3
7	CVD	Fe	2 – 6	12	0.16	0.07

Table 1 *Summary of TEM and magnetization analysis. d denotes the diameter of the respective catalyst particles as taken from TEM imaging, H_C and M_S are the coercive field and saturation magnetization from the data in figure 5.6 m_{cat}/m_{CNT} is the relative amount of magnetic material in the sample*.

As the magnetic properties of CNT are usually governed by the response of the catalyst nanoparticles, in the following we discuss the coercivities H_C for samples (1) and (2). According to table 1 the diameter of the catalyst particles are below the single domain limit, 12 nm for Fe [102] and 41 nm for bcc FeCo [103].

According to the model of Néel [104] the coercivity of our single domain, randomly oriented nanoparticles with cubic anisotropy is proportional to the magneto-crystalline anisotropy constant K_1, i.e. $H_C \sim K_1$. The values of K_1 found experimentally at room temperature are $K_1 = 4.8 \cdot 10^4$ J/m^3 and $K_1 = -1 \cdot 10^5$ J/m^3 for α-Fe and disordered BCC 50% FeCo alloy, respectively [105]. While the particle size is similar, we observe H_C(Sample 2) ~ $2 \cdot H_C$(Sample 1) which is consistent to the Néel model. The coercivity is strongly associated with the size of the magnetic nanoparticles. Two regions can then be distinguished, one for which the particle diameter is smaller than the single domain limit (12 nm for Fe), the other for larger multidomain particles. The coercive force in the single domain region is proportional to $\sim d^6$ [106]. Indeed, a rapid increase of the critical field with diameter manifests for samples (3), (7), (2) where H_C increases from 5.8 up to 36.9 mT. In contrast, for particles in the multidomain limit with diameters above 12 nm, H_C becomes smaller for larger particles, i.e. $H_C \sim 1/d$ [107]. This situation is realized in samples (2), (4), and (5), where the coercivity decreases from 36.9 to 20 mT with increasing particle size.

We can see very strong effects of the remaining catalyst particles on the magnetization of the material which renders magnetization studies a very sensitive tool for determination of residual catalyst material.

5.3. Magnetism of iron filled carbon nanotubes

Iron filled carbon nanotubes are prepared by means of thermal-catalytic chemical-vapor deposition (CVD) with ferrocene as precursor as described in several reviews, e.g. in [108][7]. This method is supposed to produce filled carbon nanotubes with a filling of more than 40 %, consisting of α-Fe, γ-Fe, and Fe_3C in different ratios depending on the sample preparation. Only α-Fe and Fe_3C exhibit ferromagnetic behavior at room temperature while γ-Fe is paramagnetic. The iron filling forms single crystal nanowires of

[7] Parts of the following text have been published in [109].

lengths up to 20 µm, coated by carbon shells. A SEM image of such homogenous ensembles of Fe-filled CNT grown onto a silicon substrate is shown in figure 5.7a. The magnetization was measured by means of the AGM at room temperature parallel and perpendicular to the oxidized silicon substrate (Fig. 5.7b). Fe-filled CNTs tend to grow perpendicular to the substrate plane and form an almost homogenous 'forest' of nanotubes (see Fig. 5.7b).

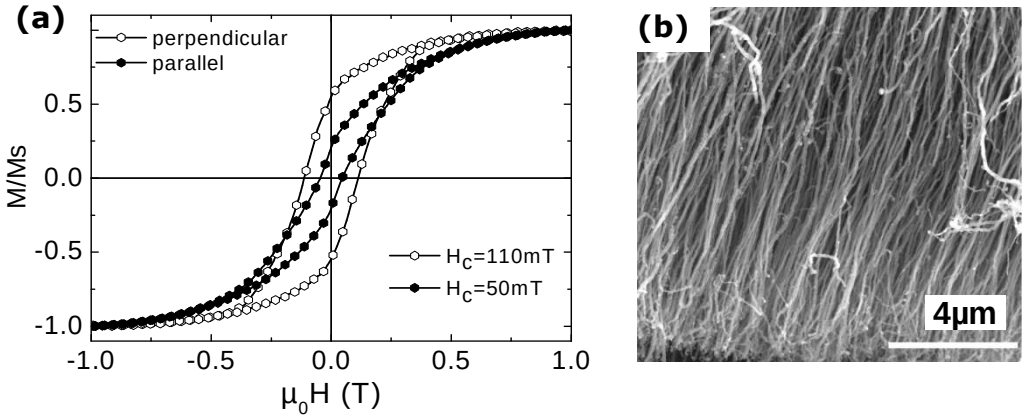

Fig. 5.7: *(a) Magnetization curve M vs. H of Fe-filled CNT grown on a silicon substrate measured at room temperature parallel and perpendicular to the substrate. (b) SEM image of the same material. [109]*

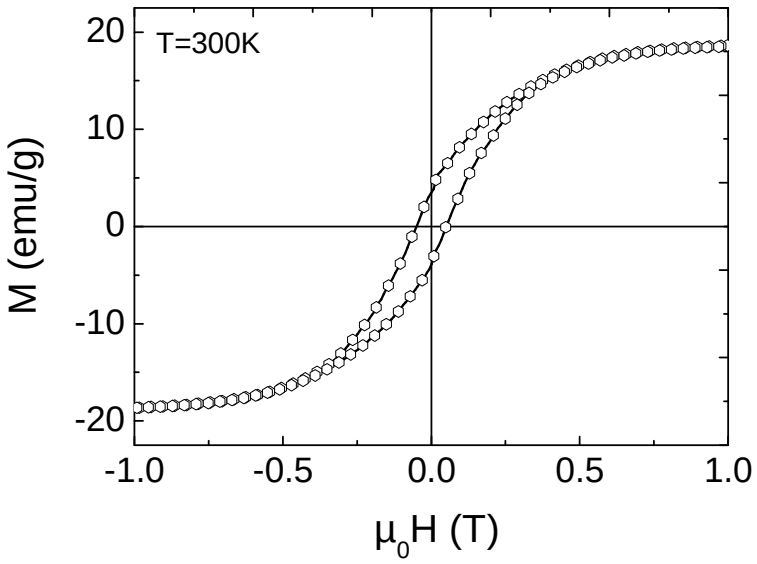

Figure 5.8: *Magnetization curve M vs. H of Fe-filled CNT powder at room temperature.*

The ferromagnetic α-Fe nanowires encapsulated by carbon nanotubes exhibit uniaxial magnetic anisotropy with the easy axis parallel to the long axis of the nanowires, leading to an enhanced magnetic coercivity ranging up to ~110 mT and ~50 mT in perpendicular and parallel direction to the substrate, respectively.

The coercivity measured when the magnetic field was applied almost parallel to the long axes of the nanowires is about two times smaller than the switching fields measured almost along the easy axis for an individual iron nanowire (see Fig. 5.7a, Fig. 6.5 c-d). The explanation of the decrease of the coercivity for ensembles of Fe nanowires is the fact that dipolar interactions between the nanowires in the ensembles reduce their switching fields. However, the elongated shape of the nanowires raises their magnetic shape anisotropy and in consequence the coercivity of Fe nanowires in ensemble is still significantly higher than the one measured for CNT with iron catalyst particles. This can be explained by the fact that the single wire measurements were conducted on MWCNT deliberately chosen for their long and homogeneous filling, resulting in a large shape anisotropy with corresponding high switching fields. Such wires are estimated to contain a minority of the iron found in the whole sample. The rest is made of short and/or inhomogeneous wires and catalyst particles, all of which have a much lower switching field. The response of the ensemble is therefore only of limited value for shedding light on the magnetic properties of the nanowires. In order to determine the relative amount of iron in the Fe-filled CNT by means of magnetometry, these Fe- filled CNT were removed from the substrate and measured as a dry powder. Figure 5.8 provides an example of a M(H) curve measured on the powder sample. At room temperature, Fe-wire-CNT powder shows a coercivity $\mu_0 H_C$ = 50 mT and a saturation magnetization M_S = 18.6 emu/g_{CNT}. Comparison with the saturation magnetization of bulk iron M_{bulk} = 212 emu/g reveals a mass ratio of iron in Fe-filled CNT of 8.7 %. Remarkably, a comparison between Fe-filled CNT and Fe-cat-CNT discussed in the previous subsection implies that the amount of ferromagnetic iron inside the Fe-filled CNT is only two times higher than in pristine ones. However, although it is known that catalyst material is also present in the Fe-filled CNT, the amount of catalysts cannot be assessed. One might speculate that iron nanowires form at the expense of some catalyst material but a separation of the magnetic signal of Fe-filled CNT into the response of nanowires and catalyst, respectively, is not possible by means of the data at hand.

5.4. Summary and discussion

The magnetic properties of CNT without ferromagnetic impurities have been studied. The data confirm the absence of any detectable amount of ferromagnetic impurities, thereby confirming efficiency of post – annealing process applied. The absence of ferromagnetic impurities is also confirmed for CNT made by virtue of Re catalyst. For CNT made with conventional ferromagnetic catalysts the data shows strong effects of the remaining catalyst particles on the magnetization of the material. This renders magnetization studies a very sensitive tool for determination of residual catalyst material.

6. Magnetism of individual iron filled carbon nanotubes

6.1. Micro Hall studies on an individual straight iron nanowire

6.1.1. Experimental details

The micro-Hall device introduced in subchapter 4.8 and shown in figure 6.1 has a longitudinal resistance between 3 kΩ and 6 kΩ (T = 10 K), depending on the path and the Hall coefficient R_H = 4.8 kΩ/T (10 K)[8]. Figure 6.1 shows a SEM picture of the Hall cross with an individual Fe-filled CNT placed near the center of the active area.

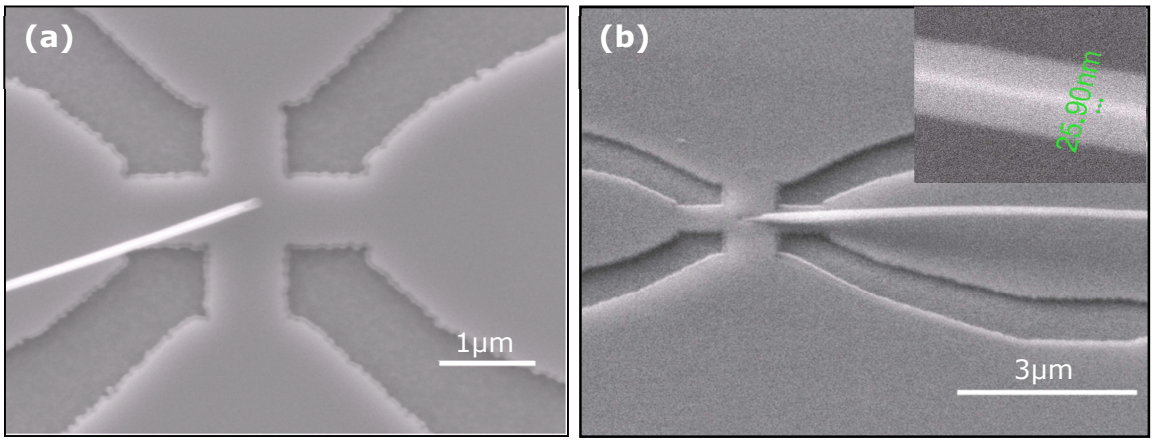

Figure 6.1: *SEM image of the 26 nm diameter Fe nanowire inside the CNT placed at the center of a 0.8 × 0.8 µm² active area of the Hall device made on GaAs/AlGaAs 2DEG heterostructure, electron density n = 4.6·10¹¹ cm⁻² and mobility µ = 2·10⁵ cm²/Vs, measured at T = 1.5 K and in the dark. (a) Top view image, (b) image taken when the plane of the sample was tilted with an angle 60°, the nanotube forms an angle ≈ 12° with respect to the surface. Inset: high magnification BSE image of the Fe-filled CNT. [110]*

For these experiments we chose a high purity Fe-filled CNT, without visible Fe catalyst particles surrounding the nanotube as studied by SEM. The filling was investigated under SEM and we determined the diameter to be d ≈ 26 nm (Inset of the figure 6.1b). The SEM study showed that the nanowire was homogenous over its entire length, L ≈ 15 µm. The Fe-filled CNT was placed onto the device (the procedure is described in subchapter 4.7.) in such a way that the small area of the nanotube at its end was touching the GaAs surface

[8] Parts of the following text have been published in [110]

(Fig. 6.1b). In order to fix the nanotube to the surface we focused the electron beam onto the nanotube over a large area ≈ 300 × 300 nm^2 (this exposure results in the deposition of carbon containing contaminations on the sample). However, it did not stick completely to the surface and further investigations with SEM showed that its long axis formed an angle ≈ 12^o with respect to the surface, near the active area of the micro-Hall device. Under these conditions, it was not possible to measure the switching of the magnetization with angles between the field and the Fe-filled CNT axis of -12^o ≤ θ ≤ 12^o since the experimental setup only allowed us to perform micro Hall-experiments with magnetic fields applied in the plane of the device.

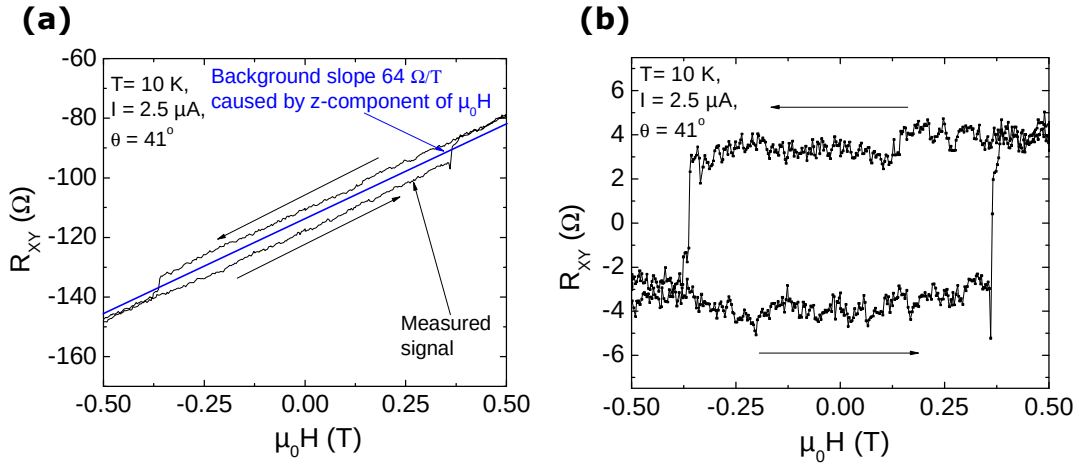

Figure 6.2: *The raw hysteresis loop measurement. (a) The hysteresis loop is tilted due to non-zero z-component of the external magnetic field applied in plane of the sample surface. The device is not perfectly aligned with respect to the magnetic field. The slope of the background signal amounts to S = 64 Ω/T, (b) the hysteresis loop after the subtraction of the background signal.*

However, as it will be shown later (subchapter 6.1.3) the angular dependence of nucleation fields provided us with valuable information to describe the magnetization reversal mechanism. The device is not perfectly aligned with respect to the magnetic field, which results in the tilting of the hysteresis loop due to a finite perpendicular component of the external magnetic field. Nevertheless this linear background can be easily subtracted from the raw data as shown in figures 6.2 a and b. The blue line in figure 6.2 a represents the signal which comes from the perpendicular component of the external magnetic field and it is drawn based on the symmetry of the hysteresis loop. The analysis

of the background signal gives a tilt angle $\alpha = 0.8^o$ ($tg\alpha = S/R_{H1}$ where R_{H1} is the Hall coefficient measured in a perpendicular field, while $S = 64\ \Omega/T$ is the slope of the background signal[9]).

The experimental setup probes the Hall voltage generated by the z-component (perpendicular to the sensor surface) of the stray field emanating from the nanowire and penetrating the active area of the sensor as a function of an external magnetic field and temperature. This local measurement technique is mainly sensitive to the stray field at one end of the magnetic wire. Since MFM studies on our nanowires [55] have clearly confirmed that the remanent magnetization state is always a single domain state in straight nanowires, the micro Hall data can be straightforwardly attributed to the magnetic properties of the entire wire. The carbon shells protect the nanowire against oxidation, which retains its ferromagnetic properties [111,112] and the CNT itself provides only a very weak diamagnetic signal with a susceptibility weakly dependent on the temperature $\chi = (-2.7 \pm 0.5) \cdot 10^{-6}$ emu/g (see subchapter 5.1). Therefore the diamagnetic signal created by the carbon shells is redundant and carbon does not disturb the magnetic measurements of the Fe nanowire. In our experiments we measured the field and temperature dependence of the Hall voltage created by magnetic stray fields of a single Fe nanowire at different temperatures and at different angles. After the full set of measurements was completed a careful analysis of the exact position of the CNT with respect to the device under the SEM was conducted in order to provide a correct angle θ which is the angle of applied external magnetic field with respect to the nanowire long axis (easy magnetization axis).

6.1.2. Hysteresis loop measurements

As already visible in figure 6.2, under a slow sweep rate of the external magnetic field ($v = 0.1 – 0.4$ T/min) jumps of the Hall voltage at negative and positive $H_{external} = H_n$ are observed which reflects a change of the magnetization in the iron nanowire. By performing the magnetic field sweeping experiments from negative to positive and back to negative magnetic fields one can get a hysteresis loop of the Hall voltage that is directly related to the hysteresis of the nanowire's magnetization reversal. As mentioned in chapter 3, in the ballistic transport regime i.e. at low temperatures the Hall voltage is directly proportional to the average z component of stray field $<B_z>$ in the active area.

[9] The derivation of the formula is given in an appendix.

We converted (equation 3.1) the Hall signal into a stray field value $<B_z>$ and observed that the remanent state creates an average stray field of about ≈ 7 Oe.

Hysteresis loops of the iron nanowire measured at relatively large angles are shown in figures 6.3 a and b. The nearly rectangular shape of the loops is similar to the magnetization reversal of single domain magnetic particles.

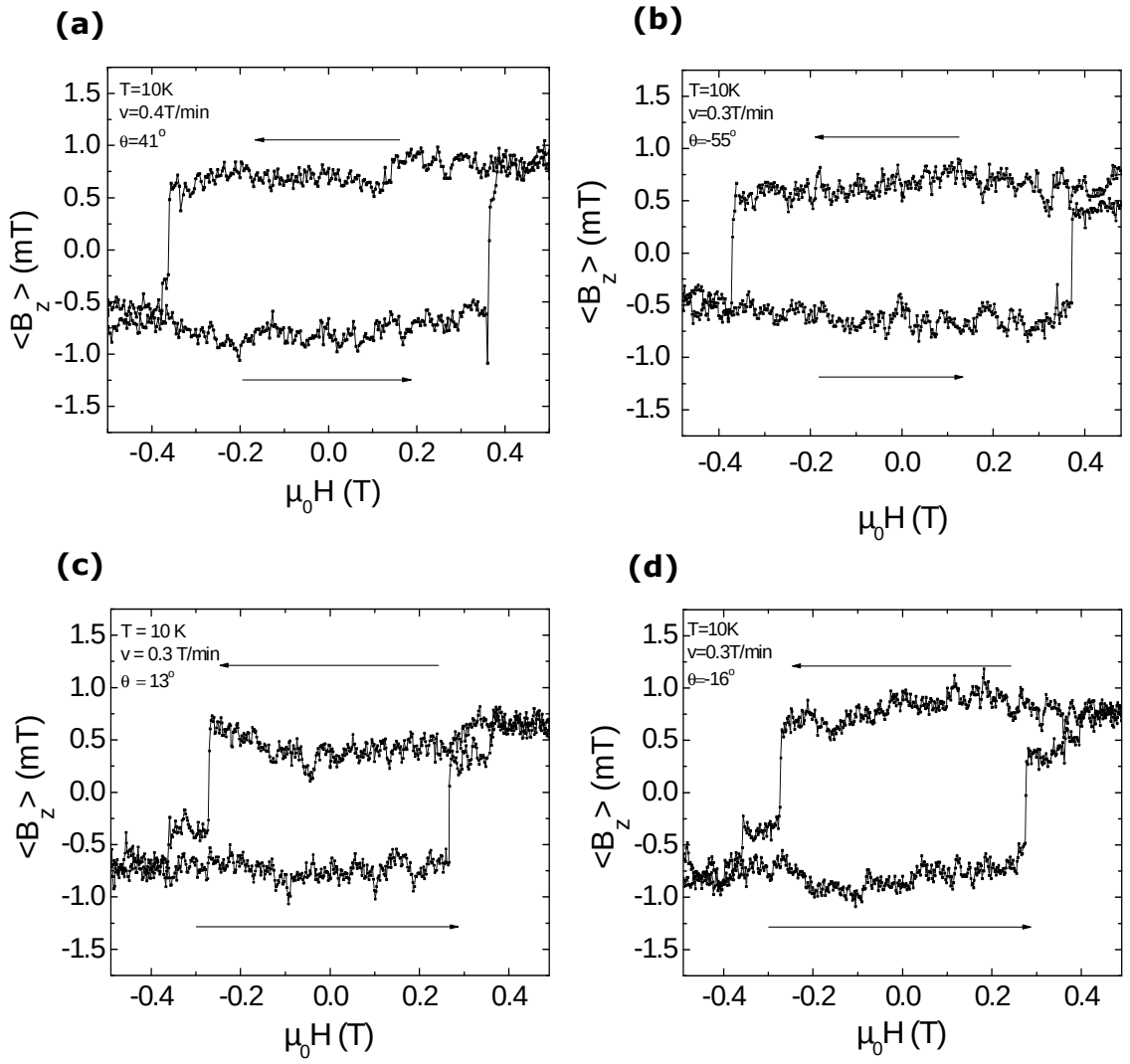

Figure 6.3: *Average magnetic stray field $<B_z>$ as detected by the micro-Hall magnetometer vs external magnetic field H, measured at T = 10K. (a) The square shape hysteresis loop with singular jumps (± 360 mT), measured at the angle $\theta = 41^o$, (b) the hysteresis loop with singular jumps (± 372 mT) measured at the angle $\theta = -55^o$, (c) the hysteresis loop with two steps measured at the angle $\theta = 13^o$. The lower field jumps (± 268 mT) correspond to the nucleation and pinning of a magnetic domain wall while tiny jumps at higher fields (± 368 mT) result from the depinning of the wall. Both jumps of $<B_z>$ are symmetric with respect to $\mu_0 H = 0$ T, (d) two step hysteresis loop measured at the angle $\theta = -16^o$. The lower field jumps occur at $\mu_0 H = \pm 272$ mT while the depinning fields equal $\mu_0 H = \pm 357$ mT. [110]*

Recent cantilever magnetometry studies [113] performed on a Fe-filled CNT with a 25 nm diameter of Fe nanowire from the same batch provided a similar picture of magnetization switching realized via a single jump. However, for small angles $|\theta| \leq 37^o$, we observed that the magnetization reverses by more than one individual step (Fig. 6.3 c-d). For the same conditions we repeated these experiments several times in order to confirm the reproducibility of such a second step in the hysteresis loops at small angles. Above the angles $\theta = 37^o$ the second jump disappears. We ascribe this phenomenon to a depinning of the domain wall during the magnetization reversal. The probable reasons for the pinning of the domain wall are small diameter variations of the nanowire, which locally change the anisotropy. Following the nucleation of the domain with reversed magnetization at one end of the nanowire the domain wall is pinned at a pinning center and a stronger external magnetic field needs to be applied to overcome this pinning and to complete magnetization reversal which results in additional steps in the hysteresis loops. At angles $|\theta| > 37^o$ the nucleation fields are already higher than the depinning fields and magnetization reversal takes place via singular steps without pinning as shown in figures 6.3 a and b.

Similar effects i.e. magnetization reversal of nanomagnets realized via two steps were already observed in Ni nanowires [114] and Co particles [115]. Moreover, *Wernsdorfer et al.* [114] did additional studies on such additional steps in the hysteresis loops measured for individual Ni nanowire and they among other things showed:

* a smaller temperature dependence of the depinning fields in comparison to the nucleation fields;
* a very narrow width of the depinning field distribution of about 0.03% of $<H_d>$.

We observed the large increase of the noise (see Fig.6.6a) with temperature. Thus the resolution of our experimental setup did not allow us to perform such detailed investigation of the temperature dependence of the depinning field.

6.1.3. Angular dependence of the nucleation fields

Typical measurements of the nucleation field of the nanowire at different angles are shown in figure 6.4. At first singular hysteresis loops were measured in order to determine the nucleation field at each angle. Then an external magnetic field $\mu_0 H = -1$ T was applied o switch the nanowire magnetization. With a fast sweeping rate (v = 0.5

T/min) the magnetic field was set to $\mu_0 H = 0.2$ T. Then the actual measurement of the nucleation field was performed with a small sweeping rate (v = 0.2 T/min). The entire procedure was performed several times for each angle. The results of these measurements for the angles θ = - 37°, - 61°, - 75°, - 85° are shown in figure 6.4. The measured nucleation fields were averaged and the angular variation $\langle H_n \rangle$ (θ) of the nucleation fields is shown in Fig. 6.5. We note slight deviations of $\langle H_n \rangle$ for the positive and negative values θ. This can be associated to an angular misalignment of ± 1° in the experiments.

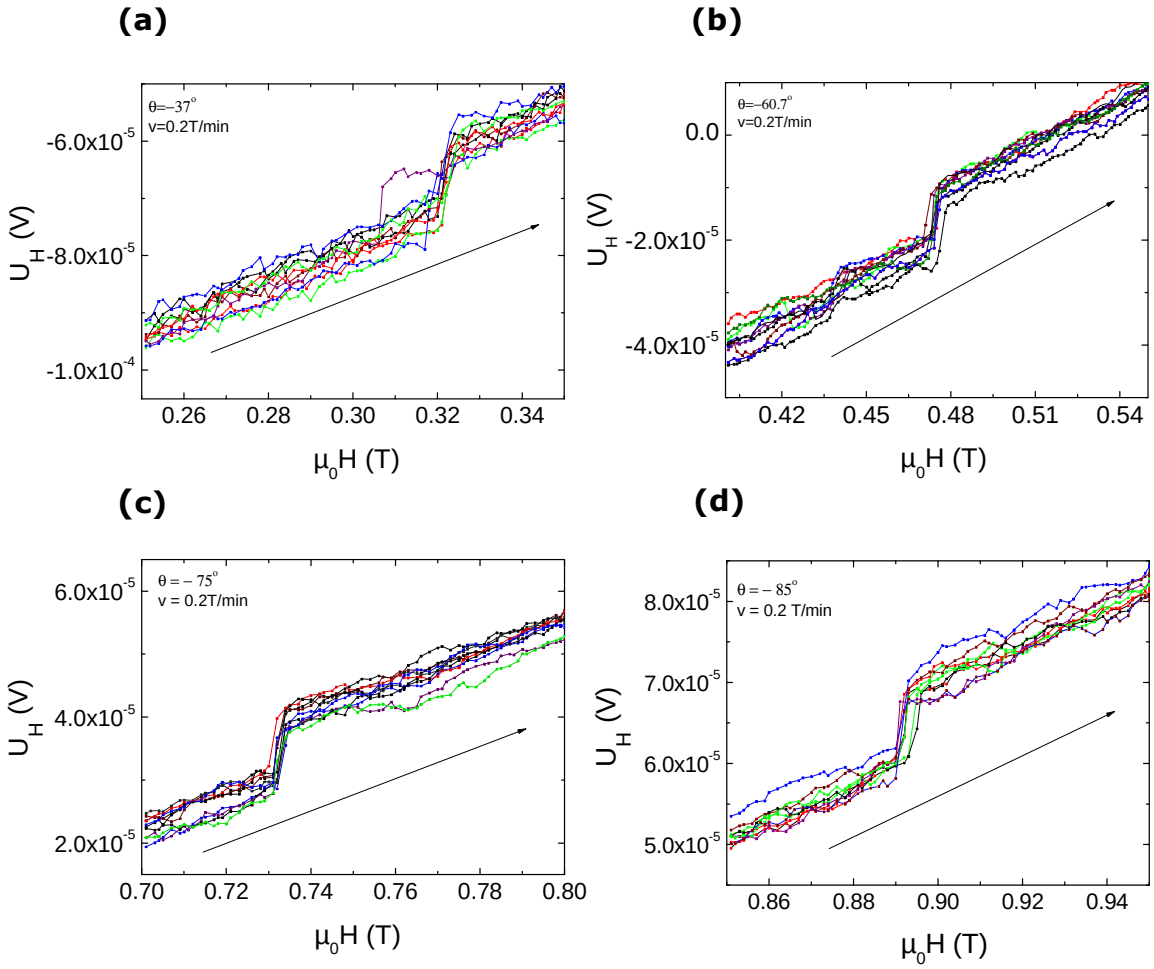

Figure 6.4: *Hall voltage dependence on the external magnetic field. Nucleation events are clearly visible and detected at T = 10 K for different angles θ. There are small deviations in the height of the steps. The relative change of the signal measured by the micro Hall device lies between 7 - 9 μV. This corresponds to the change of the average field in the active area between 5.8 - 7.5 Oe. (a) θ = -37°, $\langle H_n \rangle$ =320 mT, (b) θ = - 61°, $\langle H_n \rangle$ = 473 mT, (c) θ = - 75°, $\langle H_n \rangle$ = 731.5 mT, (d) θ = -85°, $\langle H_n \rangle$ = 891 mT.*

At small angles, the magnetization reversal occurs at $\mu_0\langle H_n\rangle \approx 265$ mT and it depends only moderately on θ. For θ > 45°, however, there is a strong increase of $\langle H_n\rangle$ and very high nucleation fields are observed when θ → 90°. In a nearly rectangular configuration a maximum $\mu_0\langle H_n\rangle$ of 891 mT is found, which is close to the shape anisotropy field ($\mu_0 H_A = 2K_1/M_s$) of about 1.1 T for iron [116].

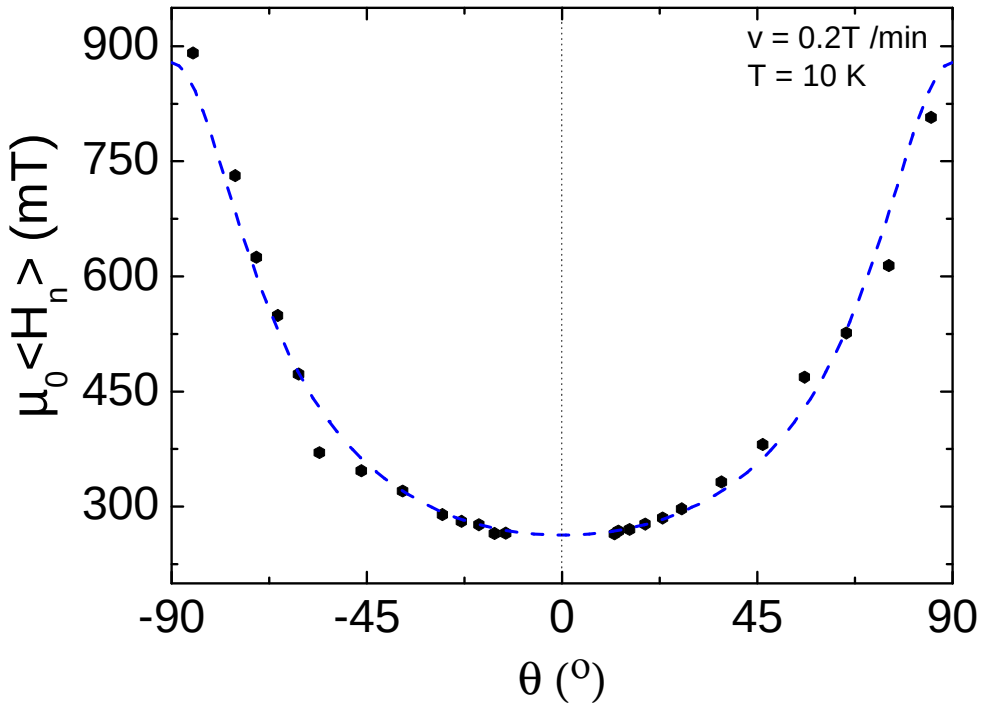

Figure 6.5: *The angular variation of the mean nucleation fields of Fe nanowire. Line: fit according to the curling model (equation 6.1) for an infinite ferromagnetic nanowire length. [110]*

Recalling that imperfections are known to reduce the experimentally observed nucleation fields in real materials, this finding confirms the extraordinary quality of the Fe-nanowire inside the CNT.

The angular dependence of the nucleation field can be interpreted in the frame work of the curling mode for an infinitely long ferromagnetic cylinder:

$$H_n = \frac{M_s}{2} \cdot \frac{a(1+a)}{\sqrt{a^2 + (1+2a)\cos^2\theta}} \qquad (6.1)$$

where, M_s is the saturation magnetization of iron ($\mu_0 M_s$ = 2.2 T at T = 0 K) and a= -1.08$(r_0/r)^2$, $r_0 = (A)^{1/2}/M_s$ is the so-called exchange length and A is the exchange constant. The nanowire radius is referred to r. The fitted curve which nicely agrees to the experimental points is shown by the blue line in figure 6.5. The fitting procedure provided the value a = -0.2301, from which the exchange constant r_0 = 6 nm for iron was derived. This is in a good agreement with the literature value r_0(Fe) = 5.8 nm [117]. The angular dependence of the nucleation fields follows the formula 6.1. for the curling mode reversal of an infinite ferromagnetic nanowire. However, in real systems even for high-quality nanowires the localized magnetization reversal mechanism is favored [118,119]. Following the discussion by Braun [120] one can alternatively explain the nucleation of the magnetization reversal in a cylinder by the creation of a spatially localized nucleus. It can be described as 2π domain wall. This results in finite energy barrier also for infinitely long particles. Another possibility of the magnetization reversal, initiated by the nucleation process was discussed by Knowles [121], who studied magnetization reversal in acicular particles of γ-Fe_2O_3. According to this, the nucleation of small domain with reversed magnetization at the wire end provides even smaller energy barriers. This mode was predicted for nanowires with radii larger than the exchange length. The theoretical studies of magnetization reversal in elongated (5:1 aspect ratio) ferromagnetic particles provide a similar magnetization reversal agreement. Micromagnetic calculations were based on the Landau-Lifshitz equation [122,123] and was performed by Boerner and Bertram. They found that the thermally assisted, field - dependent reversal is initiated at the particle ends, which suggests that thermal effective volumes are significantly smaller than particle volumes [124].

The process of magnetization reversal hence is governed by nucleation of a domain with reversed magnetization and the corresponding domain wall rapidly moves through the nanowire after its formation, while nucleation fields follow the curling mode. Further experimental evidence for nucleation scenario is provided by the hysteresis loops at small angles $|\theta| \leq 37°$ (see Fig. 6.3 c-d).

Here, the hysteresis loops reproducibly exhibit additional small jumps attributed to depinning of the domain wall during the magnetization reversal process.

6.1.4. Temperature dependence of the nucleation fields

Another experimental evidence of such a nucleation process in magnetization reversal can be obtained by the observation of the temperature dependence of the mean nucleation field, which allows calculating the effective volume for the nucleation. The temperature dependence of the nucleation field is shown in figure 6.6.

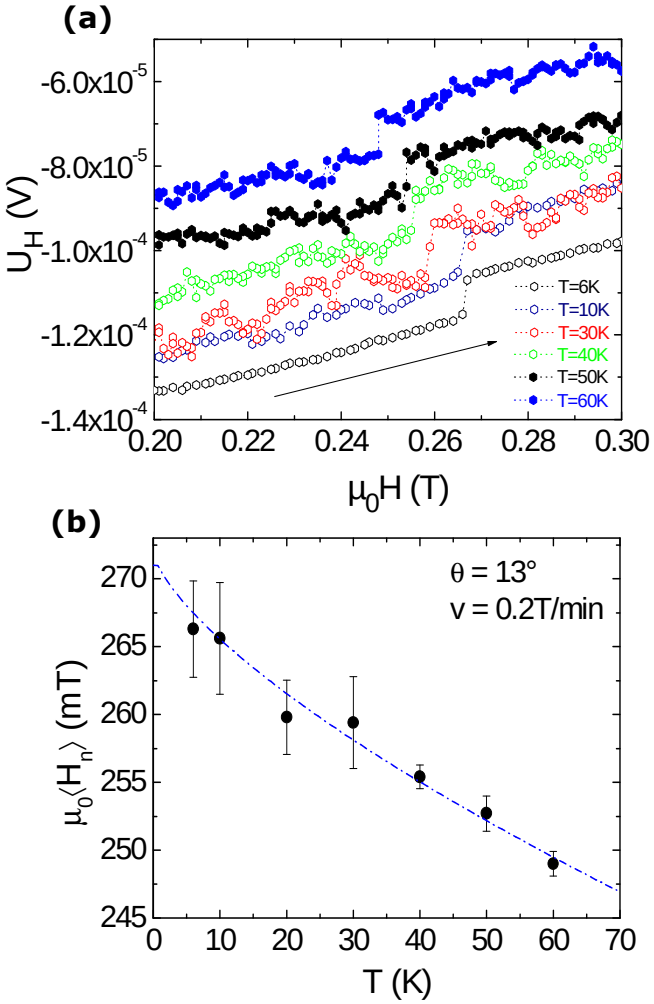

Figure 6.6: (a) *Nucleation events for different temperatures. The noise increases at higher temperatures, but the nucleation in the Fe-filled CNT is still detectable at temperatures as high as 60 K. (b) Temperature variation of the mean nucleation field of the Fe nanowire. Error bars correspond to the standard deviation of H_n. Dotted line is the fit given by the equation 6.2. [110]*

The temperature dependence of the nucleation field experiments were performed at the angle $\theta = 13^o$ and the temperature was varied from 6 to as high as 60 K, where the nucleation was still detectable (cf. fig 6.8a). The detection of the nucleation process was performed in two steps as follows. Firstly the magnetic field was ramped to the negative value of -1 T with a sweeping rate of v = 0.5 T/min to reverse nanowire magnetization. Subsequently, the magnetic field was swept back to the zero and set to the value 0.2 T. The actual measurements of the nucleation were performed at the sweeping rate 0.2 T/min in the magnetic field range between 0.2 - 0.3 T, at which the nucleation acts were

detected and stored. For each temperature we performed a set of at least 120 nucleation experiments in order to provide histograms of the nucleation fields. The mean value of the nucleation fields (circles) and the corresponding standard deviations (bars) were then calculated for each temperature and are shown in figure 6.6b. We observed a strong dependence of the mean nucleation field on the temperature range of measurements. The mean nucleation field decreases with increasing temperature. This behavior is expected in a thermally activated process. In the process the average nucleation field should follow the formula [125,126]:

$$< H_n >= H_0 \left(1 - \left(\frac{k_B T}{E_0} \ln(cT/v) \right)^{\frac{2}{3}} \right) \tag{6.2}$$

where H^0 is the nucleation field at temperature T = 0 K, k_B is the Boltzmann constant, E_0 is the energy barrier in absence of an external magnetic field, v = 3.3 mT/s wis the sweeping field rate, $c = k_B H^0/(\tau_0 E_0)$, $\tau_0 = 1.2 \cdot 10^{-10}$ s [109] is the prefactor of the thermal activation rate $\tau = \tau_0 \exp(E/k_B T)$ and $E = E_0 \cdot (1-H/H_0)^{3/2}$ is the energy barrier dependence on the external magnetic field. Experimental points are in agreement with formula 6.2. Fitting the experimental data by means of Eq. 6.2 yields $E_0/k_B = 5.18 \cdot 10^4$ K and $\mu_0 H^0 = 272$ mT. Interestingly, the activation volume $V = E_0/(\mu_0 M_s H_n)$ derived from E_0 only amounts to $V = 1.5 \cdot 10^3$ nm^3 which is much smaller than the volume of the nanowire ($\approx 8 \cdot 10^6$ nm^3). This is again consistent with the assumption of domain nucleation at one end of the nanowire. While our experimental data on the angle dependence of $\langle H_n \rangle$ indicate the evolution of curling modes, there is compelling additional evidence of localized magnetization reversal via domain wall formation and propagation. The latter observation is consistent with the conjecture that any arbitrarily small disorder gives rise to localization and shows that the actual degree of localization is strongly dependent on the structure of the nanowire [127].

6.1.5. Nucleation field distribution

In a thermally activated process of magnetization reversal the nucleation field does not have a unique character but is characterized by the width of the distribution σ_H around the average value $<H_n>$. Thus we measured histograms of nucleation fields as described

above (shown in Fig. 6.7) for different temperatures. The temperature dependence of the distribution of the nucleation field is given model developed by Kurkijärvi [110],[128]:

$$\sigma = H_0 \frac{1}{\alpha}\left(\frac{k_B T}{E_0}\right)^{\frac{1}{\alpha}}\left(\ln\left(\frac{cT}{\nu\varepsilon^{\alpha-1}}\right)\right)^{(1-\alpha)/\alpha} \tag{6.3}$$

where H_0 is the nucleation field at temperature T = 0 K, k_B is the Boltzmann constant, E_0 is the energy barrier in absence of external magnetic field, v is the sweeping field rate, $c = k_B H^0/(\tau_0 E_0)$, τ_0 is the prefactor of the thermal activation rate, $\tau = \tau_0 \exp(E/k_B T)$ where $E = E_0(1-H/H_0)^{3/2}$ is the energy barrier dependence on the external magnetic field, $\alpha = 2/3$.

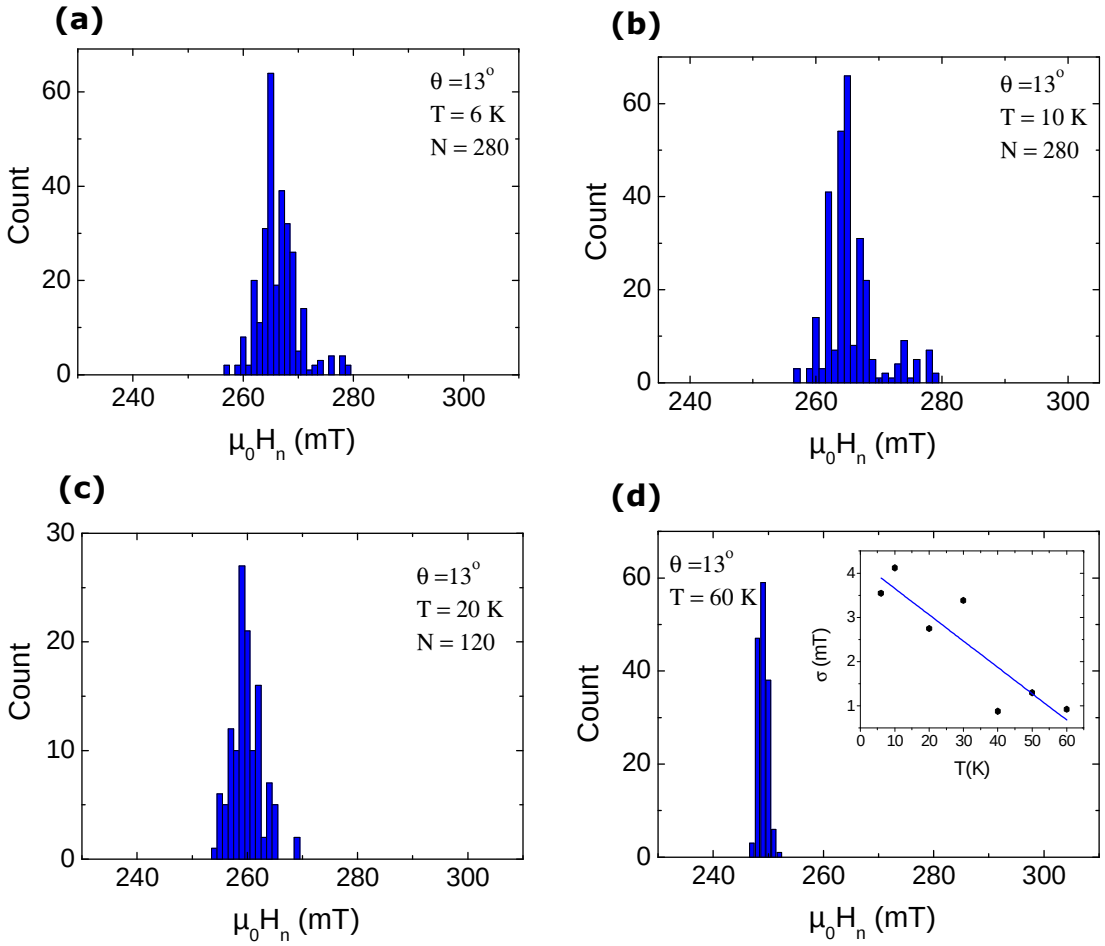

Figure 6.7: *Histograms of the nucleation field distributions measured at the angle θ = 13° and at different temperatures. (a) Histogram measured at the temperature T=6K, N = 280, $\langle H_n \rangle$ = 266.3 mT, σ_H = 3.5 mT, (b) T = 10 K, N = 280, $\langle H_n \rangle$ = 265.6 mT, σ_H = 4.1 mT, (c) T = 20 K, N = 120, $\langle H_n \rangle$ = 260 mT, σ_H = 2.7 mT, (d) T = 60 K, N = 150, $\langle H_n \rangle$ = 249mT, σ_H = 0.9 mT. Inset: Variation of the standard deviation σ_H with temperature. Blue line represents a guide for the eye. [110]*

In the model the distribution of the nucleation field increases with increasing of the temperature.

Surprisingly we observed the opposite case in our experiments, i.e. the distribution of the nucleation fields at low temperatures ($\sigma_H/<H_n>$ = 1.3 %, T=6K) is significantly higher than that measured at high temperatures ($\sigma_H/<H_n>$ = 0.36 %, T=60K). The variation of the distribution of nucleation fields with temperature has a monotonic character and it is shown in inset of figure 6.7d. The detailed study of the distribution of nucleation fields and its temperature dependence is presented in figure 6.7.

At low temperatures ($T \leq 10$ K), the distribution of nucleation fields for the fixed set-up splits into (at least) two well separated parts while no splitting occurs at higher temperatures ($T \geq 20$ K). The splitting is associated with a relatively large nucleation field distribution which at low temperatures amounts to around 2% of the average nucleation field value. The splitting in the histograms and the corresponding broad distribution of nucleation fields can again be associated with domain nucleation. To be specific, the observed splitting indicates at least two nucleation sites which are characterized by different energy barriers of nucleation and which become distinctive at low temperatures. For large diameter wires as this example $d/d_0 > 2$ several different sites compete for the nucleation but with nucleation fields following the curling mode.

The analogous behavior has been already reported by *Wernsdorfer et al.*[129] in Ni nanowires with a similar geometrical ratio $d/d_0 > 2$ and at low temperatures. The measurements of the distribution of nucleation fields presented in that work were performed with higher magnetic field resolution. Our experimental setup with a field resolution of 1 mT possibly hides the detailed structure of the distribution

6.1.6. Summary and discussion

In conclusion, we investigated the magnetic properties (nucleation fields, their distribution and temperature and angular dependence) of high quality, straight Fe nanowire d = 26 nm embedded inside the carbon nanotube. The hysteresis loops of the Fe-filled CNT exhibits square like behavior which reveals a single domain magnetic behavior of the nanowire. The exception from this is nucleation at angles between the wire axis and external magnetic field $\theta \leq 37^o$, where tiny additional steps appear in the hysteresis loops. This behavior is related to the pinning of the domain wall during the magnetization reversal process, where due to the pinning an additional magnetic field has

to be applied to complete the switching. We observed that the angular dependence of the nucleation field is in good agreement with the curling model for infinitive ferromagnetic nanowires. However, the observation of additional magnetization steps at small angles, the distribution of the nucleation field and our analysis of the observed temperature dependence provide good experimental evidence that magnetization reversal is associated with domain nucleation, supporting a scenario where domain formation is initiated by curling. At angles θ close to 90° we detect extraordinairly high nucleation fields (up to 900 mT) near the theoretical limit i.e. shape anisotropy field of iron.

6.2. Micro Hall studies on a bent iron nanowire

6.2.1. Experimental details

A Fe-filled CNT with a Fe nanowire in the core of length L ≈ 900 nm and diameter d ≈ 16 nm was placed on to the 0.8 × 0.8 μm^2 active area (Fig. 6.8 a-b).

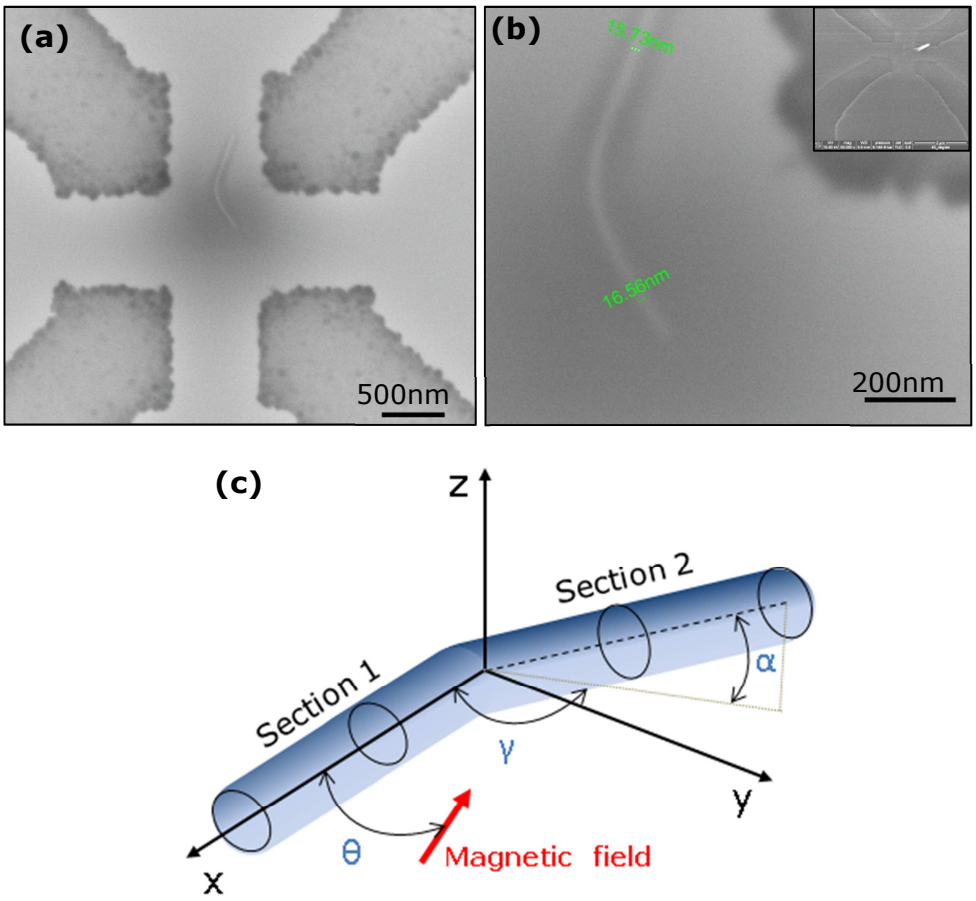

Figure 6.8: *(a) SEM BSE picture of the Fe-filled CNT placed onto the 0.8 × 0.8 μm^2 Hall sensor fabricated with the same GaAs/AlGaAs heterostructure as in the previous example, (b) high magnification SEM BSE image of the nanotube. The diameter of the nanowire lies between 16 and 17 nm. Inset: SEM picture made with plane tilt of 45°, (c) the sketch presents the situation of the nanowire in 3D space. θ is the angle between the axis of the laying part of the nanowire (section 1) and external magnetic field, γ = 130.5° describes the angle between section 1 and the projection of section 2 on the xy plane, α =43° is the angle between section 2 of the nanowire and its projection on the xy plane.*

One of the ends of the nanotube was placed almost at the center of the active area of the device. During the manipulation procedure the nanowire was bent and formed a banana-like shape. Careful investigations under SEM with tilting the plane of the device showed that the part of nanotube which is located outside of the active area (section 2) is standing up with an angle $\alpha = 43^o$ with respect to the surface, whereas section 1 of the nanowire is lying entirely on the surface. The micro Hall experiments were performed with the magnetic field applied in plane of the device. The sketch showing the nanotube in the space is presented in figure 6.8c. θ defines the angle between the external magnetic field and the axis of the section 1 of the nanowire. The angle between the axis of section 1 of the nanowire and projection of section 2 onto the surface is $\gamma=130.5^o$. The angle between both arms of the nanowire (not shown in the sketch) equals 121^o. The kinked shape causes some inhomogeneities of the magnetization orientation at the kink or under certain circumstances even the existence of a domain wall (as shown by additional MFM experiment performed at other Fe-filled CNT, see Fig. 6.15c), which separates two sections of the nanowire (section 1 and section 2) with magnetizations pointing to the kink area.

6.2.2. Hysteresis loop measurements

The hysteresis loops measured at different angles ($\theta = 2^o$, $\theta = -31^o$, $\theta = -58^o$) and in magnetic fields up to 0.5 T are shown in figures 6.9 a-c. The overall shape of the curves is similar to the one observed in the straight nanowire (cf. Fig. 6.3. a-b). The main features are sharp jumps of $<B_z>$, which are symmetric with respect to zero magnetic field. These singular jumps at $H_{exterrnal}= H_n$ (nucleation fields) are associated with the nucleation process in the iron nanowire. We transferred the Hall voltage signal to the stray field and observed that in the remanent state the average z-component of stray field equals ≈ 4 Oe which is lower than in the straight nanowire (≈ 7 Oe). The reason for this is probably that the diameter of the nanowire (≈ 16 nm) is smaller than that of the previous nanowire (≈ 26 nm). However, hysteresis loops measured for angles $30^o \leq\theta \leq 50^o$ show a strong asymmetry towards the positive magnetic fields. This is illustrated in figure 6.3 d. The hysteresis loop was measured for $\theta = 30^o$ with magnetic fields up to 0.5 T. The measured nucleation fields amount to $H_n= 309$ mT and $H_n= 331$ mT, in the negative and positive

field range, respectively. A hypothesis explaining the biasing effect is provided in section 6.2.5.

As mentioned in section 6.1, Micro Hall magnetometry is a local technique probing changes of the stray magnetic field at one end of the nanowire. In the case of the straight Fe-filled CNT we could attribute the measured hysteresis loops as a characteristic of the entire nanowire, based on previous MFM studies [55] which showed that the remanent state of straight nanowires is always single domain.

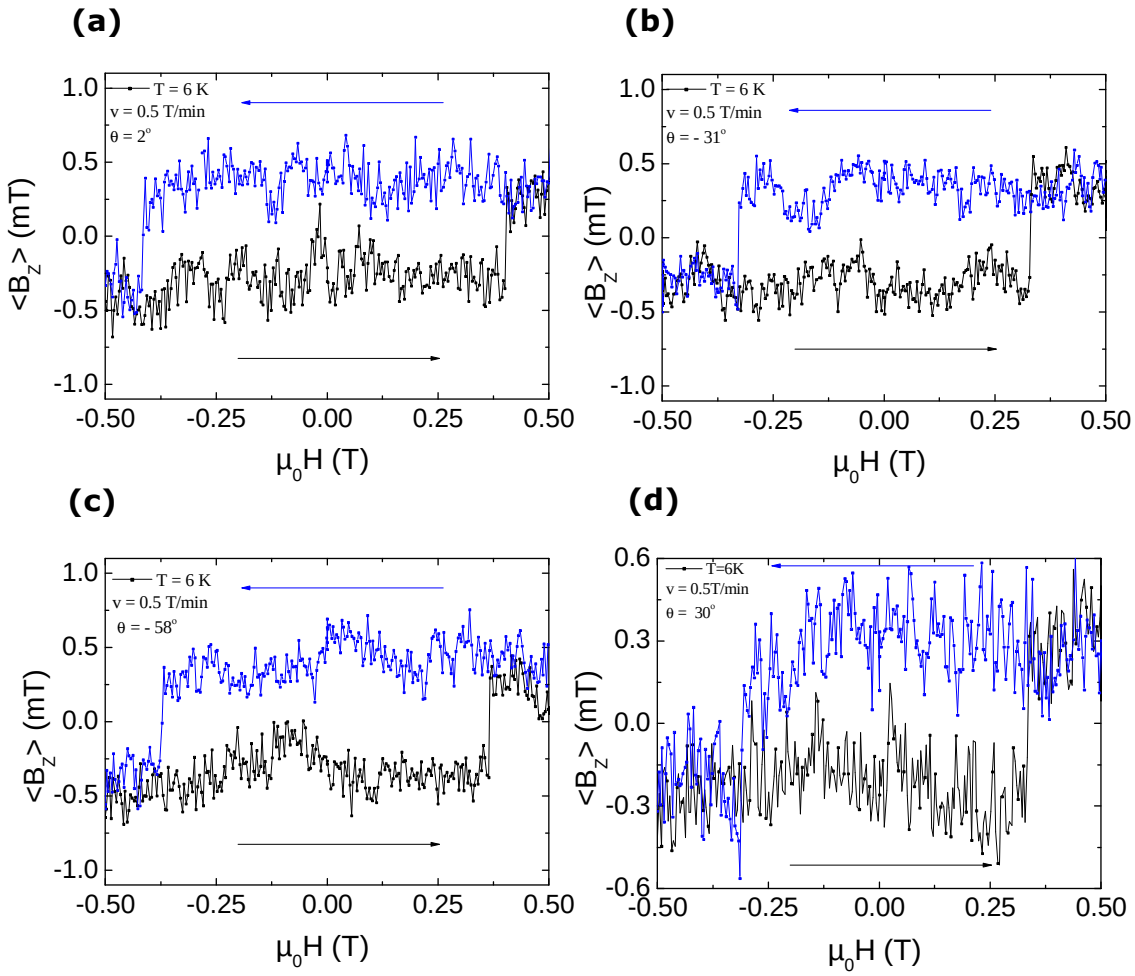

Figure 6.9: *Hysteresis loops of the Fe-filled CNT measured at T = 6 K for different angles after subtraction of the linear background coming from the z - component of external magnetic field. (a) θ = 2°, $\mu_0 H_n$ =417 mT, (b) θ = -31°, $\mu_0 H_n$ = 328 mT, (c) θ= -58°, $\mu_0 H_n$ =370 mT, (d) θ= 30°, $\mu_0 H_n$=309 mT and $\mu_0 H_n$=331mT in negative and positive magnetic field range, respectively.(measured by Dr. S. Bahr)*

MFM experiments (see Fig. 6.15) performed on the bent Fe-CNT show that the crooked area forms a pinning center in which a domain wall might be confined during the

magnetization reversal process. Since the bent part of the nanowire is at the edge of the active area of the Hall cross, the sensor does not detect the pinning of the domain wall (cf. Fig. 6.8 b). However in section 6.2.5 experimental evidence is provided which supports hypothesis that the symmetric hysteresis loops (Fig. 6.9 a-c) can be attributed to the switching of the entire nanowire, whereas asymmetric hysteresis loops to switching of section 1 only (c.f. Fig. 6.9 d).

6.2.3. Temperature dependence of the nucleation fields

The temperature depending study of the nucleation fields was performed at temperatures ranging of 6 – 70 K as shown in figure 6.10 a-b. The measurements were performed for an angle of $\theta = -36^{o}$. Similarly as for the straight nanowire presented in subchapter 6.1 we observed a strong decrease of the mean nucleation field with increasing the temperature. The results of the experiments are summarized in figures 6.10 a and b. The fitting of experimental points with formula 6.2 (v = 1.67 mT/s, $\tau_0 = 1.2 \cdot 10^{-10}$ s) provides a nucleation field at T = 0 K of H_0 = 324 mT and the energy barrier height $E_0/k_B = 1.3 \cdot 10^5$ K. Assuming that the energy of the domain with reversed magnetization is only due to the Zeeman energy, the activation volume $V = E_0/(\mu_0 M_s H_n)$ derived from E_0 only amounts to $V = 3.16 \cdot 10^3$ nm^3 which is much smaller than the volume of the nanowire ($\approx 2 \cdot 10^5$ nm3). This again suggests that the reversal of the magnetization is caused by a nucleation of a reversed fraction of the cylinder surrounded by a domain wall which rapidly propagates along the whole nanowire, similarly as in the previous Fe-filled CNT. The study of the nucleation field distribution at temperatures T = 6K and T = 20K is shown in figure 6.10 c-d. The distribution of nucleation fields is rather broad, i.e. for the distribution of the nucleation fields at T = 6K, we find $\sigma_H/\langle H_n \rangle$ = 1.5 %, whereas at the distribution amounts to T = 20K $\sigma_H/\langle H_n \rangle$ = 1.95 %. This broad distribution suggests that again there are several nucleation sites. This width of thedistribution increases with temperature (see inset of figure 6.10 d). The measured values are: T = 6K $\sigma_H/\langle H_n \rangle$ = 1.5 %, T = 10K $\sigma_H/\langle H_n \rangle$ = 1.68 %, T = 20K $\sigma_H/\langle H_n \rangle$ = 1.95 %, T = 70K $\sigma_H/\langle H_n \rangle$ = 1.91 %.

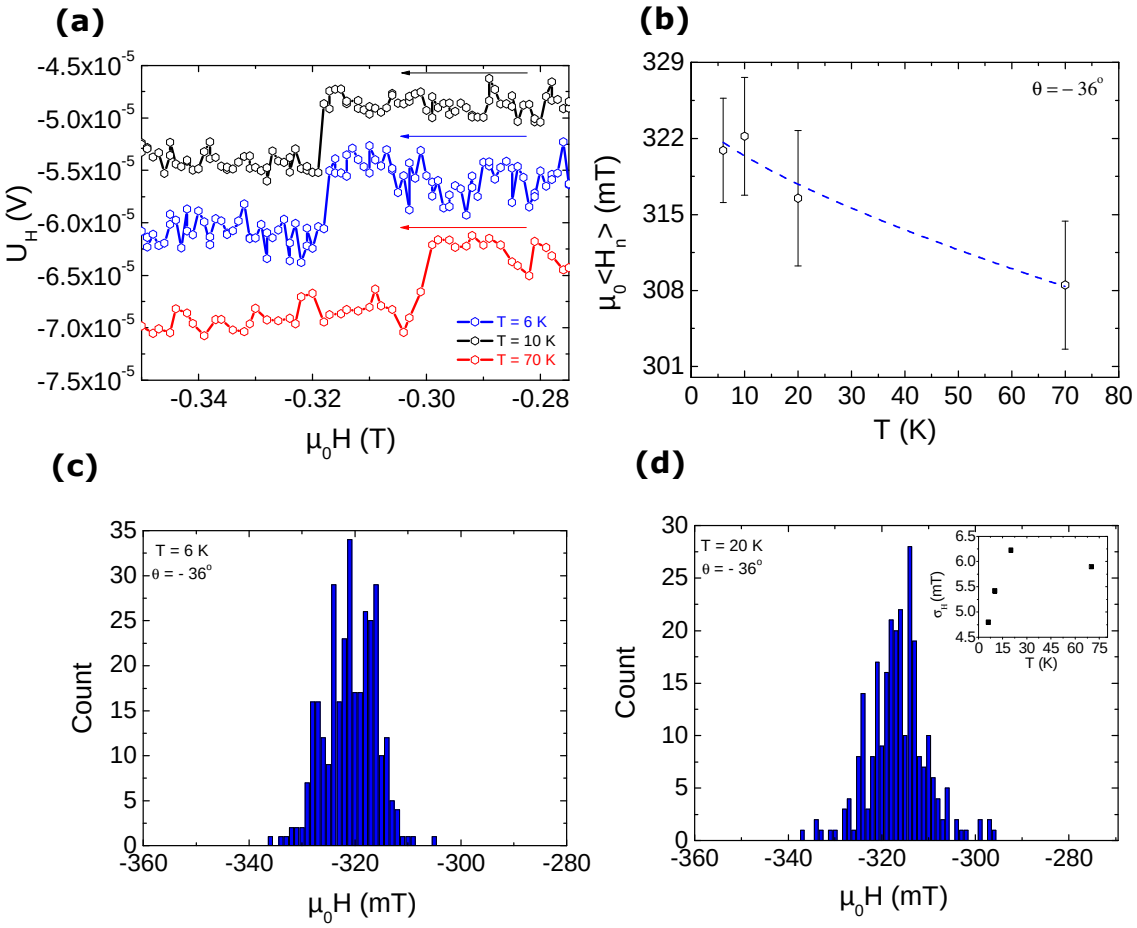

Figure 6.10: *(a) The nucleation events detected at temperatures T = 6 K, 10 K and 70 K and with θ = - 36° and ν = 0.2 T/min. Even at temperatures as high as 70K the nucleation process in the nanomagnet is still detectable, (b) the temperature variation of the mean nucleation field of the bent nanowire. Bars correspond to standard deviation of the nucleation field. Fitting parameters: E_0/k_B = 1.3·10^5 K, $\mu_0 H_0$ = 324 mT. (c) Histogram of the nucleation fields measured at T = 6 K, θ = -36°, N =320 , σ_H = 4.8 mT, (d) histogram of the nucleation fields measured at T = 20 K, θ = -36°, N = 280, σ_H= 6.2 mT. (measured by Dr. S. Bahr)*

6.2.4. Angular dependence of the nucleation fields

The angular dependence of the nucleation fields of the Fe-filled CNT is shown in figure 6.11. For each angle θ we measured the hysteresis loop (with magnetic field rate 0.5 T/min) up to maximum absolute field value of 0.5 T. The symmetric values of the nucleation field with respect to the zero external magnetic field are shown by black circles. However, as mentioned previously, in the positive angular range, i.e. for angles 30°, 40°, and 50°, we observed a biasing of the hysteresis loops towards the positive field

values. The nucleation fields measured at positive magnetic fields are marked by blue circles, whereas those measured in negative fields range are marked by red circles. Each of the measured hysteresis loops presents similar square shape as it is shown in figure 6.9. The nucleation fields observed for this nanowire equal -426 mT, 408 mT, and 416 mT, for the angles $\theta = -90^o$, $\theta = 0^o$, $\theta = 90^o$ respectively. At the angle -45^o, we observed the nucleation at field 327 mT. The overall behavior of the nucleation fields suggests that the nanowire reverses via the rotation in the unison as predicted by the Stoner – Wohlfarth model in which the periodicity of H_n equals $\pi/2$ (Fig. 2.8):

$$H_n = \frac{H_A}{(\cos^{2/3}\theta + \sin^{2/3}\theta)^{3/2}} \tag{6.4}$$

However, we find that the nucleation fields are strongly suppressed in comparison to the nucleation fields of the Fe nanowire which is presented in the previous chapter (see Fig. 6.5). In this case, the maximum value of the nucleation field is around 50 % of the maximum nucleation field of the nanowire with d = 26 nm. Moreover, the measured values of the nucleation fields are systematically smaller than the predictions of the model of coherent rotation of magnetization reversal.

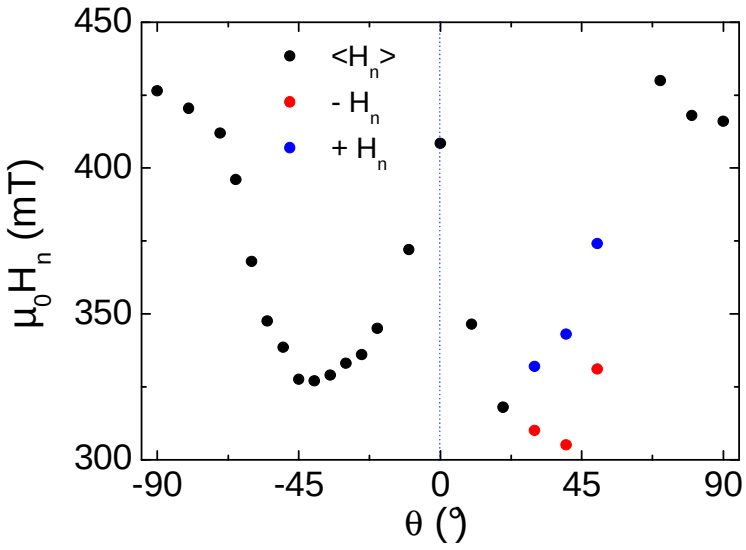

Figure 6.11: *Angular dependence of the nucleation field measured at T = 6 K. Black circles represent the nucleation fields derived from symmetric hysteresis loops. The red and blue points represent the switching in negative and positive fields in case of asymmetric hysteresis loops. (measured by Dr. S. Bahr)*

A similar behavior of coherent like magnetization reversal with suppressed switching fields is found by theoretical calculations performed by Richter [130].
In this paper, the calculations of the angular dependence of the switching fields for infinitive ferromagnetic particles with structural defects are presented. Indeed, in this example it is shown that structural defects have a significant influence and reduce the range of H_{sw}. The calculations were based on the minimization of the free energy of particles with defects. The following parameters T and α were used for these calculations:

$$T = \sqrt{\frac{K_1 d^2}{A}} \quad \alpha = \frac{M_{Sd} A}{M_S A_d} \tag{6.5}$$

Here K_1 is the magnetocrystalline anisotropy constant, d is the length of the defect area, A is the exchange constant. M_{Sd} and A_d are the saturation magnetization and exchange constant within the defect region respectively. The angular dependence of the switching fields for different parameters T and α is shown in figure 6.12.

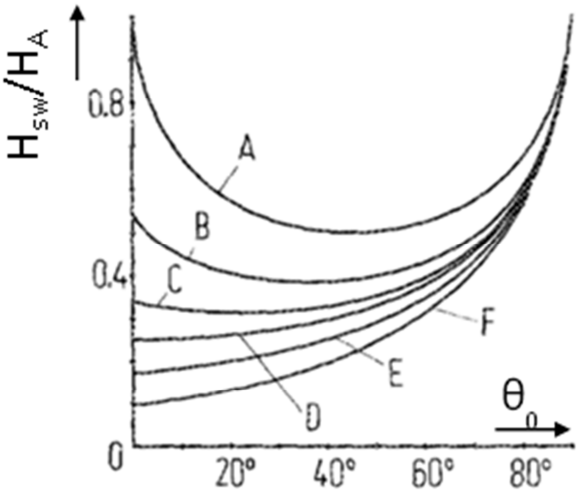

Figure 6.12: *The dependence of the reduced switching fields H_{sw}/H_A as a function of angle θ_0 between the easy axis of the nanoparticles and the applied external magnetic field obtained in calculations. Parameters used in the calculations: T – normalized defect size width and factor α. (A) Stoner-Wohlfarth model, (B) T = 1, α = 1, (C) T = 2, α = 1, (D) T = 10, α = 1, (E) T = 10, α = 2, (F) T = 10, α = 5* (taken from [126]).

The source of the defects in the nanowire studied here might be:

- crystal structure distortions (e.g. inside the bent part)
- misalignment between neighboring crystal like domains

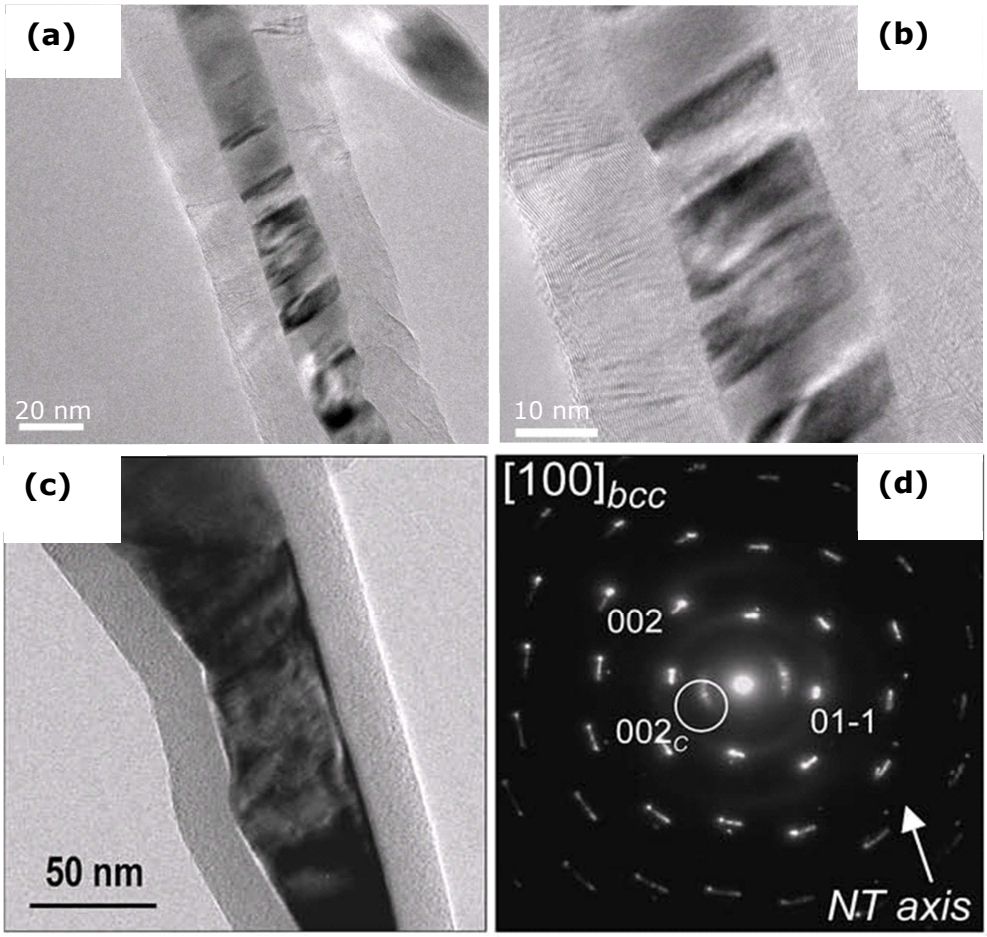

Figure 6.13: *(a) TEM image of Fe-filled carbon nanotube with poor quality filling, (b) high magnification TEM picture of Fe-filled CNT, carbon shells are well developed, white and black areas possibly correspond to different crystalline orientations, (c) TEM image of bcc Fe-filled CNT [131], (d) corresponding selected-area electron diffraction pattern. The (002) spots correspond to the grapheme sheets surrounding Fe-filling [131]. (images a and b made by Dr. Thomas).*

In several cases the crystalline structure is not so perfect as shown in figure 4.10 c-d. A further example is shown in figure 6.13. Figure 6.13 (a-b) shows a Fe-filled CNT with lighter and darker contrast along the filling. These patterns in contrast correspond to crystalline distortions (stacking folds), whereas as in other samples, as shown in figure 6.13 (c-d) misaligned neighbouring crystal domains are present. The corresponding diffraction pattern (Fig. 6.13 d), shows the diffraction spots are no longer points but are rather stretched [127]. The above explanations based on the model developed by Richter are not the only which ascribe suppression of the switching fields as the results of defects. The numerical calculations on nanowires and nanoparticles were also presented by the

other authors. *Uesaka et al.* showed by solving the Landau – Lifshitz – Gilbert equation [122,123] for fine hexagonal platelet particles [132] the influence of three different types of defects on the switching field. They considered surface defects as well as volume defects and showed that the difference between the switching fields for particles with and without defects amounts to at most 12 %. In [133] for instance *Gadbois et al.* used micromagnetic simulations to investigated the effect of edge roughness on the switching fields in Ni bars of size 1 µm in length, 30 nm depth and 40 – 400 nm in width. The conclusion of this study was that the roughness along the edges significantly reduces the switching fields. They described the magnetization reversal mechanism as a nucleation of a domain with reversed magnetization from the rough edges whereas in the absence of roughness nucleation processes takes place at one end of the sample but in higher external magnetic fields.

6.2.5. Biasing of the hysteresis loops

By performing the magnetic hysteresis loop measurements at the angles $\theta \geq 30^o$ and $\theta \leq 50^o$ (c.f. Fig. 6.11) we observed very large asymmetry in the nucleation fields. These values were $H^-_n = 309$ mT and $H^+_n = 331$ mT for 30^o, $H^-_n = 304$ mT and $H^+_n = 342$ mT for 40^o and $H^-_n = 330$ mT and $H^+_n = 373$ mT for angle 50^o. Hysteresis loops were measured in the maximum magnetic field range of up to 0.5 T. In this subchapter we will discuss by showing MFM images and switching experiments that it is possible under certain circumstances to pin a domain wall inside the bent area of the nanowire by reversing the magnetization of one of its arms. While the magnetization reversal is a localized mechanism and takes place via nucleation (activation volume is smaller than the volume of the nanowire see subchapter 6.2.3), the bent part of the nanowire forms a pinning center. The initial single domain state is then replaced by a two magnetic domain configuration. We described the observed biasing of the minor hysteresis loops measured for the given angular configuration as an influence of section 2 of the nanowire on section 1 via stray field and exchange interactions between both sections.

Because one part of the nanotube is pointing up with the angle $\alpha \approx 43^o$ with respect to the surface, we could not perform detailed MFM studies on the pinnining of the domain wall in the kinked area for the given nanowire. Thus, we will present the results of MFM experiments performed on a Fe-filled CNT entirely laying on the surface. In order to obtain the individual Fe-filled CNT an ensemble consisting of nanowires was diluted in

the acetone and tip sonification was applied to prepare a homogeneous dispersion. Then a drop of this solution was put onto Si substrate and dried. SEM was used to select the suitable individual Fe-filled CNT shown in figure 6.14a. The diameter of the nanowire was d ≈ 32 nm.

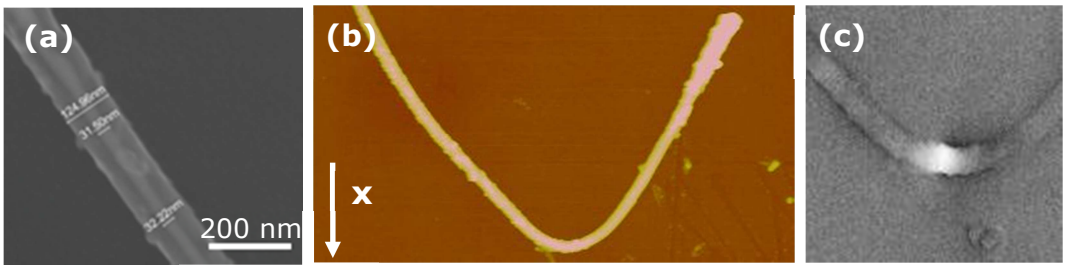

Figure 6.14: *(a) High resolution SEM image of a Fe-filled CNT (d ≈ 32 nm) used in the MFM experiment, (b) AFM topography image of the reshaped Fe-filled CNT laying on the surface, (c) Corresponding MFM scan of the bent area. The picture presents the remanent state of the iron nanowire inside the carbon nanotube after application of the external magnetic field $\mu_0 H$ = 400 mT in the x direction. The contrast reveals the formation of a domain wall separating two magnetic domains with magnetic moments pointing to each other* [10].

The sample was then placed in a chamber of AFM/MFM setup and the initial single domain state was determined by the MFM imaging. With aid of the AFM cantilever the nanotube was reshaped as it is shown in figure 6.14b and an external magnetic field 400 mT was applied in the plane in x direction. The MFM scan shown in figure 6.14c was performed on such a prepared nanomagnet and in absence of external magnetic field. In the flexure of the nanowire we observed a bright contrast. The MFM ferromagnetic tip operates in non-contact mode and it is probing the phase shift of the cantilever induced by the stray field of the magnetic sample. Thus MFM provides an image of the spatial variation of the magnetic stray field on the sample surface. We conclude that the bright contrast in the MFM picture is provided by inhomogeneities of the stray field caused by the existence of a domain wall. The applied external magnetic field (400 mT) induced the switching of one part of the nanomagnet (c.f. Fig. 6.14c). The experiment reveals that both arms of the nanowire can switch independently. After the application of an external magnetic field the nanowire consists of two magnetic domains (after the initial single domain configuration) separated by a head to head domain wall in the remanent state.
Now we will discuss, by presenting the switching experiments performed on the Fe-filled CNT shown in figure 6.8, that the biasing of the hysteresis loops which we observed for

[10] The experiment was performed by Franziska Wolny and Thomas Mühl from IFW Dresden.

angles $30^o \leq \theta \leq 50^o$ while performing the angular dependence experiments might be related to the influence of section 2 of the nanomagnet on the switching of section 1. Such interaction might be due to magnetostatic and exchange interactions between both nanowire sections.

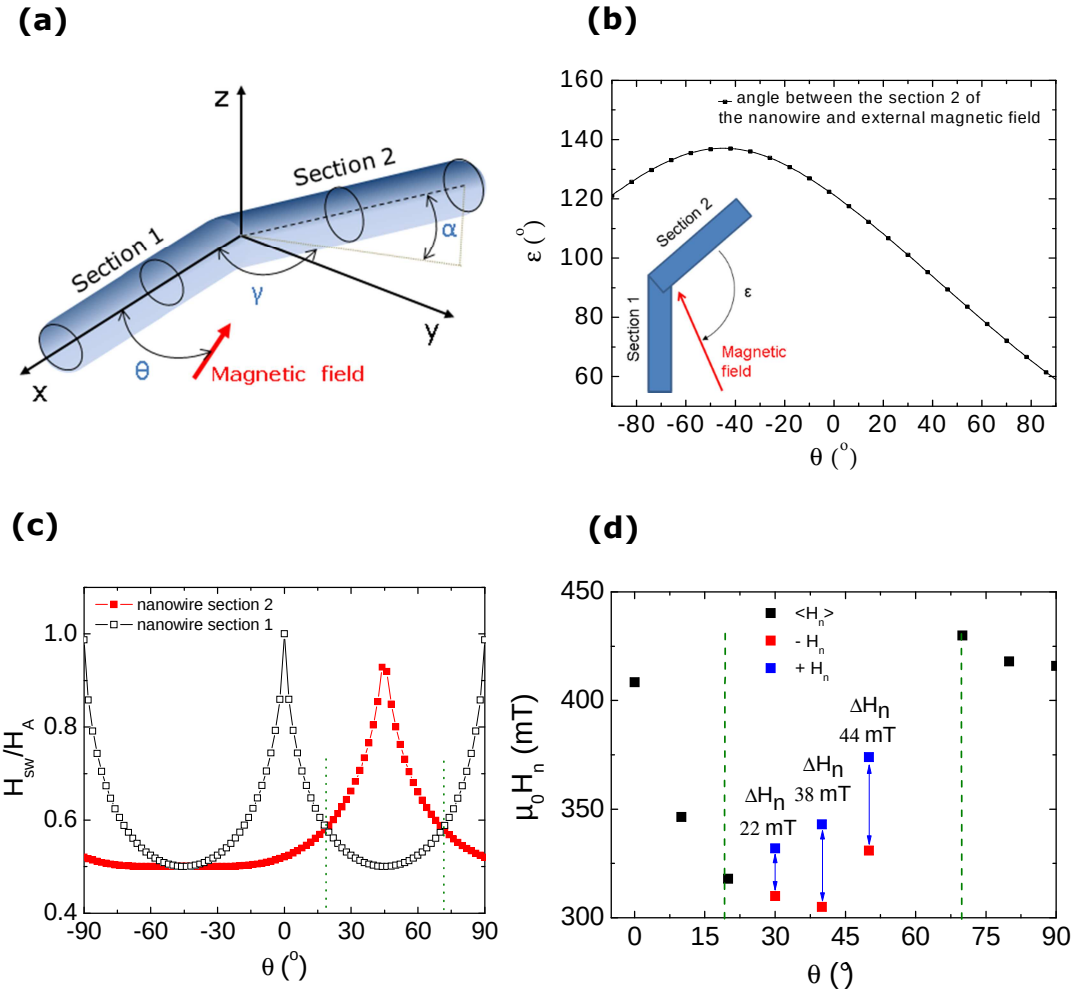

Figure 6.15: (a) *The sketch presents the situation of the nanowire in the 3D space. θ is the angle between the axis of the laying part of the nanowire and the external magnetic field, γ = 130.5° describes the angle between section 1 and the projection of section 2 on the xy plane, α = 43° is the angle between section 2 of the nanowire and its projection on the xy plane, (b) ε is the effective angle between section 2 of the nanowire and the external magnetic field as a function of the angle θ. The inset shows the sketch of the nanowire and the manner in which the angle ε is measured, (c) angular dependence of the switching fields (coherent rotation) calculated for section 1 and section 2 independently as a function of the angle θ according to Stoner-Wohlfath model, (d) experimental points, red squares represent nucleation fields measured at negative fields whereas blue squares represent nucleation fields measured at positive fields. Black squares are associated with nucleation processes in which the biasing of the hysteresis loops was not observed.*

Figure 6.15a illustrates sketches the geometry of the investigated Fe-filled CNT. An external magnetic field is applied in the x-y plane with angle θ measured from x to y axis. Using trigonometric formulas we can calculate the effective angle ε between the external magnetic field and the section 2 of the nanowire as a function of θ (Fig. 6.15b). Since we observed the suppression of the nucleation fields (possibly related to the defects of the nanowire, see subchapter 6.2.5) we assume that the switching field of section 2 is suppressed in the same rate. This allows us to calculate the angular dependence of switching fields for each section of the nanowire independently using the formula 6.4. The solutions ($Hsw_1(\theta)$ and $Hsw_2(\theta)$) are shown in figure 6.15c. The figure reveals that the expected switching field of Section 1 is larger than the switching field of section 2 for $-90^o \leq \theta \leq 18^o$ and $71^o \leq \theta \leq 90^o$, whereas it is smaller in the range $18^o < \theta < 71^o$. Such a situation is indeed found in our micro Hall experiments at $\theta = 30^o$ where asymmetric switching fields are measured. Based on previous MFM studies performed on a different bent Fe-filled CNT we hence assume a similar situation where. during the magnetization reversal process a domain wall might be pinned in the kinked part of the nanowire (Note that in micro Hall experiments the magnetic field is applied between both sections of the Fe-filled CNT with $\theta = 30^o$ and $\varepsilon \approx 101^o$, cf. Fig. 6.15b).

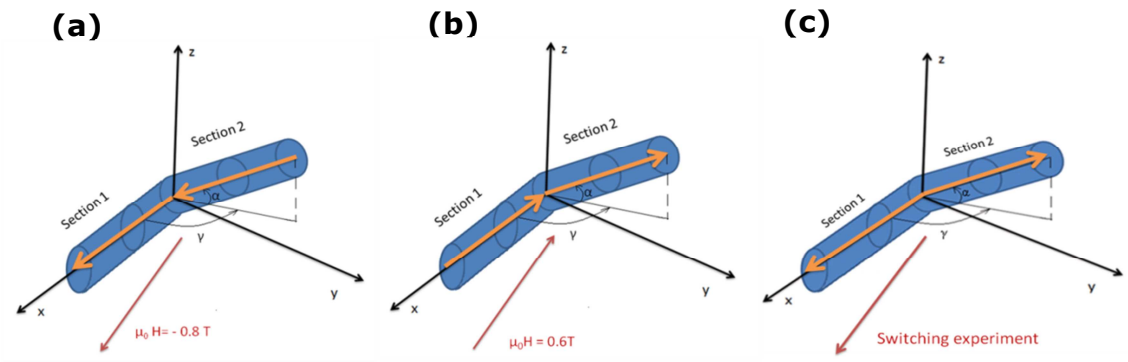

Figure 6.16: *Scenario of magnetic switching of section 1with pinning of a domain wall in the kinked region. In this arrangement we assume according to the figure 6.15c that the switching field of section 1 is lower than for section 2. (a) External magnetic field $\mu_0 H$= - 0.8 T is expected to be sufficient to switch both sections of the nanomagnet (c.f. Fig. 6.11). The field is applied with the angle $\theta = 30^o$ which corresponds to $\varepsilon=101^o$, (b) the magnetic field is ramped to zero, reversed and raised to a value of 0.6 T. Both sections switch to the new configuration and the nanomagnet is prepared for the experiment, (c) magnetic field is set to zero and the actual $U_H(H)$ measurement in this configuration is performed in the field range $\mu_0 H = 0$ to -0.5T and the switching field of section 1 Hsw_1 is determined. Upon the switching of section 1 the domain wall between both sections is pinned. The magnetic field is then set back to $\mu_0 H$ = -0.8 T (depinning of the domain wall and switching of section 2) and this three step procedure is performed 200 times in order to provide the histogram of switching fields of section 1.*

Depending on the initial configuration of the nanowire i.e. with or without the domain wall pinned in the kink part, measured switching fields of section 1 are expected to be different due to exchange and dipolar interactions between both sections. Having the assumption of pinning of a domain wall during the magnetization reversal in mind we describe the ideas of switching experiments we performed. They are graphically presented in figures 6.16 – 6.17.

For the experiments we choose $\theta = 30^{o}$ which corresponds to the region in which the switching of section 2 is expected to be higher than section 1 (cf. Fig. 6.15c) and in which we observed biasing of the hysteresis loop (cf. Fig. 6.11). At first we probed the switching fields of section 1 where pinning of the domain wall between both sections is expected (cf. Fig 6.16). The entire nanomagnet was switched at field $\mu_0 H = 0.6$ T to the desired configuration as shown in figure 6.16b. Then the magnetic field was ramped to zero. The switching field of section 1 was probed then in the negative field range. When section 1 reverses its magnetization the domain wall is assumed to be pinned in the kinked area. The switching field Hsw_1 is determined and magnetic field is set back to $\mu_0 H = -0.8$ T and this three step procedure is performed 200 times in order to provide the histogram of switching fields.

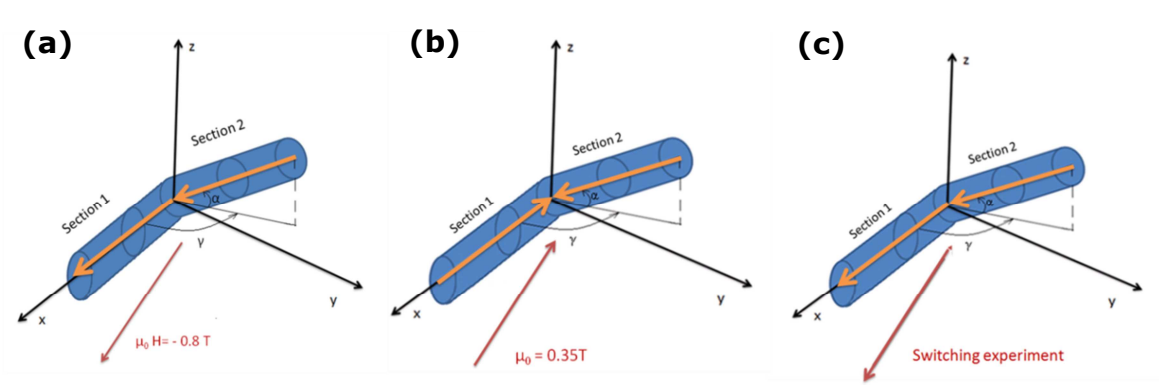

Figure 6.17: *Scenario of magnetic switching of the iron nanowire with depinning of the domain wall. (a) External magnetic field - 0.8 T is set and both sections are switched, (b) external magnetic field is ramped to zero. In order to measure the switching field of section 1 upon the depinning of the domain wall we must switch only section 1. We applied an external magnetic field of 0.35 T (we determined this value in other experiments) which switches the section 1 and the domain wall between both sections is pinned. The magnetic field is set to zero. As shown in figure 6.14c the configuration with pinned domain wall is stable, (c) in this configuration $U_H(H)$ measurement starts at field range 0 to - 0.5 T and the switching field of section 1 Hsw_2 is determined. Then the field is set to -0.8 T and measurements are repeated. To provide the histograms of the switching fields we performed 280 measurements.*

Secondly, we have probed the switching fields of section 1 associated with the depinning of the domain wall (cf. Fig 6.17).

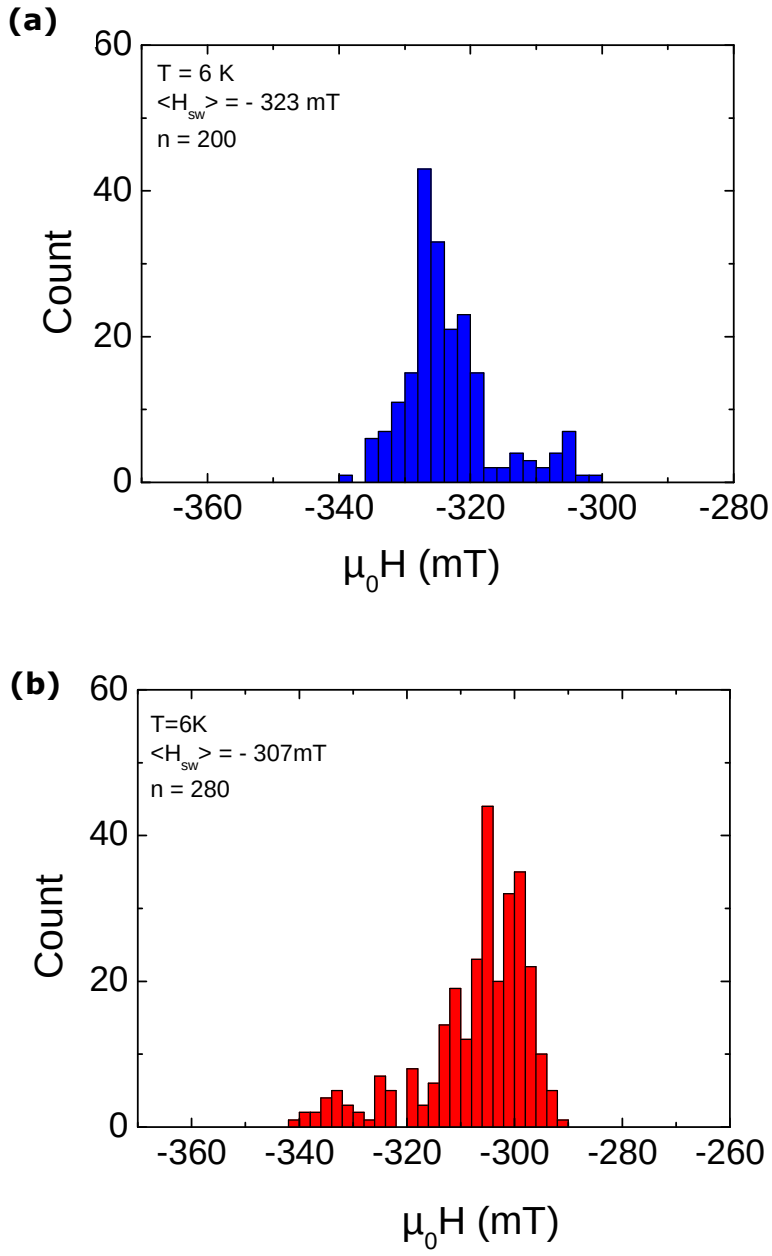

Figure 6.18: *Histograms of the switching fields of section 1 of the Fe-filled CNT. (a) Measured for the configuration described in figure 6.16a-c,<Hsw$_1$> = -323 mT, (b) measured for the configuration described in figure 6.17 a-c, <Hsw$_2$> = - 307 mT. (measured by Dr. S. Bahr)*

At first the magnetic field $\mu_0 H$ = - 0.8 T was set to switch both sections to the desired configuration (Fig. 6.17a). Then it was ramped to zero and swept to 0.35 T (cf. Fig 6.17b). Under this field it is expected that only section 1 switches and the domain wall is

pinned in the kinked part of the nanowire. Then the magnetic field is set back to zero. The configuration with pinned domain wall is stable as indicated by the MFM experiments (Fig 6.14c). The actual $U_H(H)$ experiment is performed in the negative field range. The switching of section 1 in the negative field range is associated with a depinning of the domain wall and Hsw_2 is determined. Then the field is set to -0.8 T and measurements are repeated. To provide the histograms of the switching fields we performed 280 measurements.

The results of the experiments which are sketched in detail in figures 6.16 – 6.17 are presented in figures 6.18 a and b. For the configuration in which upon the switching of section 1 of the nanowire the domain wall is pinned in the kink area (Fig. 6.18a) the majority of the switching events amount to - 328 mT and the calculated average of the switching field equals $<H_{sw1}>$ = - 323 mT. Figure 6.18b shows the switching field distribution of section 1 with depinning of the domain wall between the sections. Most of the detected switching events occur at fields of about - 306 mT. The calculated average of the switching field in this experiment is $<H_{sw2}>$ = - 307 mT. The relative shift of the average switching field of section 1 depending on the actual magnetization configuration of section 2 can be explained to occur as a result of a stray magnetic field from section 2 acting on section 1 and exchange interactions between both sections. This strictly means that biased hysteresis loops represent the minor loops of the investigated nanowire. Further, we can conclude that if there is not a biasing effect observed in the hysteresis loop the nanowire switches its entire magnetization. These experiments (MFM and Micro Hall study) reveal that the domain wall behavior during the magnetization reversal can be controlled by a pinning center such as a bent area of the nanowire and a bent area can be used to confine the domain wall during magnetization reversal [134,135]. The process of magnetization reversal of the nanowire can be interrupted by such pinning center and reversed, which provides a biasing of the measured minor hysteresis loop.

6.2.6. Summary and discussion

In conclusion, we investigated the switching behavior of Fe-filled CNT with diameter of about 16 nm and length in the μm range. The angular dependence of the nucleation fields shows a large increase of these values for low angles. This feature is characteristic for Stoner-Wohlfarth model of magnetization reversal in unison. However, we observed large suppression of the switching field values of about 50%. This can be

qualitatively explained in terms of the model proposed by Richter in which he considered and performed calculations of switching fields for infinite length ferromagnetic particles with defects. The effective volume for nucleation derived from the temperature dependence of the nucleation field is almost two orders of magnitude smaller than the volume of the nanowire. This suggests that magnetization switching is realized via nucleation of reversed magnetization and fast propagation of corresponding domain wall through the nanowire. The magnetization reversal process can be proposed as a localized mechanism in which the nucleation fields follow a coherent like rotation process while possibly structural defects of the nanowire are responsible for the massive suppression of the nucleation field values.

The bent area of the nanowire provides the pinning center in which the domain wall can be confined during the magnetization reversal as shown by the MFM image. The process of magnetization switching can be interrupted and reversed, what can explain the experimentally observed biasing of the minor hysteresis loop.

7. Summary

The aim of this thesis was to develop a micro Hall magnetometry setup for investigation of magnetic properties of magnetic nanostructures and to apply this device for investigating the magnetization reversal in individual ferromagnetically filled carbon nanotubes. These measurements were accompanied by studies of ensembles by means of Alternating Gradient and SQUID magnetometry.

Studies on ensembles provide an overview on the magnetic properties of carbon nanotubes. We have found strong effects of the remaining catalyst particles on the magnetization of the material. The magnetization studies turned out to be a very sensitive tool for determination of residual catalyst material. Through our magnetization studies we confirmed that a new method of post-annealing of CNT prepared by means of ferromagnetic catalyst material removes the catalyst without destroying the CNT material. In addition, the absence of any ferromagnetic impurities was also confirmed for CNTs made with Re catalyst. In both cases, the resulting CNTs are hence appropriate starting materials for investigation of CNT composites with magnetic materials, e.g., magnetically functionalized ones, or for biomedical usage which requires ultrapure materials.

The set-up of the micro Hall device and the measurements of individual Fe-filled CNT comprised utilized the following steps and experimental techniques:

- Design of the pattern containing Hall crosses and its writing onto the heterostructure,
- Transfer of the pattern into the heterostructure surface,
- Testing the structure of the devices by means of SEM and AFM,
- Contacting the 2DEG,
- Electrical testing of the contacts and devices,
- Micromanipulation of individual nanowires and placing one end of the nanowire onto the sensing area of the micro Hall device,
- Detailed studies of the magnetization switching of selected individual Fe nanowires.

The GaAs/AlGaAs-based micro Hall sensors were almost entirely prepared at the IFW Dresden for the first time. The device was successfully built and it was tested by means of studies on Fe nanowires protected by carbon shells. Our studies show that the prepared micro Hall sensors are excellent devices for detailed investigation of nanoscale magnetic nanowires. One challenging and time consuming task in this research was to exactly place the end of the nanowire at the center of the Hall sensor.

In our studies we performed a detailed investigation of the magnetic properties of two single crystalline Fe nanowires. Previous MFM studies showed that the magnetic configuration of straight Fe nanowires in the remanent state is single domain. The experimentally determined temperature dependence of the nucleation fields and the effective volume derived from these data suggest that the process of magnetization reversal is governed by thermally activated nucleation of a domain with reversed magnetization and propagation of the corresponding domain wall through the volume of the nanowire. Hysteresis loop measurements at large angles θ provide the nearly square shape behavior of hysteresis loops which reveals the single domain magnetic configuration of the nanowire. However we observed an additional step in hysteresis loops which we ascribed to the depinning of the domain wall during the magnetic switching process. The angular dependence of nucleation follows the curling model and the exchange constant of iron, derived from the fit, is in ~~the~~ good agreement with literature values. Thus our data reveal that the magnetization reversal is a localized process whereas the initial nucleation field follows the curling model. At angles nearly perpendicular to the nanowire axis we detect very high nucleation fields of about 900 mT which value is close to the anisotropy field of iron. This finding suggest the high quality of the iron filling and renders iron filled CNTs as desirable material for future applications like MFM sensors, or spintronic devices.

A very different picture of the magnetic properties is provided by micro Hall studies performed on a bent iron nanowire. The angular dependence of the nucleation fields and a large increase of the nucleation field at low angles θ suggest that the process of magnetization reversal has a coherent character. However, we observed a large suppression of the nucleation fields. This might be explained by some structural defect of the filling. Again the temperature dependence of the nucleation fields suggests that the magnetization switching is governed by nucleation of a small domain with reversed magnetization and propagation of the domain wall. A model is presented where the bent area of the nanowire forms a pinning center in which under certain circumstances during the magnetization switching process the domain wall can be trapped. Additional MFM

studies showed that indeed only one part of the nanowire can be switched. The process of magnetization reversal might then be interrupted by such a pinning center and reversed which can explain the experimentally observed biasing of the minor hysteresis loop.

APPENDIX

Calculation of the device angle tilt

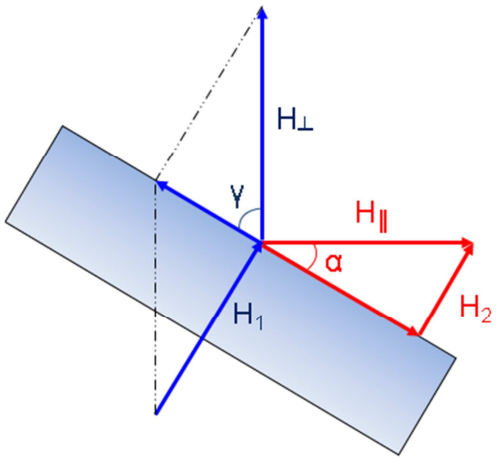

Figure A: Sketch of the device tilted with an angle α.

The Hall coefficient in such a configuration equals:

$$R_H = \frac{U_{H1}}{I \cdot H_1} = \frac{U_{H2}}{I \cdot H_2} \tag{A1}$$

U_{H1} and U_{H2} is the Hall voltage measured after application of current I and an external magnetic field H_{II} and $H_{\perp}$, respectively.

$$R_{H1} = \frac{U_{H1}}{I \cdot H_{\perp}} \tag{A2}$$

$$S = \frac{U_{H2}}{I \cdot H_{II}}$$

Where R_{H1} is the Hall coefficient obtained in experiments with applied an external magnetic field $H_{\perp}$, while S is the slope of a hysteresis loop due to tilting of the plain of the device upon application of an external magnetic field H_{II}.

$$\frac{R_{H1}}{S} = \frac{U_{H1}}{I \cdot H_{\perp}} \cdot \frac{I \cdot H_{II}}{U_{H2}} = \frac{U_{H1} \cdot H_{II}}{U_{H2} \cdot H_{\perp}} \tag{A3}$$

$$\frac{H_2}{H_{II}} = \sin\alpha$$
$$\frac{H_1}{H_{\perp}} = \sin\gamma = \sin(90^o - \alpha) = \cos\alpha \tag{A4}$$

Inserting H_{II} and $H_{\perp}$, from equation A4 into equation A3, we receive:

$$\frac{R_{H1}}{S} = \frac{U_{H1} \cdot H_2 \cdot \cos\alpha}{U_{H2} \cdot H_1 \cdot \sin\alpha} \tag{A5}$$

According to A1, we receive:

$$\frac{R_{H1}}{S} = ctg\,\alpha \tag{A6}$$

List of publications

1. **K. Lipert**, S. Bahr, F. Wolny, P. Atkinson, U. Weißker, T. Mühl, O. Schmidt, B. Büchner, R. Klingeler, Individual carbon-coated iron-nanowire probed by Micro Hall magnetometry, Applied Physics Letters 97, (2010) 212503,

2. **K. Lipert**, F. Kretzschmar, M. Ritschel, A. Leonhardt, R. Klingeler, B. Büchner, Nonmagnetic carbon nanotubes, J. Appl. Phys. 105, (2009) 063906,

3. **K. Lipert**, M. Ritschel, A. Leonhardt, Y. Krupskaya, B. Büchner, R. Klingeler., Magnetic properties of carbon nanotubes with and without catalysts. J. Phys.: Conf. Ser. 200, (2010) 072061,

4. M. U. Lutz, **K. Lipert**, Y. Krupskaya, S. Bahr, A. Wolter, A. A. El-Gendy, S. Hampel, A. Leonhardt, A. Taylor, K. Krämer, B. Büchner, R. Klingeler, Feasibility of magnetically filled CNT for biological applications: From fundamental properties of individual nanomagnets to nanoscaled heaters and temperature sensors. Book chapter, Springer-Verl., 2011, 97-124 (2011).

5. A. Taylor, **K. Lipert**, K. Kraemer, S. Hampel, S. Fuessel, A. Meye, R. Klingeler, M. Ritschel, A. Leonhardt, B. Buechner, M.P. Wirth Biocompatibility of iron filled carbon nanotubes in vitro, Journal of Nanoscience and Nanotechnology **9** (2009) 5709,

6. E. Heister, V. Neves, C. Tîlmaciu, **K. Lipert**, V. Sanz Beltrán, H. Coley, S. R. P. Silva and J. McFadden, Triple functionalisation of single-walled carbon nanotubes with doxorubicin, a monoclonal antibody, and a fluorescent marker for targeted cancer therapy, Carbon 47, (2009) 2151,

7. F. Wolny, T. Mühl, U. Weissker, **K. Lipert**, J. Schumann, A. Leonhardt and B. Büchner, Iron filled carbon nanotubes as novel high resolution probes for quantitative magnetic force microscopy. Nanotechnology 21, (2010) 435501,

References

[1] http://www.zyvex.com/nanotech/feynman.html,

[2] A. D. Kent, S. von Molnár, S. Gider, D. D. Awschalom, *Properties and measurement of scanning tunneling microscope fabricated ferromagnetic particle arrays (invited),* J. Appl. Phys. 76, (1994) 6656,

[3] L. Theil Kuhn, A.K. Geim, J.G.S. Lok, P. Hedegärd, K. Ylänen, J.B. Jensen, E. Johnson and P.E. Lindelof, *Magnetisation of isolated single crystalline Fe-nanoparticles measured by a ballistic Hall micro-magnetometer,* Eur. Phys. J. D 10, (2000) 259,

[4] S. Iijima, *Curling and closure of graphitic networks under electron-beam irradiation,* Nature 359, (1992) 707,

[5] C. Guerret-Piécourt, Y. Le Bouar, A. Loiseau, H. Pascard, *Relation between metal electronic structure and morphology of metal compounds inside carbon nanotubes,* Nature 372, (1994) 76,

[6] A. Thess, R. Lee, P. Nikolaev, H. Dai, P. Petit, J. Robert, C. Xu, Y. H. Lee, S. G. Kim, A. G. Rinzler, D. T. Colbert, G. E. Scuseria, D. Tománek, J. E. Fischer, R. E. Smalley, *Crystalline Ropes of Metallic Carbon Nanotubes,* Science 273, (1996) 483,

[7] A. Leonhardt, S. Hampel, C. Mueller, I. Moench, R. Koseva, M. Ritschel, D. Elefant, K. Biedermann, B. Buechner, *Synthesis, properties and applications of ferromagnetic-filled carbon nanotubes,* Chemical Vapor Deposition 12, (2006) 380,

[8] J. P. Salvetat, J. M. Bonard, N. H. Thomson, A. J. Kulik, L. Forró, W. Benoit, L. Zuppiroli, *Mechanical properties of carbon nanotubes,* Appl. Phys. A 69, (1999) 255,

[9] S.C. Tsang, Y.K. Chen, P.J.F. Harris, M.L.H. Green, *A simple chemical method of opening and filling carbon nanotubes,* Nature 372, (1994) 159,

[10] F. Qiang, G. Weinberg, S. Dang-sheng, *Selective filling of carbon nanotubes with metals by selective washing,* New Carbon Materials 23, (2008) 17,

[11] K. Schulte1, C. Yan, M. Ahola-Tuomi, A. Strozecka, P. J. Moriarty, A. N. Khlobystov, Journal of Physics: Conference Series 100, (2008) 012017,

[12] M. Monthioux, *Filling single-wall carbon nanotubes.* Carbon 40, (2002) 1809,

[13] D. Tasis, N. Tagmatarchis, A. Bianco, M. Prato, *Chemistry of carbon nanotubes*, Chem. Rev. 106, (2006) 1105,

[14] K. Balasubramanian, M. Burghard, *Chemically Functionalized Carbon Nanotubes,* Small 1, (2005)180,

[15] C. Klumpp, K. Kostarelos, M. Prato, A. Bianco, *Functionalized carbon nanotubes as emerging nanovectors for the delivery of therapeutics,* Biochim. Biophys. Acta, 1758 (2006) 404,

[16] I. Moench, A. Meye, A. Leonhardt, K. Kraemer, R. Kozhuharova, T. Gemming, M.P. Wirth, B. Buechner, *Ferromagnetic filled carbon nanotubes and nanoparticles: synthesis and lipid-mediated delivery into human tumor cells,* J. Magn. Magn. Mater. 290–291 (2005) 276,

[17] H. Jin, D. A. Heller, M. S. Strano, *Single-Particle Tracking of Endocytosis and Exocytosis of Single-Walled Carbon Nanotubes in NIH-3T3 Cells,* Nano Lett. 8, (2008) 1577,

[18] A. Taylor, Y. Krupskaya, K. Krämer, S. Füssel, R. Klingeler, B. Büchner, M. P. Wirth, *Cisplatin-loaded carbon-encapsulated iron nanoparticles and their in vitro effects in magnetic fluid hyperthermia*, Carbon 48, (2010) 2327,

[19] L. Lacerda, A. Bianco, M. Prato, K. Kostarelos, *Carbon nanotubes as nanomedicines: From toxicology to pharmacology,* J. Contr. Rel. 58, (1460) 2006,

[20] Y. Krupskaya, C. Mahn, A. Parameswaran, A. Taylor, K. Krämer, S.Hampel, A. Leonhardt, M. Ritschel, B. BÄuchner, R. Klingeler, *Magnetic study of iron-containing carbon nanotubes: feasibility for magnetic hyperthermia,* J. Magn. Magn. Mater. 321, (2009) 4067,

[21] A. P. Shpak, S.P. Kolesnik, G. S. Mogilny, Y. N. Petrov, V. P. Sokhatsky, L.N. Trophimova, B. D. Shanina, V. G. Gavriljuk, *Structure and magnetic properties of iron nanowires encased in multiwalled carbon nanotubes*, Acta Materialia 55, 1769 (2007),

[22] F. Geng, H. Cong, *Fe-filled carbon nanotube array with high coercivity,* Physica B 382, 300 (2006),

[23] C. Müller, S. Hampel, D. Haase, D. Elefant, T. Muehl, A. Vyalikh, R. Klingeler, D. Golberg, A. Leonhardt, B. Büchner, in: Nanorods, Nanotubes and Nanomaterials Research Progress; W. V. Prescott and A. I. Schwartz (eds.), Nova Science Publishers (2008),

[24] A. Vyalikh, A.U.B. Wolter, S. Hampel, D. Haase, M. Ritschel, A. Leonhardt, H.-J. Grafe, A. Taylor, K. Krämer, B. Büchner, R. Klingeler, *A carbon-wrapped nanoscaled thermometer for temperature control in biological environment,* Nanomedicine 3, (2008) 321,

[25] U. Weissker, S. Hampel, A. Leonhardt, B. Büchner, *Carbon Nanotubes Filled with Ferromagnetic Materials*, Materials 3, (2010) 4387,

[26] W. Heisenberg, *Many-Body Problem and Resonance in Quantum Mechanics*, Z. Phys 38, (1926) 441,

[27] P. A. M. Dirac, *On the Theory of Quantum Mechanics,* Proc. Roy. Soc. (London) A 112, (1926) 661,

[28] W. W. Heisenberg, *Zur Theorie des Ferromagnetismus,* Z. Phys. 49, (1928) 619,

[29] H. Kronmüller and M. Lambeck, Bergmann-Schaefer:
Lehrbuch der Experimentalphysik -Festkörper. Walter de Gruyter, Berlin, New York (1992)

[30] O'Handley, Robert C. O'Handley, Modern Magnetic Materials: Principles and Applications, John Wiley & Sons, Inc. (2000),

[31] K. Honda, S. Kaya, Sci. Rep. Tohoku Imp. Univ. [I] 15, (1926) 721,

[32] J. L. Dormann, D. Fiorani, and E. Tronc in Advances in Chemical Physics, Volume XCVIII, Edited by I. Prigogine and Stuart A. Rice, John Wiley & Sons, Inc. (1997),

[33] W. H. Meiklejohn and C. P. Bean, *New Magnetic Anisotropy*, Phys. Rev. 102 (1956) 1413,

[34] A. Hubert, R. Schäfer: *Magnetic Domains*, Springer Verlag, Berlin, 1998,

[35] C. Kittel, *Introduction to Solid State Physics,* John Wiley & Sons, Inc. (1996),

[36] C. Kittel, *Physical Theory of Ferromagnetic Domains*, Rev. Mod. Phys. 21, (1949) 541,

[37] E.C. Stoner, E.P. Wohlfarth, *A Mechanism of Magnetic Hysteresis in Heterogeneous Alloys*, Philos. Trans. Roy. Soc. London, A 240, (1948) 599,

[38] E.C. Stoner, E.P. Wohlfarth, *A Mechanism of Magnetic Hysteresis in Heterogeneous Alloys,* IEEE Trans. Magnetics 27, (1991) 3475,

[39] W.F. Brown, *Criterion for Uniform Micromagnetization,* Jr. Phys. Rev. 105, (1957)1479,

[40] A. Aharoni, *Angular dependence of nucleation by curling in a prolate spheroid,* J. Appl. Phys. 82 (1997) 1281,

[41] A. Aharoni, An *Introduction to the Theory of Ferromagnetism*, Oxford University Press, London (1996),

[42] E.H. Frei, S. Shtrikman, D. Treves, *Critical Size and Nucleation Field of Ideal Ferromagnetic Particles*, Phys. Rev. 106, (1957) 446,

[43] E.H. Frei, S. Shtrikman, D. Treves, *Critical Size and Nucleation Field of Ideal Ferromagnetic Particles*, Phys. Rev. 106, (1957) 446,

[44] L. Gunther and B. Barbara, *Quantum tunneling across a domain-wall junction*, Phys. Rev. B 49, (1994) 3926,

[45] W. G. Jenks, S. S. H. Sadeghi, J. P. Wikswo Jr, *SQUIDs for nondestructive evaluation*22, J. Phys. D: Appl. Phys. 30, (1997) 293,

[46] http://www.qdusa.com/products/mpms.html (9.11.2010),

[47] P. J. Flanders, *An alternating gradient magnetometer (invited),* J. Appl. Phys. 63, (1988) 3940,

[48] http://www.princetonmeasurements.com/newtwohds01.htm (19.10.2010),

[49] S. Blundell, *Magnetism in Condensed Matter,* Oxford University Press 2001,

[50] W. Wernsdorfer, B. Doudin, D. Mailly, K. Hasselbach, A. Benoit, J. Meier, J.-Ph. Ansermet, and B. Barbara, *Nucleation of Magnetization Reversal in Individual Nanosized Nickel Wires*, Physical Review Letters 77, (1996) 1873,

[51] W. Wernsdorfer, K. Hasselbach, D. Mailly, B. Barbara, A. Benoit, L. Thomas, G. Suran, *DC-SQUID magnetization measurements of single magnetic particles*, J. Magn. Magn. Mater. 145, (1995) 33,

[52] W. Wernsdorfer, D. Mailly, A. Benoit, *Single nanoparticle measurement techniques*, J. Appl. Phys. 87, (2000) 5094,

[53] C. Thirion, W. Wernsdorfer, M. Jamet, V. Dupuis, P. Mélinon, A. Pérez, D. Mailly, *Micro-SQUID technique for studying the temperature dependence of switching fields of single nanoparticles*, . Magn. Magn. Mater. 242, (2002) 993,

[54] A. Yamaguchi, K. Takeda, T. Matsumoto, G. Motoyama, H. Kashiwaya, S. Kuriki, S. Kashiwaya, S. Ohkoshi, A. Sumiyama, *Development of Micro-SQUID Magnetometers for Investigation of Quantum Tunneling of Magnetization in Nanometer-Size Magnetic Materials*, J. Low Temp. Phys. 158, (2010) 704,

[55] M.U. Lutz, U. Weissker, F. Wolny, C. Mueller, M. Loeffler, T. Muehl, A. Leonhardt, B. Buechner, R. Klingeler, *Magnetic properties of α-Fe and Fe3C nanowires*, Journal of Physics: Conference Series 200, (2010) 72062,

[56] F. Wolny, T. Mühl, U. Weissker, K. Lipert, J. Schumann, A. Leonhardt and B. Büchner, *Iron filled carbon nanotubes as novel monopole-like sensors for quantitative magnetic force microscopy*, Nanotechnology 21, (2010) 435501,

[57] M. Kleiber, F. Kümmerlen, M. Löhndorf, and A. Wadas, *Magnetization switching of submicrometer Co dots induced by a magnetic force microscope tip*, Phys. Rev. B 58, (1998) 5563,

[58] D. Schuh, J. Biberger, A. Bauer, W. Breuer, D. Weiss, *Hall-magnetometry on ferromagnetic dots and dot arrays*, IEEE Trans. Magn. 37, (2001) 2091,

[59] L. Theil Kuhn, A.K. Geim, J.G.S. Lok, P. Hedegård, K. Ylänen, J.B. Jensen, E. Johnson and P.E. Lindelof, *Magnetisation of isolated single crystalline Fe-nanoparticles measured by a ballistic Hall micro-magnetometer*, Eur. Phys. J. D 10, (2000) 259,

[60] E. Hall, *On a New Action of the Magnet on Electric Currents*, American Journal of Mathematic 2, (1879) 287,

[61] G. Boero, M. Demierre, P.-.A. Besse, R.S. Popovic, *Micro-Hall devices: performance, technologies and applications*, Sensors and Actuators A 106, (2003) 314,

[62] Y. Li, P Xiong, S. Wirth, S. von Molnár, Y. Ohno, H. Ohno, *Hall magnetometry on a single iron nanoparticle*, Appl. Phys. Lett. 80, (2002) 4644,

[63] V. Cambel, G. Karapetrov, P. Elias, S. Hasenohrl, W.K. Kwok, J. Krause, J. Manka, *Approaching the pT range with a 2DEG InGaAs/InP Hall sensor*, Microelectronic Engineering 51 (2000) 333,

[64] X.Q. Li, F.M. Peeters, and A.K. Geim, *The Hall effect of an inhomogeneous magnetic field in mesoscopic structures*, J. Phys.: Condens. Matter. 9, (1997) 8065,

[65] F. M. Peeters, X. Q. Li, *Hall magnetometer in the ballistic regime*, Appl. Phys. Lett. 72, (1998) 572,

[66] Y. Li, *Optimization of Hall magnetometry and single magnetic nanoparticle measurements*, PhD dissertation at The Florida State University, 2003,

[67] O. Madelung, ed, *Semiconductors - Basic Data*, 2nd Revised edition Berlin: Springer,1996),

[68] D. E. Aspnes, S. M. Kelso, R. A. Logan, R. Bhat, *Optical properties of AlxGa1−x As*, Journal of Applied Physics 60, (1986) 754,

[69] D.D. Carey, S.T. Stoddart, S.J. Bending, J.J. Harris, C.T. Foxon, *Investigation of deep metastable traps in Si δ-doped GaAs/Al0.33Ga0.67As quantum-well samples using noise*, Physical Review B 54, (1996) 2813,

[70] S. Datta, *Electronic Transport in Mesoscopic Systems*, Cambridge University Press, Cambridge, 1995,

[71] G.H. English, A.C. Gossard, H.L. Störmer, and K.W. Baldwin, *GaAs structures with electron mobility of 5×106 cm2/V*s, Applied Physics Letters 50, (1987) 1826,

[72] S. Datta, *Electronic Transport in Mesoscopic Systems*, 2nd edition, Cambridge University Press, Cambridge, 1997,

[73] H. van Houten, *Quantum transport in nanostructures: from electron waveguide to electron box*, Microelectronic Engineering 23 (1994) 31,

[74] C. W. J. Beenakker, H. van Houten, *Billiard model of a ballistic multiprobe conductor* Phys. Rev. Lett. 63, (1989)1857,

[75] H. van Houten and C. W. J. Beenakker, *Nanostructure Physics and Fabrication*, Academic, New York, 1989,

[76] M.L. Roukes, A. Scherer, S.J. Allen, Jr., H.G. Craighead, R.M. Ruthen, E.D. Beebe, and J.P. Harbison: *Quenching of the Hall Effect in a one-dimensional Wire,* Phys. Rev. Lett. 59, (1987) 3011,

[77] H. Akera, T. Ando, *Current distribution and Hall resistance in quantum wires*, Surface Science 229, (1990) 268,

[78] C. J. B. Ford, T. J. Thornton, R. Newbury, M. Pepper, H. Ahmed, D. C. Peacock, D. A. Ritchie, J. E. F. Frost, and G. A. C. Jones, *Vanishing hall voltage in a quasi-one-dimensional GaAs-AlxGa1-xAs heterojunction,* Phys. Rev. B 38, (1988) 8518,

[79] C.W.J. Beenakker, H. van Houten: *Quantum Transport in Semiconductor Nanostructures,* in: H. Ehrenreich, D. Turnbull (eds.): Solid State Physics, Volume 44, Academic Press, San Diego, 1991, S. 1-228,

[80] C. J. B. Ford, S. Washburn, M. Büttiker, C. M. Knoedler, J. M. Hong, *Influence of geometry on the Hall effect in ballistic wires*, Phys. Rev. Lett. 62, (1989) 2724,

[81] FEI Company, *The Nova NanoSEM User's Operation Manual,* 4th edition, 2006,

[82] K.D. Vernon-Parry, III-Vs Review 13, (2000) 40,

[83] Nanonic GmbH company. http://www.nanonic.de/, 2010,

[84] W. Daumann: *InP-Kurzkanal-Heterostruktur-Feldeffekttransistoren mit elektronenstrahldefinierten Gate-Kontakten,* Dissertation, Universität Duisburg, 2000,

[85] A. Leonhardt, S. Hampel, C. Müller, I. Mönch, R. Koseva, M. Ritschel, D. Elefant, K. Biedermann, B. Büchner, *Synthesis, Properties, and Applications of Ferromagnetic-Filled Carbon Nanotubes,* Chem. Vap. Deposition 12, (2006) 380,

[86] A. Leonhardt, S. Hampel, C. Mueller, I. Moench, R. Koseva, M. Ritschel, D. Elefant, K. Biedermann, B. Buechner, *Synthesis, properties and applications of ferromagnetic-filled carbon nanotubes,* Chemical Vapor Deposition 12 (2006) 380,

[87] Kleindiek Nanotechnik, http://www.nanotechnik.com/mm3a-lmp.html/, 2010,

[88] A. Peigney, C. Laurent, F. Dobigeon,, A. Rousset, *Carbon Nanotubes grown in situ by a novel catalitic method* J. Mater. Res. 12, (1997) 613,

[89] H. Dai, A. G. Rinzler, P. Nikolaev, A. Thess, D. T. Colbert, R. E. Smalley, *Single-wall nanotubes produced by metal-catalyzed disproportionation of carbon monoxide,* Chem. Phys. Lett. 260, (1996) 471,

[90] J. Hafner, M. J. Bronikowski, B. R. Azamian, P. Nikolaev, A. G. Rinzler, D. T. Colbert, K. A. Smith, R. E. Smalley, *Catalytic growth of single-wall carbon nanotubes from metal particles,* Chem. Phys.Lett. 296, (1998) 195,

[91] N. Nagaraju, A. Fonseca, Z. Konya, J. B. Nagy, *Alumina and silica supported metal catalysts for the production of carbon nanotubes,* J. Mol. Catal. A: Chem. 181, (2002) 57,

[92] S. Y. Lee, M. Yamada, M. Miyake, *Synthesis of carbon nanotubes and carbon nanofilaments over palladium supported catalysts,* Sci. Technol. Adv. Mater. 6, (2005) 420,

[93] A. M. Cassell, J. A. Raymakers, J. Kong, H. Dai, *Large-scale CVD synthesis of single walled carbon nanotubes,* J. Phys. Chem. B 103 , (1999) 6484,

[94] M. L. Mabudafhasi, R. Bodkin, C. P. Nicolaides, X. Y. Liu, M. J. Witcomb, N. J. Coville, *The ruthenium catalysed synthesis of carbon nanostructures,* Carbon 40, (2002) 2737,

[95] K. Lipert, F. Kretzschmar, M. Ritschel, A. Leonhardt, R. Klingeler, B. Büchner, *Nonmagnetic carbon nanotubes,* J. Appl. Phys. 105, (2009) 063906,

[96] M. Ritschel, A. Leonhardt, D. Elefant, S. Oswald, and B. Büchner, *Rhenium-Catalyzed Growth Carbon Nanotubes,* J. Phys. Chem. C 111, (2007) 8414,

[97] J. Heremans, C. H. Olk, and D. T. Morelli, *Magnetic susceptibility of carbon structures,* Phys. Rev. B 49, (1994) 15122,

[98] F. Tsui, L. Jin, and O. Zhou, *Anisotropic magnetic susceptibility of multiwalled carbon nanotubes,* Appl. Phys. Lett. 76, (2000) 1452,

[99] P. Byszewski and M. Baran, *Magnetic Susceptibility of Carbon Nanotubes*, Europhys. Lett. 31, (1995) 363,

[100] K. Lipert, M. Ritschel, A. Leonhardt, Y. Krupskaya, B. Büchner, R. Klingeler., *Magnetic properties of carbon nanotubes with and without catalysts,* J. Phys.: Conf. Ser. 200, (2010) 072061,

[101] A. Leonhardt, M. Ritschel, D. Elefant, N. Mattern, K. Biedermann, S. Hampel, Ch. Müller, T. Gemming, B. Büchner, *Enhanced magnetism in Fe-filled carbon nanotubes produced by pyrolysis of ferrocene,* J. Appl. Phys. 98, (2005) 074315,

[102] R. Skomski, *Nanomagnetics,* J. Phys.: Condens. Matter 15, (2003) 841,

[103] A. Hütten, D. Sudfeld, I. Ennen, G. Reiss, K. Wojczykowski, P. Jutzi, *Ferromagnetic FeCo-nanoparticles for biotechnology*, J. Magn. Magn. Magn. 293, (2005) 93,

[104] L. Neel, *Propriétés d'un ferromagnétique cubique en grains fins*, Compt. Rend. (Paris) 224, (1947) 1488,

[105] R. C. O'Handley, *Modern Magnetic Materials New York,* NY: John Wiley and Sons, Inc. 2000,

[106] G. Herzer, *Nanocrystalline soft magnetic materials,* J. Magn. Magn. Mater. 112, (1992) 258,

[107] M. Kersten, *Zur Theorie der Koerzitivkraft,* Z. Phys. 124, (1948) 714,

[108] S. Hampel, A. Leonhardt, D. Selbmann, K. Biedermann, D. Elefant, C. Mueller, T. Gemming, B. Buechner, *Growth and characterization of filled carbon nanotubes with ferromagnetic properties*, Carbon 44, (2006) 2316,

[109] M. U. Lutz, K. Lipert, Y. Krupskaya, S. Bahr, A. Wolter, A. A. El-Gendy, S. Hampel, A. Leonhardt, A. Taylor, K. Krämer, B. Büchner, R. Klingeler, *Feasibility of magnetically filled CNT for biological applications: From fundamental properties of individual nanomagnets to nanoscaled heaters and temperature sensors.* Book chapter, Springer-Verl., 2011, 97-124 (2011).

[110] K. Lipert, S. Bahr, F. Wolny, P. Atkinson, U. Weißker, T. Mühl, O. Schmidt, B. Büchner, R. Klingeler, *Individual carbon-coated iron-nanowire probed by Micro Hall magnetometr*y, Applied Physics Letters 97, (2010) 212503,

[111] F. Geng and H. Cong, *Fe-filled carbon nanotube array with high coercivity*, Physica B 382, (2006) 300,

[112] C. Müller, S. Hampel, D. Haase, D. Elefant, T. Muehl, A. Vyalikh, R. Klingeler, D. Golberg, A. Leonhardt, B. Büchner, *Selected synthesis methods for nanowires encapsulated inside carbon nanostructures and their fascinating properties*, Nanorods, Nanotubes and Nanomaterials Research Progress, edited by W. V. Prescott and A. I. Schwartz (Nova Science, New York, 2008),

[113] P. Banerjee, F. Wolny, D. V. Pelekhov, M. R. Herman, K. C. Fong, U. Weissker, T. Mühl, Yu. Obukhov, A. Leonhardt, B. Büchner, and P. Chris Hammel, *Magnetization reversal in an individual 25 nm iron-filled carbon nanotube*, Appl. Phys. Lett. 96, (2010) 252505,

[114] W. Wernsdorfer, K. Hasselbach, A. Benoit, B. Barbara, B. Doudin, J. Meier, J. –Ph. Ansermet, D. Mailly, *Measurements of magnetization switching in individual nickel nanowires*, Phys. Rev. B 55, (1997) 11552,

[115] W. Wernsdorfer, K. Hasselbach, A. Sulpice, A. Benoit, J.-E. Wegrowe, L. Thomas, B. Barbara, D. Mailly, *Dynamical measurement of domain-wall nucleation and annihilation in individual amorphous Co particles*, Phys. Rev. B 53, (1996) 3341,

[116] R. Skomski, *Simple Models of Magnetism*, Oxford University Press, New York, 2008,

[117] M. E. Schabes, *Micromagnetic theory of non-uniform magnetization processes in magnetic recording particles*, J. Magn. Magn. Mater. 95, (1991) 249,

[118] R. Skomski, *Magnetic localization in transition-metal nanowires*, Phys. Rev. B 62, (2000) 3900,

[119] B. Barbara, *Single-particle nanomagnetism*, Solid State Sciences 7, (2005) 668,

[120] H. B. Braun, *Thermally Activated Magnetization Reversal in Elongated Ferromagnetic Particles*, Phys. Rev. Lett. 71, (1993) 3557,

[121] J.E. Knowles, *Magnetization reversal by flipping, in acicular particles of γ-Fe2O3*, J. Magn. Magn. Mater. 61, (1986) 121,

[122] L. Landau and E. Lifshitz, Phys. Z. Sowjetunion 8, (1935) 153,

[123] W. F. Brown, Jr., *Thermal Fluctuations of a Single-Domain Particle*, Phys. Rev. 130, (1963) 1677,

[124] E.D. Boerner, H. N. Bertram, *Dynamics of thermally activated reversal in nonuniformly magnetized single particles*, IEEE Transactions on Magnetics 33, (1997) 3052,

[125] L. Gunther, B. Barbara, *Quantum tunnelling across a domain-wall junction*, Phys. Rev. B 49, (1994) 3926,

[126] W. Wernsdorfer, K. Hasselbach, B. Barbara, L. Thomas, D. Mailly, G. Suran, *DC-SQUID magnetization measurements of single magnetic particles,* Journal of Magnetism and Magnetic Materials 145, (1995) 33,

[127] R. Skomski, H. Zeng, M. Zheng, and D. J. Sellmyer, *Magnetic localization in transition-metal nanowires,* Phys. Rev. B 62, (2000) 3900,

[128] J. Kurkijärvi, *Intrinsic Fluctuations in a Superconducting Ring Closed with a Josephson Junction,* Phys. Rev. B 6, (1971) 832,

[129] W. Wernsdorfer, B. Doudin, D. Mailly, K. Hasselbach, A. Benoit, J. Meier, J. –Ph. Ansermet, B. Barbara, *Nucleation of Magnetization Reversal in Individual Nanosized Nickel Wires*, Phys. Rev. Lett. 77, (1996) 1873,

[130] H. J. Richter, *Model calculations of the angular dependence of the switching field of imperfect ferromagnetic particles with special reference to barium ferrite,* J. Appl. Phys. 65, (3597) 1989,

[131] D. Golberg, M. Mitome, Ch. Müller, C. Tang, A. Leonhardt, Y. Bando, *Atomic structures of iron-based single-crystalline nanowires crystallized inside multi-walled carbon nanotubes as revealed by analytical electron microscopy,* Acta Materialia 54 (2006) 2567,

[132] Y. Uesaka, Y. Nakatani, N. Hayashi, J. Appl. Phys., *Computer simulation of magnetization reversal in fine hexagonal platelet particles with defects,* 69, (1991) 4847,

[133] J. Gadbois, J.-G. Zhu, *Effect of Edge Roughness in Nano-Scale Magnetic Bar Switching,* IEEE Trans. Magn. 31, (1995) 3802,

[134] M. Kläui, H. Ehrke, U. Rüdiger, T. Kasama, R. E. Dunin-Borkowski, D. Backes, L. J. Heyderman, C. A. F. Vaz, J. A. C. Bland, G. Faini, E. Cambril, W. Wernsdorfer, *Direct observation of domain-wall pinning at nanoscale constrictions,* Appl. Phys. Lett. 87, (2005) 102509,

[135] M. Kläui, A. F. Vaza, A. Lapicki, T. Suzuki, Z. Cuic, J. A. C. Bland, *Domain wall pinning in ferromagnetic structures fabricated by focused ion beam*, Microelectronic Engineering 73–74, (2004) 785.

Acknowledgments

I would like to gratefully thank all of the people who helped during the complete this work:

Firstly I would like to truly say thanks to my supervisor Prof. Rüdiger Klingeler and Prof. Bernd Büchner who accepted me to work on this challenging task and provided me with funding.

Prof. Klingeler is an extremely patient and calm person and I have learned from him much about shaping and writing scientific publications.

Dr. Stefan Bahr was an important person in this work who helped immensely with electronic and software aspects. He also helped perform measurements on bent Fe nanowire.

Dr. Daniel Grimm who introduced me to EBL.

Franziska Wolny for her introduction to the micromanipulation system and her help.

Dr. Paola Atkinson for providing me with 2DEG heterostructures.

Dr. Josef Biberger, Cornelia Linz and Prof. Dieter Weiss for fruitful collaborations and providing 2DEG contacts.

Dr. Thomas Mühl who was always open and had time for long and fruitful discussions.

I also would like to thank all of those around me for nice atmosphere, especially: Matthias, Ahmed, Yulia, Wolfram, Diana, Mark, Rafael, Alicja and many, many others.

Special thanks to Malgorzata.